Electronic Supplementary Material (ESI) for Energy & Environmental Science.

Electronic supporting information

Material and system development needs for widespread deployment of hydroxide exchange membrane fuel cells in light-duty vehicles

Author Names: Reza Abbasi*, Brian P. Setzler, and Yushan Yan*

Affiliation(s): Center for Clean Hydrogen and Department of Chemical and Biomolecular Engineering, University of Delaware, 150 Academy Street, Newark, DE 19716, USA

*Corresponding Author E-mail Address: Reza Abbasi: (abbasi@udel.edu; abbasi2@wisc.edu)

Yushan Yan: (yanys@udel.edu)

FC stack performance model details

Schematic diagram of the pseudo-2-D FC

Figure S1 shows the schematic diagram of our pseudo-2-D FC model, which is a 1-D FC sandwich model coupled with a 1-D down-the-channel model. The 1-D FC sandwich model only considers the direction normal to the MEA along the MEA thickness. The 1-D down-the-channel model consists of mass balance down the channel for the species present in the channel coupled with an assumption of linear total pressure drop along the flow channels.

One-dimensional (1-D) FC sandwich model

Dimensions of the modeling domains and the values of transport parameters used for each domain

The 1-D FC sandwich model includes two gas diffusion layers (GDLs), two microporous layers (MPLs), two electrocatalyst layers, and a membrane. Table S1 shows the values of the dimensions of the modeling domains and the values of transport parameters used for each domain. We set the transport properties at reasonable values using the data available in the literature. We

note some differences exist in the dimensions of domains and some of the transport properties between GMs polarization curves (Figure 2, S2, and S3) and those assumed by us for either our base-case system cost estimation or our 30 $/kW$_{Net}$ LDV systems. When these differences exist, we mention them as "GM-case", "Base-case", and "30 $/kW$_{Net}$-case" in Table S1. We clarify these differences below and explain some transport parameters used for each domain.

i) All the FCs in this paper have the same GDL thickness on the anode and cathode sides. Similarly, all the FCs in this paper have the same MPL thickness on the anode and cathode sides. The thickness of the GDL and MPL for GM-case are 200 µm and 30 µm, respectively.[1] For our base-case, where we determined the system cost based on currently available materials, the thickness of the GDL and MPL are identical to those mentioned in the SA comprehensive report and are 105 µm and 45 µm, respectively.[2] For the 30 $/kW$_{Net}$-case, where we determined the material and system development needs to achieve 30 $/kW$_{Net}$ system cost, we assumed the thickness of the GDL and MPL to be 90 µm and 20 µm, respectively.

ii) For GM-case, the membrane thickness is 25 µm.[1, 3] The SA comprehensive report specifies that the 2018 LDV system's membrane thickness is 14 µm. However, the report also mentions that a transition to a 10 µm membrane is very likely, and it sets the membrane thickness for 2020 and 2025 LDV systems to 10 µm.[2] Considering the above fact and the fact that the SA evaluation of the Toyota Mirai LDV shows that Toyota Mirai already operates using a 10 µm membrane, we chose 10 µm as the thickness of membrane for both our base-case and 30 $/kW$_{Net}$-case.[2]

iii) For the anode/cathode electrocatalyst layers, we assumed the porosity and volume fraction of the ionomer and electrocatalyst to be 0.7, 0.15, and 0.15, respectively. For

all electrocatalysts except Fe-N-C, the volume fraction and thickness are related through equation S1.

$$\varepsilon_{Cat} = 0.15 = \varepsilon_{Active} + \varepsilon_{Carbon} = \frac{1}{t_{Cat}}\left(\frac{L_{Active}}{\rho_{Active}} + \frac{L_{Carbon}}{\rho_{Carbon}}\right) \quad (S1)$$

In equation S1, ε_{Cat}, ε_{Active}, ε_{Carbon}, t_{Cat}, L_{Active}, L_{Carbon}, $\rho_{Active,}$ and ρ_{Carbon} are the volume fraction of the electrocatalyst/active phase of the electrocatalyst/carbon support, the thickness of the electrocatalyst layer, mass loading of the active phase of the electrocatalyst/carbon support within the electrode, and the density of the active phase of the electrocatalyst/carbon support, respectively. In our calculations, we assumed that (ρ_{Carbon}=2000 kg/m^3). One can think of Fe-N-C conceptually and ideally as carbon support on which tiny amounts of Fe have been dispersed atomically as active sites. Consequently, the Fe-N-C volume fraction and thickness are related through equation S2.

$$\varepsilon_{Fe-N-C} = 0.15 = \frac{1}{t_{Fe-N-C}}\left(\frac{L_{Fe-N-C}}{\rho_{Fe-N-C}}\right) \quad (S2)$$

In equation S2, $\varepsilon_{Fe\text{-}N\text{-}C}$, $t_{Fe\text{-}N\text{-}C}$, $L_{Fe\text{-}N\text{-}C}$, and $\rho_{Fe\text{-}N\text{-}C}$ are the volume fraction, thickness, mass loading, and density of the Fe-N-C electrocatalyst, respectively. We made a reasonable assumption that ($\rho_{Fe\text{-}N\text{-}C} = \rho_{Carbon}$ =2000 kg/m^3).

iv) We note that the thermal conductivity values reported in the literature for MPLs vary between 0.1 and 0.3 W/(m.K).[4-6] Consequently, we used an average value of 0.2 W/(m.K) for the thermal conductivity of MPLs in our paper.

v) For GM-case, the membrane is Nafion and contains no ePTFE support. Consequently, the ionomer volume fraction in the membrane is one.[1, 3] The SA comprehensive report

suggests electrospun polyphenyl-sulfone as a potential lower-cost replacement for the ePTFE support currently used within the state-of-the-art supported membranes. The performance and durability of electrospun-supported membranes have yet to be demonstrated to meet or exceed ePTFE-supported membranes' current performance and durability status.[2] Consequently, we chose to keep ePTFE as the support in our membranes. According to the SA comprehensive report, a particular grade of non-expanded PTFE is used as a precursor material for ePTFE. A multi-stage, bi-axial mechanical stretching regiment is applied to the precursor to attain an optimized final fibril and node structure of the 0.95+ porous ePTFE.[2] The exact parameters of the stretching steps and presumable heat treatments are highly confidential to W. L. Gore & Associates, Inc and other high-quality FC grade ePTFE manufacturers.[2] Consequently, we used 0.95 as a reasonable value for the ionomer volume fraction in the membranes for both our base-case and 30 \$/kW$_{Net}$-case.

vi) We used the Zamel empirical correlation to calculate the tortuosity of the GDL (equation S3).[7]

$$\tau_{GDL} = \frac{\varepsilon_{GDL}}{\left\{1 - 2.76\varepsilon_{GDL}\cosh\left(3\varepsilon_{GDL} - 1.92\right)\left[\frac{3(1-\varepsilon_{GDL})}{(3-\varepsilon_{GDL})}\right]\right\}} \quad (S3)$$

In equation S3, ε_{GDL} and τ_{GDL} are the porosity and tortuosity of the GDL, respectively. We calculated the tortuosity of the MPL, anode/cathode, ionomer within the anode/cathode/membrane, and electronically conducting phase (i.e., carbon-supported electrocatalyst) within the anode/cathode using the Bruggeman correlation (equation S4).[8]

$$\tau = \varepsilon^{-0.5} \quad (S4)$$

In equation S4, ε is the porosity of the MPL, anode/cathode, the volume fraction of the ionomer within the anode/cathode/membrane, and the volume fraction of the electronically conducting phase (i.e., carbon-supported electrocatalyst) within the anode/cathode, and τ is the corresponding tortuosity.

vii) We adopted a hierarchical approach to calculate the thermal conductivity of the membrane.

$$k_{Ion,\ Hydrated} = \varepsilon_{Ion,\ Dry} k_{Ion,\ Dry} + \varepsilon_{H_2O,Ion} k_{H_2O,Ion} \quad (S5)$$

In equation S5, $k_{Ion,Hydrated}$, $k_{Ion,Dry}$, $k_{H2O,Ion}$, $\varepsilon_{Ion,Dry}$, and $\varepsilon_{H2O,Ion}$ are the thermal conductivity of the hydrated ionomer/dry ionomer/water absorbed within the ionomer, and volume fraction of dry ionomer/absorbed water within the hydrated ionomer, respectively. Subsequently, we calculated the membrane thermal conductivity using equation S6.

$$k_{Mem} = \varepsilon_{Ion,\ Hydrated} k_{Ion,\ Hydrated} + \varepsilon_{ePTFE} k_{ePTFE} \quad (S6)$$

In equation S6, $k_{Mem,}$ k_{ePTFE}, $\varepsilon_{Ion,Hydrated}$, and ε_{ePTFE} are the thermal conductivity of the membrane/ePTFE and volume fraction of ionomer/ePTFE within the membrane, respectively. We used reasonable values of 0.2, 0.569, and 0.25 W/(m.K) for $k_{Ion,Dry}$, $k_{H_2O,Ion}$, and k_{ePTFE}, respectively.[9, 10]

viii) We used a pseudo-two-component approach to calculate the effective diffusivity and molar flux of species i within the gas phase in our 1-D FC sandwich model.[11, 12] We calculated the molar flux of species i within the gas phase (N_i) using equation S7.

$$N_i = - D_i^{Eff} C_{Total} \nabla x_i \quad (S7)$$

In equation S7, D_i^{Eff} is the effective diffusivity, C_{Total} is the total gas phase concentration calculated using the total pressure assuming ideal gas law, and x_i is the mole fraction of species i. We calculated the effective diffusivity using equation S8.

$$D_i^{Eff} = \left(\frac{\varepsilon}{\tau}\right)\left(\frac{1}{1 - x_i}\right) D_i \quad (S8)$$

In equation S8, ε, τ, x_i, and D_i are the porosity and tortuosity of the medium where the gas diffusion happens (i.e., GDL, MPL, and electrocatalyst layer), the mole fraction of species i in the gas phase, and the diffusion coefficient of species i, respectively. We included the term $1/(1- x_i)$ to account for the effect of convective flux on molar flux in a pseudo-two-component gas mixture.[12] We calculated the diffusion coefficient of species i using the Bosanquet equation (equation S9).[11, 12]

$$D_i = \left(\frac{1}{D_{Knudsen,\, i}} + \frac{1}{D_{i\,,Mixture}}\right)^{-1} \quad (S9)$$

In equation S9, $D_{Knudsen,i}$ and $D_{i,Mixture}$ are the Knudsen and molecular diffusion coefficient of species i, respectively. We calculated the Knudsen diffusion coefficient using equation S10.[11, 12]

$$D_{Knudsen,\, i} = \frac{d_{Pore}}{3}\sqrt{\frac{8 R_g T}{\pi M_i}} \quad (S10)$$

In equation S10, d_{Pore}, R_g, T, and M_i are the mean pore size, universal gas constant, temperature, and molecular weight of species i, respectively. The current consensus in the FC literature is that Knudsen diffusion is negligible in the GDL, a small contributor

to the diffusion coefficient in the MPL, and a prominent contributor to the diffusion coefficient in the electrocatalyst layer.[11] Consequently, we neglected the Knudsen diffusion in the GDL. We used reasonable values of 55 and 300 nm for mean pore size in the electrocatalyst layer and MPL, respectively.[13, 14]

We calculated the molecular diffusion coefficient using the Wilke equation (equation S11).[11, 12]

$$D_{i:Mixture} = \left(\sum_{\substack{j=1 \\ j \neq i}}^{N_C} \frac{x_j^{'}}{D_{i,j}}\right)^{-1} \quad (S11)$$

In equation S11, $D_{i,j}$ and $x_j^{'}$ are the binary molecular diffusion coefficients and the mole fraction of component j in a gas mixture free of i. We calculated the binary molecular diffusion coefficients ($D_{i,j}$) using the equations detailed in the paper by Weber et al.[9]

ix) We used a reasonable value of 20 mΩ.cm^2 for the total area-specific electronic resistance. The total area-specific electronic resistance includes electronic contact resistances between the layers and the electronic resistance of GDLs and MPLs. Still, it does not include the electronic resistances originating from the electrocatalyst layers. We reasonably assumed the electronic conductivity (σ_{Cat}) of the carbon-supported electrocatalysts to be the same as that of the carbon support (120 S/cm).[9] We can calculate the electrocatalyst layers' effective electronic conductivity (σ^{Eff}) using equation S12.

$$\sigma^{Eff} = \left(\frac{\varepsilon}{\tau}\right)\sigma_{Cat} \quad (S12)$$

In equation S12, ε is the volume fraction of the electronically conducting phase (i.e.,

carbon-supported electrocatalyst) within the anode/cathode, and τ is the corresponding tortuosity.

x) To fully describe an ionomer's performance, we need to know its ionic conductivity (κ), its H_2O permeability ($D_{\hat{a},H_2O}$), and the number of H_2O molecules per charged group at equilibrium for that ionomer (λ).[15] For GM-case, the membrane is Nafion (EW=1100 g/mol), and the PEI in the electrodes is a PFSA-based ionomer with an EW of 950 g/mol.[1, 3] As detailed in the paper, most high-performance HEIs presently used in HEMs and HEMFC electrodes are hydrocarbon-based.[16-23] These HEIs are generally expected to be cheaper than PFSA-based PEIs currently used in state-of-the-art PEMFCs.[2, 24, 25] At this point, it is not clear which of these HEIs would be the final choice for implementation in HEMFCs, and unlike PFSA-based PEIs, the cost of these HEIs produced through optimized synthesis processes at large production volumes required for the production of 500,000 LDV systems/year is not known yet.[25] Consequently, for our base case, we decided to implement a HEI in both HEM and HEMFC electrodes that has the same κ, $D_{\hat{a},H_2O}$, and cost per mass as a PFSA-based PEI with an EW of 700 g/mol.

We note that we have synthesized PAP-TP-85 HEI in our lab, which is a poly (aryl piperidinium) HEI based on terphenyl, with 85 being the molar ratio between N-methyl-4-piperidone and aryl monomers (in percent), and the balance (15) composed of 2,2,2-trifluoroacetophenone.[20] And we have successfully implemented this HEI in our high-performance HEMFCs.[20, 26] Our in-lab measurements demonstrated that PAP-TP-85 has a lower density (1200 kg/m^3) than PFSA-based PEIs (2000 kg/m^3).

We reasonably assumed that the HEI in our technoeconomic analysis has the same density as PAP-TP-85. This assumption, combined with the assumption that the HEI in our technoeconomic analysis has the exact cost per mass as a 700 g/mol EW PFSA-based PEI, will result in a HEI with a lower cost per volume than a 700 g/mol EW PEI. Since the amount of the ionomer used in our model is dictated by its volume fraction in the membrane and electrodes, our cost and density assumptions will fully implement the conceptual construct of a cheaper HEI. The following sections will discuss implementing our cost estimation approach in more detail.

The choice of the 700 EW for PFSA-based PEI comes from the idea that, conceptually, what dictates the κ and $D_{\hat{a},H_2O}$ of a PEI or a HEI is the number of charged (cationic/anionic) groups per volume of that ionomer. One can calculate the number of charged (cationic/anionic) groups per volume of an ionomer using equation S13.

$$Number\ of\ charged\ groups\ per\ volume\ of\ an\ ionomer\left(\frac{mmol}{cm^3}\right) = IEC\left(\frac{mmol}{g}\right)\rho\left(\frac{g}{cm^3}\right) = \frac{1000\rho\left(\frac{g}{cm^3}\right)}{EW\left(\frac{g}{mol}\right)} \quad (S13)$$

In the above equation, IEC, ρ, and EW are the ion exchange capacity, density, and equivalent weight of an ionomer. Using equation S13, a 700 EW PEI with a density of 2000 kg/m^3 should have the same number of charged groups per volume and consequently comparable κ and $D_{\hat{a},H_2O}$ as a HEI with an IEC of 2.38 mmol/g and a density of 1200 kg/m^3. The IEC of 2.38 mmol/g favorably represents the IEC of PAP-TP-85,[20] and consequently, the 700 EW PEI properties should reasonably capture the

properties of a representative high-performance HEI. For the 30 \$/kW$_{Net}$-case, we assumed the HEI to have κ and $D_{\hat{a},H_2O}$ values three times that of 700 g/mol EW PEI at the exact cost as our base case's HEI.

Reference[27] presents the κ of several different EW PFSA-based PEIs (i.e., 1100, 825, 725, 620, and 438 g/mol EW) produced by 3M. The benchmark measurements performed by 3M show that at constant H_2O activity ($\hat{a}$), the κ of PFSA-based PEIs increases linearly on a log scale when EW decreases on an ordinary scale.[27] Consequently, we drew similar graphs at different values of $\hat{a}$ and we calculated the κ of 950 and 700 g/mol EW from the graphs (data not shown). Subsequently, we fitted suitable exponential functions to the κ of 1100, 950, and 700 g/mol EW PEIs. Equations S14, S15, and S16 present the κ in (S/m) functions for 1100, 950, and 700 g/mol EW PEIs at 80 °C vs. $\hat{a}$. We used a reasonable activation energy of (15 kJ/mol) to calculate κ at temperatures other than 80 °C.[15]

$$\kappa_{1100\ EW} = e^{(-3.3947\hat{a}^2 + 8.4271\hat{a} - 2.166)} \quad (S14)$$

$$\kappa_{950\ EW} = e^{(-3.0302\hat{a}^2 + 7.6364\hat{a} - 1.5437)} \quad (S15)$$

$$\kappa_{700\ EW} = e^{(-1.8874\hat{a}^2 + 5.8901\hat{a} - 0.3883)} \quad (S16)$$

The data for $D_{\hat{a},H_2O}$ of 1100[28] and 700[29] g/mol EW PEIs are available in the literature. We assumed reasonably that $D_{\hat{a},H_2O}$ shows a similar dependence on EW as does κ at a constant $\hat{a}$. This assumption means the $D_{\hat{a},H_2O}$ of PFSA-based PEIs increases linearly on a log scale when EW decreases on an ordinary scale at a constant $\hat{a}$. Consequently,

using a similar approach as described for κ, we calculated the $D_{\hat{a},H_2O}$ for 950 g/mol EW PEI. Finally, we fitted suitable polynomial functions to the $D_{\hat{a},H_2O}$ of 1100, 950, and 700 g/mol EW PEIs. Equations S17, S18, and S19 present the $D_{\hat{a},H_2O}$ in (mol/(m.s)) functions for 1100, 950, and 700 g/mol EW PEIs at 95 °C vs. $\hat{a}$. We used a reasonable activation energy of (20.1 kJ/mol) to calculate $D_{\hat{a},H_2O}$ at temperatures other than 95 °C.[15, 28]

$$D_{\hat{a},H_2O,1100\,EW} = 6.7 \times 10^{-5}\hat{a}^3 - 3.6 \times 10^{-5}\hat{a}^2 + 6.8 \times 10^{-6}\hat{a} + 5.6 \times 10^{-6} \quad (S17)$$

$$D_{\hat{a},H_2O,950\,EW} = 9.3 \times 10^{-5}\hat{a}^3 - 6.2 \times 10^{-5}\hat{a}^2 + 2.4 \times 10^{-5}\hat{a} + 4 \times 10^{-6} \quad (S18)$$

$$D_{\hat{a},H_2O,700\,EW} = 8.0 \times 10^{-5}\hat{a}^3 - 5.7 \times 10^{-5}\hat{a}^2 + 5.6 \times 10^{-5}\hat{a} - 3.9 \times 10^{-7} \quad (S19)$$

We calculated the effective κ and $D_{\hat{a},H_2O}$ of the ionomer in the membrane or electrodes using equation S20.

$$\kappa^{Eff} = \left(\frac{\varepsilon}{\tau}\right)\kappa \; and \; D_{\hat{a},H_2O}^{Eff} = \left(\frac{\varepsilon}{\tau}\right)D_{\hat{a},H_2O} \quad (S20)$$

In equation S20, ε and τ are the volume fraction of the ionomer in the membrane/electrode and the corresponding tortuosity of the ionomer in the membrane/electrode. We note that λ is independent of EW[27] and can be calculated using equation S21.[28]

$$\lambda = 0.043 + 17.81\hat{a} - 39.85\hat{a}^2 + 36.0\hat{a}^3 \quad (S21)$$

xi) We assumed all the ionomers in our paper have the same H_2 and O_2 permeation

coefficients (ψ_{H_2} and ψ_{O_2}; mol/(cm.s.bar)) as Nafion. One can calculate ψ_{H_2} and ψ_{O_2} of Nafion as a function of temperature and volume fraction of absorbed water within the hydrated ionomer ($\varepsilon_{H_2O,Ion}$) using the following correlations (E_{H2}=21 kJ/mol, E_{O2}=22 kJ/mol, and T_{Ref}=303 K).[15]

$$\psi_{H_2} = \left(0.29 + 2.2\varepsilon_{H_2O,Ion}\right) \times 10^{-11} e^{\left(E_{H_2}\left(\frac{1}{T_{Ref}} - \frac{1}{T}\right)\right)} \quad (S22)$$

$$\psi_{O_2} = \left(0.11 + 1.9\varepsilon_{H_2O,Ion}\right) \times 10^{-11} e^{\left(E_{O_2}\left(\frac{1}{T_{Ref}} - \frac{1}{T}\right)\right)} \quad (S23)$$

Next, we used the anode gas channel temperature and H_2O activity to calculate a value for ψ_{H_2} and cathode gas channel and H_2O activity to calculate another value for ψ_{H_2} and averaged these two values to get $\psi_{H_2,Avg}$. Similarly, we used the same approach to get a value for $\psi_{O_2,Avg}$. Subsequently, we calculated the crossover flux of H_2 and O_2 using equation S24.

$$N_{H_2,Crossover} = \left(\left(\frac{\varepsilon}{\tau}\right)\psi_{H_2,Avg}\frac{P_{H_2,Channel}}{t_{Mem}}\right)e_x \text{ and } N_{O_2,Crossover} = -\left(\left(\frac{\varepsilon}{\tau}\right)\psi_{O_2,Avg}\frac{P_{O_2,Channel}}{t_{Mem}}\right)e_x \quad (S24)$$

In equation S24, $P_{H_2,Channel}$, $P_{O_2,Channel}$, t_{Mem}, ε, τ, and e_x are the partial pressure of H_2/O_2 in the anode/cathode gas channels, membrane thickness, ionomer volume fraction/tortuosity in the membrane, and a vector of unit length in the positive x direction (Figure S1).

xii) For simplicity, we combined the GDL and MPL on FC's anode or cathode side into one

layer in our model named gas diffusion medium (GDM) using the idea of equivalent resistances. The GDM has a thickness equal to the combined thickness of GDL and MPL, and we can calculate the thermal conductivity of GDM (k_{GDM}), the diffusion coefficient of species i in the GDM ($D_i^{Eff,GDM}$), and the electronic conductivity of GDM (σ_{GDM}) using the following equations.

$$\frac{t_{GDM}}{k_{GDM}} = \frac{t_{GDL}}{k_{GDL}} + \frac{t_{MPL}}{k_{MPL}} + TCR_{FF-GDL} \quad (S25)$$

$$\frac{t_{GDM}}{D_i^{Eff,GDM}} = \frac{t_{GDL}}{D_i^{Eff,GDL}} + \frac{t_{MPL}}{D_i^{Eff,MPL}} \quad (S26)$$

$$\frac{t_{GDM}}{\sigma_{GDM}} = \frac{R_{Total,\,Electronic}}{2} \quad (S27)$$

In equations S25 to S27, $TCR_{FF\text{-}GDL}$ and $R_{Total,Electronic}$ are the thermal contact resistance between the flow field/GDL and the total area-specific electronic resistance. Please see Table S1 for the values of the parameters used to calculate the transport properties of the GDM.

The 1-D FC sandwich model considerations

We note that the mass, charge, and energy balance equations for the FC sandwich model described in the paper by Weber et al. are presented in their most general format using vector notations and are valid independent of the number of dimensions used in the FC sandwich model (1-D vs. 2-D).[9] Consequently, we adopted those balance equations for our 1-D FC sandwich model. We solved them numerically in MATLAB using the dimensions of the modeling domains and transport parameters described in Table S1, subject to the following considerations.

i) We neglected multiphase flow in our 1-D FC sandwich model. Consequently, all the terms pertaining to multiphase flow would be eliminated from the balance equations. We also ignored the formation of any liquid H_2O in our 1-D FC sandwich model. Consequently, all the terms pertaining to the formation of liquid H_2O would be eliminated from the balance equation. In our 1-D FC sandwich model, we allowed the H_2O partial pressure to rise above the H_2O saturation pressure, but we capped the H_2O activity at 1, which prevents any properties that depend on H_2O activity (e.g., ionic conductivity, H_2O permeability, etc.) from exceeding their values for a H_2O activity of 1.

ii) For PEMFC, we reasonably assumed that there is no pH gradient in the MEA and that the PEI provides an effective pH of 0 in the MEA. We note that our HEMFC LDV system incorporates an EDCS unit which reduces the cathode inlet CO_2 concentration to 4 ppm. We also assumed intermittent electrochemical purges would be applied to the HEMFC stack at the time of refueling of the LDV. These considerations mean that the negative impact of CO_2 on the HEMFC performance is mitigated. Consequently, 1) We reasonably assumed that there is no pH gradient in the MEA of HEMFC and that the HEI provides an effective pH of 14 in the MEA, and 2) We eliminated all the terms pertaining to the formation/consumption of CO_2, CO_3^{-2}, and HCO_3^- from the balance equations.

iii) In a FC, the O_2 in the cathode gets consumed through the ORR. For a PEMFC, the ORR reaction stoichiometry and kinetics are as follows:[30]

$$O_2 + 4H^+ + 4e^- \rightarrow 2H_2O \quad (S28)$$

$$i_{0,ORR}^{E_{ORR}^{Ref}} = i_{0,Ref,ORR}^{E_{ORR}^{Ref}} e^{\left(\frac{-E_{A,ORR}}{R_g}\left(\frac{1}{T}-\frac{1}{T^{Ref}}\right)\right)} \quad (S29)$$

$$i_{ORR} = -i_{0,ORR}^{E_{ORR}^{Ref}} \hat{a}_{O_2}^{m_{O_2}} e^{\left(-\frac{\alpha_c^{ORR} F}{R_g T}\left(\varphi_1 - \varphi_2 - E_{ORR}^{Ref}\right)\right)} \quad (S30)$$

Equation S29 defines the ORR electrocatalyst-specific current density ($i_{0,ORR}^{E_{ORR}^{Ref}}$; A/m$^2_{ECSA}$) using i) the ORR electrocatalyst-specific reference current density ($i_{0,Ref,ORR}^{E_{ORR}^{Ref}}$; A/m$^2_{ECSA}$) measured at a reference potential of (E_{ORR}^{Ref}= 0.9 V vs. reversible hydrogen electrode (RHE)), a reference O_2 partial pressure of 1 atm, and a reference temperature (T_{Ref}) of 25 °C, and ii) an ORR activation energy ($E_{A,ORR}$).[30] Equation S30 is a Tafel equation for the ORR electrocatalyst-specific current density (i_{ORR}; A/m$^2_{ECSA}$).[30, 31] In Equation S30, $\hat{a}_{O_2}$, m_{O_2}, α_c^{ORR}, F, φ_1, and φ_2 are the O_2 activity, the ORR reaction order with regard to O_2 activity, the ORR cathodic charge transfer coefficient, Faraday's constant, electronic potential, and ionic potential.[30, 31] Based on the comprehensive studies of the ORR kinetics on Pt/C in PEMFCs performed by GM, we assigned values of 10 kJ/mol, 0.79, and 1 to $E_{A,ORR}$, m_{O_2}, and α_c^{ORR}.[30] For a HEMFC, the ORR reaction stoichiometry and kinetics are as follows:[9]

$$O_2 + 2H_2O + 4e^- \rightarrow 4OH^- \quad (S31)$$

$$i_{0,ORR}^{E_{ORR}^{Ref}} = i_{0,Ref,ORR}^{E_{ORR}^{Ref}} e^{\left(\frac{-E_{A,ORR}}{R_g}\left(\frac{1}{T}-\frac{1}{T^{Ref}}\right)\right)} \quad (S32)$$

$$i_{ORR} = -i_{0,ORR}^{E_{ORR}^{Ref}} \hat{a}_{O_2}^{m_{O_2}} \hat{a}_{H_2O}^{m_{H_2O}} e^{\left(-\frac{\alpha_c^{ORR} F}{R_g T}\left(\varphi_1 - \varphi_2 - E_{ORR}^{Ref}\right)\right)} \quad (S33)$$

Equation S32 defines the ORR electrocatalyst-specific current density ($i_{0,ORR}^{E_{ORR}^{Ref}}$; A/m^2_{ECSA}) using i) the ORR electrocatalyst-specific reference current density ($i_{0,Ref,ORR}^{E_{ORR}^{Ref}}$; A/m^2_{ECSA}) measured at a reference potential of (E_{ORR}^{Ref}), a reference O_2 partial pressure of 1 atm, a reference H_2O partial pressure of 1 atm, and a reference temperature (T_{Ref}) of 25 °C, and ii) an ORR activation energy ($E_{A,ORR}$). In equation S33, $\hat{a}_{H_2O}$ and m_{H_2O} are the H_2O activity and the ORR reaction order with regard to H_2O activity. The definition of the rest of the parameters in equation S33 is the same as the parameters in equation S30. If one makes the reasonable assumption of no kinetic dependence in the oxygen evolution direction on $\hat{a}_{H_2O}$, then m_{H_2O} is constrained by thermodynamics to be $\frac{\alpha_a^{ORR} + \alpha_c^{ORR}}{2}$ with α_a^{ORR} being the ORR anodic charge transfer coefficient. In equation S33, we assumed the same values for $E_{A,ORR}$, m_{O_2}, α_c^{ORR}, and α_a^{ORR} as those assumed for PEMFCs (i.e., 10 kJ/mol, 0.79, 1, and 1).[9, 30] Consequently, m_{H_2O} will have a value of 1.[9]

iv) In a FC, the H_2 in the anode gets consumed through the HOR. For a PEMFC, the HOR reaction stoichiometry and kinetics are as follows:[32]

$$H_2 \rightarrow 2H^+ + 2e^- \quad (S34)$$

$$i_{0,HOR} = i_{0,Ref,HOR}\, e^{\left(\frac{-E_{A,HOR}}{R_g}\left(\frac{1}{T}-\frac{1}{T^{Ref}}\right)\right)} \quad (S35)$$

$$i_{HOR} = i_{0,HOR}\left\{\hat{a}_{H_2}{}^{m_{H_2}} e^{\left(\frac{\alpha_a^{HOR} F}{R_g T}\left(\varphi_1-\varphi_2-E^{\circ}_{HOR}\right)\right)} - e^{\left(-\frac{\alpha_c^{HOR} F}{R_g T}\left(\varphi_1-\varphi_2-E^{\circ}_{HOR}\right)\right)}\right\} \quad (S36)$$

Equation S35 defines the HOR electrocatalyst-specific exchange current density ($i_{0,HOR}$; A/m^2_{ECSA}) using i) the HOR electrocatalyst-specific reference exchange current density ($i_{0,Ref,HOR}$; A/m^2_{ECSA}) measured at a reference H_2 partial pressure of 1 atm and a reference temperature (T_{Ref}) of 25 °C, and ii) a HOR activation energy ($E_{A,HOR}$). Equation S36 is a Butler-Volmer equation for the HOR electrocatalyst-specific current density (i_{HOR}; A/m^2_{ECSA}).[31, 32] In Equation S36, $\hat{a}_{H_2}$, m_{H_2}, α_a^{HOR}, α_c^{HOR}, F, φ_1, φ_2, and E°_{HOR} are the H_2 activity, the HOR reaction order with regard to H_2 activity, the HOR anodic charge transfer coefficient, the HOR cathodic charge transfer coefficient, Faraday's constant, electronic potential, ionic potential, and the standard HOR equilibrium potential.[31] If one makes the reasonable assumption of no kinetic dependence in the hydrogen evolution direction on $\hat{a}_{H_2}$, then $m_{H_2}$is constrained by thermodynamics to be $\frac{\alpha_a^{HOR}+\alpha_c^{HOR}}{2}$. Based on the comprehensive studies of the HOR kinetics on Pt/C performed in acidic media, we assigned values of 16 kJ/mol, 0.5, and 0.5 to $E_{A,HOR}$, α_a^{HOR}, and α_c^{HOR}.[32-34] Consequently, m_{H_2} will have a value of 0.5. For a HEMFC, the HOR reaction stoichiometry and kinetics are as follows:[9]

$$H_2 + 2OH^- \rightarrow 2H_2O + 2e^- \quad (S37)$$

$$i_{0,HOR} = i_{0,Ref,HOR}\, e^{\left(\frac{-E_{A,HOR}}{R_g}\left(\frac{1}{T}-\frac{1}{T^{Ref}}\right)\right)} \quad (S38)$$

$$i_{HOR} = i_{0,HOR}\left\{\hat{a}_{H_2}{}^{m_{H_2}} e^{\left(\frac{\alpha^{HOR}_{a} F}{R_g T}\left(\varphi_1 - \varphi_2 - E^{\circ}_{HOR}\right)\right)} - \hat{a}_{H_2O}{}^{m_{H_2O}} e^{\left(-\frac{\alpha^{HOR}_{c} F}{R_g T}\left(\varphi_1 - \varphi_2 - E^{\circ}_{HOR}\right)\right)}\right\} \quad (S39)$$

Equation S38 defines the HOR electrocatalyst-specific exchange current density ($i_{0,HOR}$; A/m^2_{ECSA}) using i) the HOR electrocatalyst-specific reference exchange current density ($i_{0,Ref,HOR}$; A/m^2_{ECSA}) measured at a reference H_2 partial pressure of 1 atm, a reference H_2O partial pressure of 1 atm, and a reference temperature (T_{Ref}) of 25 °C, and ii) a HOR activation energy ($E_{A,HOR}$). In equation S39, $\hat{a}_{H_2O}$ and m_{H_2O} are the H_2O activity and the hydrogen evolution reaction (HER) reaction order with regard to H_2O activity. The definition of the rest of the parameters in equation S39 is the same as the parameters in equation S36. If one makes the reasonable assumption of no kinetic dependence in the hydrogen evolution direction on $\hat{a}_{H_2}$ and no kinetic dependence in the hydrogen oxidation direction on $\hat{a}_{H_2O}$, then $m_{H_2}$and m_{H_2O} are constrained by thermodynamics to be $\frac{\alpha^{HOR}_{a} + \alpha^{HOR}_{c}}{2}$ and $\alpha^{HOR}_{a} + \alpha^{HOR}_{c}$ respectively.[9] The HOR electrocatalysts used in our HEMFC model have different values of α^{HOR}_{a} and α^{HOR}_{c} as noted in Figure S2-2. We assumed that all of the HOR electrocatalysts used in our HEMFC model have the same $E_{A,HOR}$ as that of Pt/C in alkaline media

(29.5 kJ/mol).[34]

v) We summarized the electrocatalyst properties relevant to the kinetics of the ORR and the HOR in Figure S2 and its caption. We note that we compared the intrinsic activity of the HOR electrocatalysts using a generalized exchange current density defined as ($i_{HOR}(\alpha_{a}^{HOR} + \alpha_{C}^{HOR})$). We chose this because linearization of the Butler–Volmer HOR rate equation at small overpotentials and 1 atm partial pressure shows that the HOR overpotential is inversely proportional to the generalized exchange current density.[32] We note that for GM-case, the ORR electrocatalyst is 33.38 wt.% PtCo/high surface area carbon (HSC) with an ECSA of 45 m^2/g and a mass activity of 0.503 A/mg ($E_{ORR}^{Ref} = 0.9\ V\ vs.\ RHE$, 80 °C, and 1 atm partial pressure).[3] Furthermore, the HOR electrocatalyst is 20 wt.% Pt/HSC, whose properties we presented in Figure S2-2 and its caption.[3]

vi) We assumed that the O_2 that crossed over to the anode side of FC would go through the ORR (equation S28 for PEMFC and equation S31 for HEMFC) with a constant electrode-volume normalized rate of O_2 consumption of ($\frac{N_{O_2,Crossover}}{t_{ACl}}$). Similarly, we assumed that the H_2 that crossed over to the cathode side of FC would go through the HOR (equation S34 for PEMFC and equation S37 for HEMFC) with a constant electrode-volume normalized rate of H_2 consumption of ($\frac{N_{H_2,Crossover}}{t_{CCl}}$).

vii) For PEMFC, we assumed an electro-osmotic drag coefficient of one for H^+, meaning that a H^+ ion would carry a H_2O molecule with itself as it goes from the anode to the cathode side of the PEMFC.[35] Similar to Weber et al., for HEMFC, we assumed an

electro-osmotic drag coefficient of one for OH^-, meaning that an OH^- ion would carry a H_2O molecule with itself as it goes through from the cathode to the anode side of the HEMFC.[9]

viii) In our 1D-MEA model, we included a local-O_2 transport resistance term ($R_{O_2}^{Local}$; s/cm) to model the O_2 transport through the ionomer in the cathode electrocatalyst layer. [3, 11, 36] Detailed discussions of this resistance are beyond the scope of our paper, and we refer interested readers to the benchmark GM's paper authored by Kongkanand and Mathias for excellent discussions of this resistance.[3] We note that the current consensus in the FC community is that this resistance causes major voltage loss at technologically important high current density (HCD) region of FC polarization curves for low cathode electrocatalyst loadings.[3] Consequently, one needs to include this resistance in any FC model that aims to accurately predict the HCD region of FC polarization curves, especially at low cathode electrocatalyst loadings.[3] The presence of $R_{O_2}^{Local}$ decreases the O_2 partial pressure at the surface of the ORR electrocatalyst ($P_{O_2}^{Surface}$) compared to the gas phase O_2 partial pressure ($P_{O_2}^{Gas}$) as described by Equation S40.[3, 11]

$$P_{O_2}^{Surface} = P_{O_2}^{Gas} + R_g T R_{O_2}^{Local} \frac{i_{ORR}}{4F} \quad (S40)$$

In equation S40, i_{ORR} is the ORR electrocatalyst-specific current density (equation S30 for PEMFC and equation S33 for HEMFC) calculated using an O_2 activity ($\hat{a}_{O_2}$) evaluated based on $P_{O_2}^{Surface}$.[3, 11] We note that GM's studies of well-optimized

electrodes prepared using PtNi/HSC and PtCo/HSC ORR electrocatalysts show that 25 s/cm is a reasonable estimate for $R_{O_2}^{Local}$.[3] Consequently, for GM-case and base-case, we assumed $R_{O_2}^{Local}$ to be 25 s/cm. Recently, GM has developed a specially designed carbon support with cleverly engineered mesoporous morphology that enables reducing $R_{O_2}^{Local}$ to 6 s/cm.[36] Consequently, for the 30 \$/kW$_{Net}$ case, we assumed $R_{O_2}^{Local}$ to be 6 s/cm.

ix) Inspired by the paper authored by Weber et al., we applied the flowing boundary conditions in our 1-D FC sandwich model.[9] At each electrocatalyst layer/membrane interface, we assumed the H_2 and O_2 fluxes to be equal to the crossover flux of H_2 and O_2 (equation S24) and imposed no-flux boundary conditions for other gas phase species. We assumed no-flux boundary conditions at each electrocatalyst layer/GDL interface for ions and ionomer-absorbed water and at each electrocatalyst layer/membrane interface for electronic current. We set the temperature of the channel/GDL interface at the anode and cathode to the temperatures of the anode and cathode gas channels, respectively. At the gas channel/GDL interface, we set each gaseous species' partial pressure to that species' partial pressure in the gas channel. We set the electronic potential (φ_1) to 0 V at the anode gas channel/GDL interface and to the applied FC potential at the cathode gas channel/GDL interface. In all other cases, we assumed a variable that exists on both sides of an interface to be continuous across that interface.

One-dimensional (1-D) down-the-channel model

In our modeling approach, we assumed that there is no temperature variation along the anode/cathode gas channels and that the temperature in the anode/cathode gas channel is equal to the specified FC operational temperature. Our 1-D down-the-channel model consists of mass balance down the channel for the species present in the channel coupled with an assumption of linear total pressure drop along the flow channels. The following mass balance equations and their associated boundary conditions describe the flow variations along the z-direction (Figure S1) of total pressure (P_{Total}^{AGC}) and molar flow rates of H_2 and H_2O ($n_{H_2}^{AGC}$ *and* $n_{H_2O}^{AGC}$; mol/s) in the anode gas channel (equations S41 to S43).

$$\frac{dP_{Total}^{AGC}(z)}{dz} = \frac{\Delta P_{Total}^{AGC}}{l_{MEA}} \; and \; P_{Total}^{AGC}(z = l_{MEA}) = P_{Total-Inlet}^{AGC} \quad (S41)$$

$$\frac{dn_{H_2}^{AGC}(z)}{dz} = \left|N_{H_2}(x=0,z)\right| w_{MEA} = \frac{w_{MEA}}{2F}\left(i_{1D-MEA}(z) + 2F\left|N_{H_2,Crossover}(z)\right| + 4F\left|N_{O_2,Crossover}(z)\right|\right) \quad (S42-1)$$

$$n_{H_2}^{AGC}(z = l_{MEA}) = n_{H_2-Inlet}^{AGC} = \frac{S_{Anode}}{2F}\left(w_{MEA}\int_{z=0}^{z=l_{MEA}} i_{1D-MEA}(z)dz\right) \quad (S42-2)$$

$$\frac{dn_{H_2O}^{AGC}(z)}{dz} = \left|N_{H_2O}(x=0,z)\right| \delta_{H_2O}^{AGC} w_{MEA} \; and \; n_{H_2O}^{AGC}(z = l_{MEA}) = n_{H_2O-Inlet}^{AGC} \quad (S43)$$

In equation S41, ΔP_{Total}^{AGC}, $P_{Total-Inlet}^{AGC}$, and l_{MEA} are the anode gas channel pressure drop, anode gas channel inlet total pressure, and length of the MEA, respectively. In equations S42-1 and S42-2, $\left|N_{H_2}(x=0,z)\right|$, $\left|N_{H_2,Crossover}(z)\right|$, $\left|N_{O_2,Crossover}(z)\right|$, $i_{1D-MEA}(z)$, w_{MEA}, and S_{Anode} are the norm of H_2 flux at (x=0,z)/H_2 crossover flux/O_2 crossover flux, local geometric

current density associated with the 1D-MEA slice located at point z in the anode/cathode gas channel, width of the MEA, and anode stoichiometry, respectively. In equation S43, $\left|N_{H_2O}(x=0,z)\right|$, $\delta_{H_2O}^{AGC}$, and $n_{H_2O-Inlet}^{AGC}$ are the norm of H_2O flux at (x=0,z), anode gas channel water transport direction adjustment parameter, and molar flux of H_2O at the inlet of the anode gas channel, respectively. We note that $\delta_{H_2O}^{AGC}$ is a parameter that has been introduced to the anode gas channel H_2O balance (equation S43) to correctly account for the direction of the H_2O flux into or out of the 1-D MEA slice located at point z in the anode/cathode gas channel ($\delta_{H_2O}^{AGC}$=1 if $N_{H_2O}(x=0,z)$ points into the 1-D MEA slice and $\delta_{H_2O}^{AGC}$=− 1 if $N_{H_2O}(x=0,z)$ points out of the 1-D MEA slice). We note that the ideal gas law provides the partial pressure of H_2 ($P_{H_2}^{AGC}(z)$) and H_2O ($P_{H_2O}^{AGC}(z)$) at any point in the anode gas channel (equation S44).

$$P_{H_2}^{AGC}(z)=\frac{n_{H_2}^{AGC}(z)P_{Total}^{AGC}(z)}{n_{H_2}^{AGC}(z)+n_{H_2O}^{AGC}(z)}\ and\ P_{H_2O}^{AGC}(z)=\frac{n_{H_2O}^{AGC}(z)P_{Total}^{AGC}(z)}{n_{H_2}^{AGC}(z)+n_{H_2O}^{AGC}(z)}\quad (S44)$$

The following mass balance equations and their associated boundary conditions describe the flow variations along the z-direction (Figure S1) of total pressure (P_{Total}^{CGC}) and molar flow rates of O_2 , H_2O, and N_2 ($n_{O_2}^{CGC}$, $n_{H_2O}^{CGC}$, $and\ n_{N_2}^{CGC}$; mol/s) in the cathode gas channel (equations S45 to S48).

$$\frac{dP_{Total}^{CGC}(z)}{dz}=-\frac{\Delta P_{Total}^{CGC}}{l_{MEA}}\ and\ P_{Total}^{CGC}(z=0)=P_{Total-Inlet}^{CGC}\quad (S45)$$

$$\frac{dn_{O_2}^{CGC}(z)}{dz}=-\left|N_{O_2}(x=t_{MEA},z)\right|w_{MEA}=\frac{-w_{MEA}}{4F}\left(i_{1D-MEA}(z)+2F\left|N_{H_2,Crossover}(z)\right|+4F\right|-1)$$

$$n_{O_2}^{CGC}(z=0) = n_{O_2-Inlet}^{CGC} = \frac{S_{Cathode}}{4F}\left(w_{MEA}\int_{z=0}^{z=l_{MEA}} i_{1D-MEA}(z)dz\right) \quad (S46-2)$$

$$\frac{dn_{H_2O}^{CGC}(z)}{dz} = \left|N_{H_2O}(x=t_{MEA},z)\right|\delta_{H_2O}^{CGC} w_{MEA} \text{ and } n_{H_2O}^{CGC}(z=0) = n_{H_2O-Inlet}^{CGC} \quad (S47)$$

$$n_{N_2}^{CGC}(z) = n_{N_2-Inlet}^{CGC} = \frac{1-x_{O_2}^{Dry\ air-Adjusted}}{x_{O_2}^{Dry\ air-Adjusted}} \frac{S_{Cathode}}{4F}\left(w_{MEA}\int_{z=0}^{z=l_{MEA}} i_{1D-MEA}(z)dz\right) =$$
$$= \frac{x_{O_2}^{Dry\ air}}{1+f_{O_2}\times(1-x_{O_2}^{Dry\ air})}; \quad x_{O_2}^{Dry\ air} = 0.21 \quad (S48)$$

In equation S45, ΔP_{Total}^{CGC}, $P_{Total-Inlet}^{CGC}$, and l_{MEA} are the cathode gas channel pressure drop, anode gas channel inlet total pressure, and length of the MEA, respectively. In equations S46-1 and S46-2, $\left|N_{O_2}(x=t_{MEA},z)\right|$, $\left|N_{H_2,Crossover}(z)\right|$, $\left|N_{O_2,Crossover}(z)\right|$, $i_{1D-MEA}(z)$, w_{MEA}, and $S_{Cathode}$ are the norm of O_2 flux at (x=t_{MEA},z)/H_2 crossover flux/O_2 crossover flux, local geometric current density associated with the 1D-MEA slice located at point z in the anode/cathode gas channel, width of the MEA, and cathode stoichiometry, respectively. In equation S47, $\left|N_{H_2O}(x=t_{MEA},z)\right|$, $\delta_{H_2O}^{CGC}$, and $n_{H_2O-Inlet}^{CGC}$ are the norm of H_2O flux at (x= t_{MEA},z), cathode gas channel water transport direction adjustment parameter, and molar flux of H_2O at the inlet of the cathode gas channel, respectively. We note that $\delta_{H_2O}^{CGC}$ is a parameter that has been introduced to the cathode gas channel H_2O balance (equation S47) to correctly account for the direction of the H_2O flux into or out of the 1-D MEA slice located at point z in the anode/cathode gas channel ($\delta_{H_2O}^{CGC}$=1 if $N_{H_2O}(x=t_{MEA},z)$ points out of the 1-D MEA slice and $\delta_{H_2O}^{CGC}$=-1 if $N_{H_2O}(x=t_{MEA},z)$

points into the 1-D MEA slice). In equation S48, $n_{N_2}^{CGC-Inlet}$ and $x_{O_2}^{Dry\ air}$ are the molar flux of N_2 at the inlet of the cathode gas channel and the mole fraction of O_2 in dry air (0.21). We note that due to the consumption of O_2 in the EDCS unit, the mole fraction of O_2 on a dry basis entering the stack ($x_{O_2}^{Dry\ air-Adjusted}$) is smaller than the scenario in which no EDCS is present in the FC system. The parameter f_{O_2} in equation S48 is the ratio of the molar flow rate of O_2 consumed in the EDCS unit to the molar flow rate of O_2 entering the stack, and we will discuss this parameter and its effects later in the ESI in detail (for PEMFC, $f_{O_2}=0$).

We note that the ideal gas law provides the partial pressure of O_2 ($P_{O_2}^{CGC}(z)$), H_2O ($P_{H_2O}^{CGC}(z)$), and N_2 ($P_{N_2}^{CGC}(z)$) at any point in the cathode gas channel (equation S49).

$$P_{O_2}^{CGC}(z) = \frac{n_{O_2}^{CGC}(z)P_{Total}^{CGC}(z)}{n_{O_2}^{CGC}(z)+n_{H_2O}^{CGC}(z)+n_{N_2}^{CGC}(z)},\ P_{H_2O}^{CGC}(z) = \frac{n_{H_2O}^{CGC}(z)P_{Total}^{CGC}(z)}{n_{O_2}^{CGC}(z)+n_{H_2O}^{CGC}(z)+n_{N_2}^{CGC}(z)}\ and\ P^{C} \quad (S49)$$

Similar to the paper by Weber et al., we explicitly implemented the condensation of liquid H_2O in the gas channels.[9] If the partial pressure of water (P_{H_2O}) at any point in the gas channels became higher than the H_2O saturation pressure ($P_{H_2O}^{Sat}$), we set ($P_{H_2O}=P_{H_2O}^{Sat}$) and we apportioned the molar flow rate of H_2O (n_{H_2O}; mol/s) into the vapor phase ($n_{H_2O}^{V}$; mol/s) and liquid phase ($n_{H_2O}^{L}$; mol/s) components using S50 and S51.

$$n_{H_2O}^{V} = \frac{P_{H_2O}^{Sat}}{(P_{Total}^{GC}-P_{H_2O}^{Sat})_{i\neq H_2O}}\sum n_i \quad (S50)$$

$$n_{H_2O}^{L} = n_{H_2O} - n_{H_2O}^{V} \quad (S51)$$

In equation S50, P_{Total}^{GC} and n_i are the total pressure in the gas channel and the molar flow rate of component i (mol/s) in the gas channel.

We note that in the SA comprehensive report, the pressure drop of the cathode side of the stack is specified to be 0.24 atm for the 2018 LDV system.[2] We reasonably assumed that this pressure drop is primarily due to the pressure drop within the cathode side of a single cell in the stack and that the pressure drop on the cathode side and anode side of a single cell are equal. Consequently, we set $\Delta P_{Total}^{AGC} = \Delta P_{Total}^{CGC} = 0.24\ atm.$ SA comprehensive report specifies the active area of a single cell for the 2018 LDV system as 197 cm^2.[2] We reasonably assumed that this single cell has the same ratio of (l_{MEA}/w_{MEA}) as that of Toyota Mirai ($l_{MEA,Toyota\ Mirai}$=13.36 cm and $w_{MEA,Toyota\ Mirai}$=20 cm).[2] Consequently, the l_{MEA} and w_{MEA} of the 2018 LDV system would be 11.47 cm and 17.17 cm, respectively. Accordingly, in all our modeling work, we assumed that $\frac{\Delta P_{Total}^{AGC}}{l_{MEA}} = \frac{\Delta P_{Total}^{CGC}}{l_{MEA}} = \frac{0.24\ atm}{11.47\ cm} = 2.12 \times 10^5\ Pa/m$. For GM-case, the PEMFC operating in counter-flow mode is a 50 cm^2 active area single cell ($l_{MEA}=w_{MEA}$=7.07 cm).[3] For our base-case and 30 \$/kW_{Net}-case, we assumed a constant value of l_{MEA}=11.47 cm for a single cell. This assumption has the significant advantage that it makes the cell average geometric current density (i_{Cell}) independent of the cell area (note that in our 1-D MEA model, no variations exist in the dimension associated with w_{MEA}; Figure S1). Consequently, we set w_{MEA} to an arbitrarily chosen value of 17.17 cm to perform our pseudo-2-D FC model. As we will discuss later in this ESI, we updated w_{MEA} in our cost estimation efforts for our base-case and 30 \$/kW_{Net}-case to its required value based on the system power and voltage requirements.

Our pseudo-2-D FC model corresponds to a FC operating in counter-flow mode. In this operation mode, the anode gas channel exit is adjacent to the cathode gas channel inlet, and the anode gas channel inlet is adjacent to the cathode gas channel exit (Figure S1). Since we do not know the exit conditions of the anode/cathode gas channels a priori, solving the pseudo-2-D FC model requires an elaborative and very time-consuming iterative guess and check approach. In this approach, we guessed the cell average current density and the exit composition of the anode gas channel. Subsequently, we ran the pseudo-2-D FC model iteratively, renewing the guessed values several times until the inlet conditions of the anode gas channel and anode/cathode calculated stoichiometry matched the known values. We note that the 1-D FC sandwich model is already quite computationally expensive, and the need to run the pseudo-2-D FC model iteratively several times makes acquiring results in a reasonable time impractical. Therefore, we implemented the below-described sensible approach, which maintains the underlying physics of the 1-D FC sandwich model in our pseudo-2-D FC model execution while enabling much faster execution times for our pseudo-2-D FC model. We note that to run our pseudo-2-D FC model, we only need to know $i_{1D-MEA}(z)$, $N_{H_2O}(x=0,z)$, and $N_{H_2O}(x=t_{MEA},z)$ (equations S41 to S51). We note that $N_{H_2O}(x=0,z)$ and $N_{H_2O}(x=t_{MEA},z)$ are dependent on each other through the flux of the total amount of H_2O produced in the 1-D MEA slice, as described in equation S52. Therefore, just knowing one of them is enough to know the other.

$$\left|N_{H_2O}(x=t_{MEA},z)\right|\delta_{H_2O}^{CGC} = \left|N_{H_2O}(x=0,z)\right|\delta_{H_2O}^{AGC} + \frac{1}{2F}\left(i_{1D-MEA}(z) + 2F\left|N_{H_2,Crossover}(z)\right| + 4F\left|N_{O_2,Crossover}(z)\right|\right) \quad (S52)$$

We note $i_{1D-MEA}(z)$ and $N_{H_2O}(x=t_{MEA},z)$ are only a function of six independent variables:

FC voltage, total anode pressure, relative humidity of anode, total cathode pressure, relative humidity of cathode, and O_2 mole fraction in the cathode on a dry basis. Consequently, we formed a 6-D matrix of the values of six independent variables: FC voltage values (29 equidistant points varying between 0.9 V to 0.55 V), total anode pressure values (3 equidistant points varying between the total anode inlet pressure and total anode outlet pressure), relative humidity of anode (10 equidistant points varying between 1 to 0.65), total cathode pressure values (3 equidistant points varying between the total cathode inlet pressure and total cathode outlet pressure), relative humidity of cathode (10 equidistant points varying between 1 to 0.65), and O_2 mole fraction in the cathode on a dry basis (10 equidistant points varying between 0.21 to 0.0706). Subsequently, we ran the 1-D FC sandwich model over the 6-D matrix of the values of six independent variables and stored the results in a matrix. Finally, at the time of pseudo-2-D FC model execution, at each point z in the gas channels, we used the matrix of results and the matrix of independent variables' values and performed a cubic spline interpolation to calculate $i_{1D-MEA}(z)$ and $N_{H_2O}(x = t_{MEA}, z)$.

Validation of 1-D FC sandwich and pseudo-2-D FC models

We validated our 1-D FC sandwich and pseudo-2-D FC models by comparing their results with benchmark PEMFC experimental polarization curves provided by GM for cells operating in either differential mode (5 cm^2 active area single cell) or counter-flow mode (50 cm^2 active area single cell).[3] Figure 2 in the paper compares the experimental polarization curve with the model polarization curve for PtCo/HSC cathode (Pt loadings=0.2 mg_{Pt}/cm^2) coupled with Pt/HSC anode (Pt loadings=0.025 mg_{Pt}/cm^2) for PEMFCs operating either in differential mode or counter-flow mode. We included similar comparisons for two other PtCo/HSC cathodes at different Pt loadings (0.1 and 0.05 mg_{Pt}/cm^2) coupled with Pt/HSC anode (Pt loadings=0.025 mg_{Pt}/cm^2) in Figures S3 and S4. Close inspection of Figures 2, S3, and S4 shows that the overall agreement between

polarization curves produced by our 1-D FC sandwich model or our pseudo-2-D FC model and the GM's benchmark experimental ones is very reasonable.

Description of the correction term which accounts for the single-cell voltage loss resulting from the buildup of N_2 in the recirculating anode gas in FC stacks of LDVs

We note that the FC stacks of LDVs operate at considerably less than 100% H_2 utilization per pass in the anode. Consequently, the bulk of the spent anode outlet gas containing unconverted H_2 must be recycled towards the anode inlet to maintain reasonable energy conversion efficiency.[37, 38] In FCs in LDVs, N_2 diffuses across the membrane from the cathode side to the anode side. Recycling the anode exit gas to the anode inlet significantly builds up the N_2 concentration within the recirculating anode gas, which causes unacceptable levels of FC performance degradation.[37, 38] Consequently, in practice, a portion of the recirculating anode gas is purged to prevent excessive buildup of the N_2 in the anode gas and maintain FC performance degradation at acceptable levels.[37, 38] We note that the anode purge rate of a FC stack depends on the purge method, and it can be in the range of 0.7%–1.2% of H_2 fed to the FC.[37, 38] The available estimates in the literature show that upon implementation of the anode purge strategy, the single cell voltage degradation in a PEMFC stack with a stack gross power of between 80 kW_{Gross} and 90 kW_{Gross}, corresponding to a stack delivering 80 kW_{Net} power, would be only around 1 mV.[38] Consequently, in our FC LDV system cost estimation studies, after acquiring the FC polarization curves, we applied a N_2 buildup voltage degradation ($\Delta V_{N_2\ buildup}$) of 1 mV to the polarization curves. This way, we have reasonably accounted for the single-cell voltage loss which results from the buildup of N_2 in the recirculating anode gas of a FC stack with implemented anode purge.

The mathematical definition of voltage-loss terms calculated from our pseudo-2-D FC model results

Inspired by the voltage-loss calculations presented in the paper authored by Weber et al.,[9] we calculated the kinetic voltage loss, ionic Ohmic voltage loss, electronic Ohmic voltage loss, and concentration voltage loss using the below equations. We first calculated an average geometric current density for a single cell ($i_{Cell,Avg}$) using the local geometric current density ($i_{1D-MEA}(z)$) associated with the 1D-MEA slice located at point z in the gas channel (equation S53).

$$i_{Cell,Avg} = \frac{1}{l_{MEA}} \int_{z=0}^{z=l_{MEA}} i_{1D-MEA}(z)dz \quad (S53)$$

We note that in the below equations, x' is a coordinate axis in the same direction as the x-axis in Figure S1, with its origin located at the start of a layer. The choice of this axis enables a more straightforward presentation of integral limits in the voltage loss calculation equations.

Kinetic voltage loss calculations:

We calculated the cathode kinetic voltage loss using equations S54 and S55.

$$\Delta V_{Kinetic,CCL}(z) = \frac{1}{i_{1D-MEA}(z)} \int_{x'=0}^{x'=t_{CCL}} (i_{ORR}(x',z)a_{Cat})\left(\varphi_1(x',z) - \varphi_2(x',z) - U_{ORR}(x',z)\right)dx' \quad (S54)$$

$$\Delta V_{Kinetic,CCL,Cell} = \frac{1}{i_{Cell,Avg}l_{MEA}} \int_{z=0}^{z=l_{MEA}} i_{1D-MEA}(z)\Delta V_{Kinetic,CCL}(z)dz \quad (S55)$$

In equation S54, $\Delta V_{Kinetic,CCL}(z)$ is the cathode kinetic voltage loss associated with the 1D-MEA slice located at point z in the gas channel, $i_{1D-MEA}(z)$ is the local geometric current density associated with the 1D-MEA slice located at point z in the gas channel, i_{ORR} is the ORR

electrocatalyst-specific current density (equation S30 for PEMFC and equation S33 for HEMFC), a_{Cat} is the specific interfacial area of the ORR electrocatalyst ($m^2_{ECSA}/m^3_{Electrode}$), φ_1 is the electronic potential, φ_2 is the ionic potential, U_{ORR} is the ORR equilibrium potential, and t_{CCL} is the thickness of the cathode electrocatalyst layer. In equation S55, $\Delta V_{Kinetic,CCL,Cell}$ is the single-cell cathode kinetic voltage loss, and the rest of the parameter definitions are the same as those in equations S53 and S54.

We calculated the anode kinetic voltage loss using equations S56 and S57.

$$\Delta V_{Kinetic,ACL}(z) = \frac{1}{i_{1D-MEA}(z)} \int_{x'=0}^{x'=t_{ACL}} (i_{HOR}(x',z)a_{Cat})\left(\varphi_1(x',z) - \varphi_2(x',z) - U_{HOR}(x',z)\right)dx' \quad (S56)$$

$$\Delta V_{Kinetic,ACL,Cell} = \frac{1}{i_{Cell,Avg}l_{MEA}} \int_{z=0}^{z=l_{MEA}} i_{1D-MEA}(z)\Delta V_{Kinetic,ACL}(z)dz \quad (S57)$$

In equation S56, $\Delta V_{Kinetic,ACL}(z)$ is the anode kinetic voltage loss associated with the 1D-MEA slice located at point z in the gas channel, $i_{1D-MEA}(z)$ is the local geometric current density associated with the 1D-MEA slice located at point z in the gas channel, i_{HOR} is the HOR electrocatalyst-specific current density (equation S36 for PEMFC and equation S39 for HEMFC), a_{Cat} is the specific interfacial area of the HOR electrocatalyst ($m^2_{ECSA}/m^3_{Electrode}$), φ_1 is the electronic potential, φ_2 is the ionic potential, U_{HOR} is the HOR equilibrium potential, and t_{ACL} is the thickness of the anode electrocatalyst layer. In equation S57, $\Delta V_{Kinetic,ACL,Cell}$ is the single-cell anode kinetic voltage loss, and the rest of the parameter definitions are the same as those in equations S53 and S56.

Ionic Ohmic voltage loss calculations:

We calculated the ionic Ohmic voltage loss using equations S58 to S63.

$$\Delta V_{Ion\ Ohmic,\ ACL}(z) = \frac{1}{i_{1D-MEA}(z)} \int_{x'=0}^{x'=t_{ACL}} \frac{i_2^2(x',z)}{\kappa^{Eff}(x',z)} dx' \quad (S58)$$

$$\Delta V_{Ion\ Ohmic,\ ACL,Cell} = \frac{1}{i_{Cell,Avg} l_{MEA}} \int_{z=0}^{z=l_{MEA}} i_{1D-MEA}(z) \Delta V_{Ion\ Ohmic,ACL}(z) dz \quad (S59)$$

$$\Delta V_{Ion\ Ohmic,CCL}(z) = \frac{1}{i_{1D-MEA}(z)} \int_{x'=0}^{x'=t_{CCL}} \frac{i_2^2(x',z)}{\kappa^{Eff}(x',z)} dx' \quad (S60)$$

$$\Delta V_{Ion\ Ohmic,CCL,Cell} = \frac{1}{i_{Cell,Avg} l_{MEA}} \int_{z=0}^{z=l_{MEA}} i_{1D-MEA}(z) \Delta V_{Ion\ Ohmic,\ CCL}(z) dz \quad (S61)$$

$$\Delta V_{Ion\ Ohmic,Mem}(z) = \frac{1}{i_{1D-MEA}(z)} \int_{x'=0}^{x'=t_{Mem}} \frac{i_2^2(x',z)}{\kappa^{Eff}(x',z)} dx' = i_{1D-MEA}(z) \int_{x'=0}^{x'=t_{Mem}} \frac{1}{\kappa^{Eff}(x',z)} dx' \quad (S62)$$

$$\Delta V_{Ion\ Ohmic,Mem,Cell} = \frac{1}{i_{Cell,Avg} l_{MEA}} \int_{z=0}^{z=l_{MEA}} i_{1D-MEA}(z) \Delta V_{Ion\ Ohmic,Mem}(z) dz \quad (S63)$$

In equations S58 to S63, $\Delta V_{Ion\ Ohmic,ACL}(z)$, $\Delta V_{Ion\ Ohmic,CCL}(z)$, $\Delta V_{Ion\ Ohmic,Mem}(z)$, $\Delta V_{Ion\ Ohmic,\ ACL,Cell}$, $\Delta V_{Ion\ Ohmic,CCL,Cell}$, $\Delta V_{Ion\ Ohmic,Mem,Cell}$, i_2, κ^{Eff}, t_{ACL}, t_{CCL} and t_{Mem} are the anode/cathode/membrane ionic Ohmic loss associated with the 1D-MEA slice located at point z in the gas channel, the single-cell anode/cathode/membrane ionic Ohmic voltage loss, ionic current density, effective ionic conductivity, and anode electrocatalyst layer/cathode electrocatalyst layer/membrane thickness. The rest of the parameter definitions are the same as those in equation S53.

Electronic Ohmic voltage loss calculations:

We calculated the electronic Ohmic voltage loss of the electrocatalyst layers using equations S64 to S67.

$$\Delta V_{Ele\ Ohmic,ACL}(z) = \frac{1}{i_{1D-MEA}(z)} \int_{x'=0}^{x'=t_{ACL}} \frac{i_1^2(x',z)}{\sigma^{Eff}} dx' \quad (S64)$$

$$\Delta V_{Ele\ Ohmic,ACL,Cell} = \frac{1}{i_{Cell,Avg} l_{MEA}} \int_{z=0}^{z=l_{MEA}} i_{1D-MEA}(z) \Delta V_{Ele\ Ohmic,ACL}(z) dz \quad (S65)$$

$$\Delta V_{Ele\ Ohmic,CCL}(z) = \frac{1}{i_{1D-MEA}(z)} \int_{x'=0}^{x'=t_{CCL}} \frac{i_1^2(x',z)}{\sigma^{Eff}} dx' \quad (S66)$$

$$\Delta V_{Ele\ Ohmic,CCL,Cell} = \frac{1}{i_{Cell,Avg} l_{MEA}} \int_{z=0}^{z=l_{MEA}} i_{1D-MEA}(z) \Delta V_{Ele\ Ohmic,CCL}(z) dz \quad (S67)$$

In equations S64 to S67, $\Delta V_{Ele\ Ohmic,ACL}(z)$, $\Delta V_{Ele\ Ohmic,CCL}(z)$, $\Delta V_{Ele\ Ohmic,ACL,Cell}$, $\Delta V_{Ele\ Ohmic,CCL,Cell}$, i_1, σ^{Eff}, t_{ACL}, and t_{CCL} are the anode/cathode electronic Ohmic voltage loss associated with the 1D-MEA slice located at point z in the gas channel, the single-cell anode/cathode electronic Ohmic voltage loss, electronic current density, effective electronic conductivity, and anode electrocatalyst layer/cathode electrocatalyst layer thickness. The rest of the parameter definitions are the same as those in equation S53.

We calculated the electronic Ohmic voltage loss caused by contact resistance using equations S68 and S69. We note that using the idea of equivalent resistances, we captured the effect of contact resistance in the GDM electronic conductivity (equation S27).

$$\Delta V_{Ele\ Ohmic,Contact}(z) = \frac{2}{i_{1D-MEA}(z)} \int_{x'=0}^{x'=t_{GDM}} \frac{i_1^2(x',z)}{\sigma_{GDM}} dx' = \frac{2 i_{1D-MEA}(z) t_{GDM}}{\sigma_{GDM}} \quad (S68)$$

$$\Delta V_{Ele\ Ohmic,\ Contact,Cell} = \frac{1}{i_{Cell,Avg} l_{MEA}} \int_{z=0}^{z=l_{MEA}} i_{1D-MEA}(z) \Delta V_{Ele\ Ohmic,Contact}(z) dz \quad (S69)$$

In equations S68 and S69, $\Delta V_{Ele\ Ohmic,Contact}(z)$, $\Delta V_{Ele\ Ohmic,\ Contact,Cell}$, i_l, σ_{GDM}, t_{GDM}, and t_{GDM} are the electronic Ohmic voltage loss caused by contact resistance associated with the 1D-MEA slice located at point z in the gas channel, the single-cell electronic Ohmic voltage loss caused by contact resistance, electronic current density, electronic conductivity of GDM, and GDM thickness. The rest of the parameter definitions are the same as those in equation S53. Finally, we combined all the single-cell electronic Ohmic voltage loss terms into one term named total electronic Ohmic voltage loss, the values of which we reported in the paper (equation S70).

$$\Delta V_{Ele\ Ohmic,Total,Cell} = \Delta V_{Ele\ Ohmic,ACL,Cell} + \Delta V_{Ele\ Ohmic,CCL,Cell} + \Delta V_{Ele\ Ohmic,Contact,Cell} \quad (S70)$$

Concentration voltage loss calculations:

We calculated the concentration voltage losses using equations S71 to S74.

$$\Delta V_{Concentration,CCL}(z) = \frac{1}{i_{1D-MEA}(z)} \int_{x'=0}^{x'=t_{CCL}} (i_{ORR}(x',z) a_{Cat})(U_{ORR}(x',z) - \overset{\circ}{E}_{ORR}) dx' \quad (S71)$$

$$\Delta V_{Concentration,CCL,Cell} = \frac{1}{i_{Cell,Avg} l_{MEA}} \int_{y=0}^{y=l_{MEA}} i_{1D-MEA}(z) \Delta V_{Concentration,CCL}(z) dz \quad (S72)$$

$$\Delta V_{Concentration,ACL}(z) = \frac{1}{i_{1D-MEA}(z)} \int_{x'=0}^{x'=t_{ACL}} (i_{HOR}(x',z) a_{Cat})(U_{HOR}(x',z) - \overset{\circ}{E}_{HOR}) dx' \quad (S73)$$

$$\Delta V_{Concentration,\ ACL,Cell} = \frac{1}{i_{Cell,Avg} l_{MEA}} \int_{z=0}^{z=l_{MEA}} i_{1D-MEA}(z) \Delta V_{Concentration,ACL}(z) dz \quad (S74)$$

In equations S71 to S74, $\Delta V_{Concentration,CCL}(z)$, $\Delta V_{Concentration,ACL}(z)$, $\Delta V_{Concentration,CCL,Cell}$, $\Delta V_{Concentration,\,ACL,Cell}$, E°_{ORR}, E°_{HOR}, t_{CCL}, and t_{ACL} are the cathode/anode concentration voltage loss associated with the 1D-MEA slice located at point z in the gas channel, the single-cell cathode/anode concentration voltage loss, the standard ORR equilibrium potential, the standard HOR equilibrium potential, and anode electrocatalyst layer/cathode electrocatalyst layer thickness. The rest of the parameter definitions are the same as those in equations S54 and S56. Finally, we combined all the single-cell concentration voltage loss terms and N_2 buildup voltage degradation ($\Delta V_{N_2\,buildup} = 1\ mV$) into one term named total concentration voltage loss, the values of which we reported in the paper (equation S75).

$$\Delta V_{Concentration,Total,Cell} = \Delta V_{Concentration,CCL,Cell} + \Delta V_{Concentration,\,ACL,Cell} + \Delta V_{N_2\,buildup} \quad (S75)$$

FC stack cost model details

The SA comprehensive report provides a PEMFC stack cost model that correlates the stack's cost ($C_{Stack,PEMFC}$; \$) to its active area, anode/cathode electrocatalyst loadings, and anode/cathode electrocatalyst material cost (equation S76).[2]

$$C_{Stack,PEMFC} = 1.97 \times 10^{-4} \times ((0.16485 \times A_{Active\ Stack} + 588.83) \times (L_{Anode} \times E$$
$$+ (0.00900 \times A_{Active\ Stack}) + 295.05 \quad (S76)$$

In equation S76, $A_{Active\ Stack}$, L_{Anode}, $L_{Cathode}$, $Electrocatalyst\ Cost_{Anode}$, and $Electrocatalyst\ Cost_{Cathode}$ are the total active area of the stack (cm^2), anode/cathode electrocatalyst loading (mg/cm^2), and anode/cathode electrocatalyst material cost (\$/tr.oz).[2] We included the material cost of the electrocatalysts considered in our paper in the caption of Figure S2. We adopted the PEMFC stack cost model and updated it to reflect the cost of the HEMFC

stack by applying some corrections to the cost model. We explain the details of these correction terms below.

The membrane electrode assembly (MEA) related assumptions

According to the SA comprehensive report, the gaskets and GDLs are applied to the electrocatalyst-coated membrane through a roll-to-roll (R2R) process, and a ~1/8 inch (~ 0.003175 m) overlap of the gasket over membrane exists on each side (Figure S5).[2] We assumed that the FC stacks in our study have the same overlap value. Subsequently, we defined a term named $R_{WA,}$ which is the ratio of the wasted to the active surface area of a single cell in the stack, which is equal to the ratio of the wasted to the active area of the stack (equation S77).

$$R_{WA} = \frac{(l_{MEA} + 2\delta_{Overlap})(w_{MEA} + 2\delta_{Overlap}) - l_{MEA}w_{MEA}}{l_{MEA}w_{MEA}} \quad (S77)$$

In equation S77, l_{MEA}, w_{MEA}, and $\delta_{Overlap}$ are the length/width of the MEA and the overlap length ($\delta_{Overlap} = \frac{1}{8}inch$). The term $(1 + R_{WA}) \times A_{Active\ Stack}$ defines the total area of the stack (i.e., the sum of active and wasted areas), and we used this term in our cost corrections as detailed below. We note that for the 2018 LDV PEMFC system in the SA comprehensive report, the active area of a single cell is 197 cm^2.[2] We reasonably assumed that this single cell has the same ratio of (l_{MEA}/w_{MEA}) as that of Toyota Mirai ($l_{MEA,Toyota\ Mirai}$=13.36 cm and $w_{MEA,Toyota\ Mirai}$=20 cm).[2] Consequently, the l_{MEA} and w_{MEA} of the 2018 LDV PEMFC system would be 11.47 cm and 17.17 cm, respectively. Using equation S77, the R_{WA} for the 2018 LDV PEMFC system, from now called $R_{WA,2018\ PEMFC}$, will be 0.0943.

Changing the bipolar plate (BPP) from 316L stainless steel coated with TreadStone DOTS-R coating to aluminum coated with TreadStone TiO_X-containing coating

The BPPs of the 2018 LDV PEMFC system in the SA comprehensive report and the BPPs of the LDV PEMFC system with the stack cost function presented in equation S76 are made of 316L stainless steel (SS316L), and the BPPs are coated with a PM-containing coating (TreadStone DOTS-R).[2] Consequently, first, we estimated the cost of BPPs ($C_{BPP,PEMFC}$) for a LDV PEMFC system with a total stack area of ($A_{Active\ Stack} \times (1 + R_{WA})$). Next, we estimated the cost of BPPs ($C_{BPP,HEMFC}$) made from aluminum and coated with a PM-free coating (TreadStone TiO_X-containing coating) for a HEMFC LDV system with a total stack area of ($A_{Active\ Stack} \times (1 + R_{WA})$). Finally, we added a correction term ($C_{BPP,HEMFC}$-$C_{BPP,PEMFC}$) to equation S76, which will effectively change the BPP from 316L stainless steel coated with TreadStone DOTS-R coating to aluminum coated with TreadStone TiO_X-containing coating in the stack cost function.

Table S2 provides the cost breakdown of BPPs of the 2018 LDV system as presented in the SA comprehensive report.[2] The materials cost of BPPs referees to the cost of SS316L sheets used in the BPPs. The SA comprehensive report specifies the material cost of SS316L and SS316L sheets as 3.93 $/kg and 13.19 $/kg. Consequently, one can calculate the cost of SS316L sheet manufacturing as 9.26 $/kg and the mass of the SS316L sheet used in the 2018 LDV PEMFC system as 15.466 kg.[2] The manufacturing cost of BPPs includes the capital cost of the progressive stamping machine (excluding dies cost), the capital cost of the BPP quality control system, the maintenance cost of the progressive stamping machine, and the utilities cost.[2] The BPP tooling cost includes the dies capital and maintenance cost.[2] The BPP coating cost consists of the coating materials and manufacturing cost (physical vapor deposition (PVD), chemical etching, and heat

treatment steps cost).[2] Conceptually, as shown in equation S78, the total mass of BPP material present in a FC stack is proportional to the total stack area ($A_{Active\ Stack} \times (1 + R_{WA})$), the effective thickness of the BPP ($t_{BPP,Eff}$), and the density of the BPP substrate ($\rho_{BPP\ material}$).

$$Total\ mass\ of\ BPP\ material \propto A_{Active\ Stack} \times (1 + R_{WA}) \times t_{BPP,Eff} \times \rho_{BPP\ material} \quad (S78)$$

By using equation S78 and after accounting for the area difference between a PEMFC stack with a total stack area of ($A_{Active\ Stack} \times (1 + R_{WA})$) and the 2018 LDV PEMFC system with a total stack area of ($A_{Active\ Stack,2018\ PEMFC} \times (1 + R_{WA,2018\ PEMFC})$), we can calculate $C_{BPP,PEMFC}$ using equation S78, keeping in mind that $t_{BPP,Eff}$ and $\rho_{BPP\ material}$ are the same for these two systems ($A_{Active\ Stack,2018\ PEMFC} = 7.486\ m^2$).[2]

$$C_{BPP,PEMFC} = \frac{A_{Active\ Stack} \times (1 + R_{WA})}{A_{Active\ Stack,2018\ PEMFC} \times (1 + R_{WA,2018\ PEMFC})} \times 388 \quad (S79)$$

The SA comprehensive report suggests hydroforming as a potential lower-cost replacement for progressive stamping, which is worth investigating.[2] However, this approach is not well-established for producing BPPs in the FC industry.[2] Consistent FC industry feedback shows that progressive stamping is the most common approach currently implemented successfully for making BPPs and is inferred to be employed by GM, Dana Reinz, and Mercedes Benz.[2] Consequently, we cautiously chose to keep progressive stamping as our method for producing BPPs for HEMFC stacks. We note that aluminum is lighter and softer than stainless steel (SS).[39] Consequently, we enforced the requirement that aluminum-based BPPs have equivalent mechanical flexural rigidity (i.e., resistance offered by a material while undergoing bending forces[39]) as SS-based BPPs. We presented the definition of flexural rigidity for a slab of material in Figure S6.[39] Enforcement of the requirement mentioned above will result in a correlation

between the effective thickness of aluminum-based BPP and SS-based BPP (equation S80). In the calculation described in equation S80, we assumed reasonable values of 193 GPa and 69 GPa for Young's modulus of SS316L and aluminum.[39]

$$E_{Young\ Al} \times \left(\frac{w_{BPP} t_{BPP,\,Eff}^{\ 3}}{12}\right)_{Al\_based\ BPP} = E_{Young\ SS316L} \times \left(\frac{w_{BPP} t_{BPP,\,Eff}^{\ 3}}{12}\right)_{SS316L\_based\ BPP} \Rightarrow \left(\frac{t_{BPP,\,Eff,\,Al\_based\ BPP}}{t_{BPP,\,Eff,\,SS316L\_based\ BPP}}\right) = \left(\frac{E_{Young\ SS316L}}{E_{Young\ Al}}\right)^{\frac{1}{3}} = 1.409 \quad (S80)$$

Using equations S78 and S80, and after accounting for the area difference between a HEMFC stack with a total stack area of $\left(A_{Active\ Stack} \times \left(1 + R_{WA}\right)\right)$ and the 2018 LDV PEMFC system with a total stack area of $\left(A_{Active\ Stack,2018\ PEMFC} \times \left(1 + R_{WA,2018\ PEMFC}\right)\right)$, we can calculate the total mass of aluminum sheets used in the HEMFC stack using equation S81. In the calculation described in equation S81, we assumed reasonable values of 8000 kg/m^3 and 2700 kg/m^3 for the density of SS316L and aluminum.[39]

$$\frac{Total\ mass\ of\ Al\ based\ BPP\ (HEMFC\ system)}{Total\ mass\ of\ SS316L\ based\ BPP\ (2018\ PEMFC) = 15.466\ kg} = \frac{A_{Active\ Stack} \times \left(1 + R_{WA}\right)}{A_{Active\ Stack,2018\ PEMFC} \times \left(1 + R_{WA,2018\ PEMFC}\right)} \times \left(\frac{E_{Young\ SS316L}}{E_{Young\ Al}}\right)^{\frac{1}{3}} \times \left(\frac{\rho_{Al}}{\rho_{SS316L}}\right) = 0.4755 \times \left(\frac{A_{Active\ Stack} \times \left(1 + R_{WA}\right)}{A_{Active\ Stack,2018\ PEMFC} \times \left(1 + R_{WA,2018\ PEMFC}\right)}\right) \quad (S81)$$

The cost of aluminum is 2.54 $/kg, and we assumed that the cost of aluminum sheet manufacturing is the same as that of SS316L sheet manufacturing (9.26 $/kg). Consequently, the material cost of the aluminum sheet would be 11.80 $/kg. By using the material cost of the aluminum sheet and equation S81, one can calculate the BPP materials cost ($C_{BPP,HEMFC,Materials}$) for a HEMFC stack with a total stack area of $\left(A_{Active\ Stack} \times \left(1 + R_{WA}\right)\right)$

through equation S82.

$$C_{BPP,HEMFC,Materials} = \frac{A_{Active\ Stack} \times (1 + R_{WA})}{A_{Active\ Stack,2018\ PEMFC} \times (1 + R_{WA,2018\ PEMFC})} \times 86.80 \quad (S82)$$

We reasonably assumed that the BPP manufacturing cost and BPP tooling cost of the 2018 LDV PEMFC system normalized by its total stack area are the same as that of a HEMFC stack. This assumption will allow us to calculate the BPP manufacturing cost and BPP tooling cost of a HEMFC stack with a total stack area of ($A_{Active\ Stack} \times (1 + R_{WA})$) through equation S83.

$$C_{BPP,HEMFC,Manufacturing\ \&\ Tooling} = \frac{A_{Active\ Stack} \times (1 + R_{WA})}{A_{Active\ Stack,2018\ PEMFC} \times (1 + R_{WA,2018\ PEMFC})} \times (64 + 52) \quad (S83)$$

The SA comprehensive report provides a cost estimate for a PM-free coating (TreadStone TiO_X-containing coating) for the 2020 LDV PEMFC system at 500000 systems per year (46 \$/Stack).[2] We note that for the 2020 LDV PEMFC system in the SA comprehensive report, the active area of a single cell is 185 cm^2, and the total active stack area is 7.03 m^2 ($A_{Active\ Stack,2020\ PEMFC} = 7.03\ m^2$).[2] We reasonably assumed that this single cell has the same ratio of (l_{MEA}/w_{MEA}) as that of Toyota Mirai ($l_{MEA,Toyota\ Mirai}$=13.36 cm and $w_{MEA,Toyota\ Mirai}$=20 cm). Consequently, the l_{MEA} and w_{MEA} of the 2020 LDV PEMFC system would be 11.12 cm and 16.64 cm, respectively. Using equation S77, the R_{WA} for the 2020 LDV PEMFC system, from now called $R_{WA,2020\ PEMFC}$, will be 0.0975. We reasonably assumed that the BPP coating cost of the 2020 LDV PEMFC system normalized by its total stack area is the same as that of a HEMFC stack. This assumption will allow us to calculate the BPP coating cost of a HEMFC stack with a total stack area of ($A_{Active\ Stack} \times (1 + R_{WA})$) through equation S84.

$$C_{BPP,HEMFC,Coating} = \frac{A_{Active\ Stack} \times (1 + R_{WA})}{A_{Active\ Stack,2020\ PEMFC} \times (1 + R_{WA,2020\ PEMFC})} \times 46 \quad (S84)$$

Subsequently, the cost of BPPs of a HEMFC stack ($C_{BPP,HEMFC}$) with a total stack area of ($A_{Active\ Stack} \times (1 + R_{WA})$) can be calculated by combining equations S82 to S84.

$$C_{BPP,HEMFC} = C_{BPP,HEMFC,Materials} + C_{BPP,HEMFC,Manufacturing\ \&\ Tooling} + C_{BPP,HEMFC,Coating} \quad (S85)$$

Replacing the PFSA PEI in the membrane and electrodes with a cheaper HEI that has the same conductivity and H_2O permeability as 700 EW PFSA

The PEMFC stack cost function shown in equation S76 corresponds to a PEMFC stack with a 14 μm membrane ($t_{Membrane\ PEMFC} = 14\ \mu m$).[2] The membrane consists of PFSA PEI (850EW) supported on ePTFE, and the PEI implemented in the electrodes is PFSA (950 EW) ionomer.[2] Consequently, first, we estimated the cost of the PEI in the membrane ($C_{PEI\ of\ membrane,PEMFC}$) and the cost of PEI in the electrodes ($C_{PEI\ in\ electrodes,PEMFC}$) for a LDV PEMFC system with a total stack area of ($A_{Active\ Stack} \times (1 + R_{WA})$). Next, we estimated the cost of the HEI in the membrane ($C_{HEI\ of\ membrane,HEMFC}$) and the cost of HEI in the electrodes ($C_{HEI\ in\ electrodes,HEMFC}$) for a LDV HEMFC system with a total stack area of ($A_{Active\ Stack} \times (1 + R_{WA})$). The HEI has the same conductivity and H_2O permeability as PFSA (700 EW) PEI while being cheaper. Finally, we added a correction term ($C_{HEI\ of\ membrane,HEMFC} + C_{HEI\ in\ electrodes,HEMFC} - C_{PEI\ of\ membrane,PEMFC} - C_{PEI\ in\ electrodes,PEMFC}$) to equation S76. This correction term will effectively replace the PFSA PEIs in the membrane and electrodes with a cheaper HEI that has the same conductivity and H_2O permeability as PFSA (700 EW) PEI. As mentioned before, the thickness of the membrane in our HEMFC stack is 10 μm ($t_{Membrane\ HEMFC} = 10\ \mu m$). According to the SA comprehensive report, the cost of ePTFE production firmly controls the price of ePTFE. Consequently, it is reasonable to assume that

ePTFE cost is primarily independent of its thickness.[2] Consequently, we do not need a correction term to account for the difference in the thickness of ePTFE support between the PEMFC stack and HEMFC stack.

We used a cost factor approach to estimate the cost of PEIs with different EWs adapted directly from the SA comprehensive report.[2] The price of PEIs is based upon the high-volume manufacturing of perfluorosulfonic acid-based PEIs from the raw material of hexafluoropropylene oxide (HFPO). HFPO makes up the majority of the raw material cost of PEIs. The usage of HFPO is inversely proportional to the EW value. Thus, an increase in cost for lower EW PEIs can be adequately approximated via the equation S86 below (with the reasonable assumption that raw materials account for half of the total PEI price).[2]

$$Cost_{PEI,Mass-based}(EW = X) = Cost_{PEI,Mass-based}(EW = 1100) \times 0.5 \times \left(1 + \left(\frac{1100}{X}\right)\right) \quad (S86)$$

In equation S86, $Cost_{PEI,Mass-based}(EW = X)$ and $Cost_{PEI,Mass-based}(EW = 1100)$ are the mass-based cost of a (X EW) PEI ($/kg) and the mass-based cost of a (1100 EW) PEI (99 $/kg).[2] The mass-based cost presented in equation S86 can be converted to volume-based cost ($/m^3) using the density of PFSA-based PEIs ($\rho_{PEI} = 2000\,\frac{kg}{m^3}$) (equation S87).

$$Cost_{PEI,Volume-based}(EW = X) = Cost_{PEI,Mass-based}(EW = X)\,\rho_{PEI} \quad (S87)$$

As mentioned before, we reasonably assumed that the HEI in our technoeconomic analysis has the same density as PAP-TP-85 ($\rho_{HEI} = 1200\,\frac{kg}{m^3}$). This assumption, combined with the assumption that the HEI in our technoeconomic analysis has the exact cost per mass as a (700 EW) PEI, will result in a HEI with a lower cost per volume than a (700 EW) PEI (equation S88).

$$Cost_{HEI,Volume-based} = Cost_{PEI,Mass-based}(EW = 700)\ \rho_{HEI} \quad (S88)$$

According to the SA comprehensive report, material loss in the membrane manufacturing process stems from four losses: 1) fluid loss within machinery or fluid lines, 2) membrane edge losses removed after production, 3) machinery start-up and shut-down losses, and 4) unplanned wastage due to membrane coating defect/contamination.[2] The SA comprehensive report specifies the ePTFE yield ($Yield_{ePTFE}$) and the ionomer yield ($Yield_{Ionomer}$) in the membrane as 0.95 and 0.94.[2] According to the SA comprehensive report, the electrocatalyst ink is applied to the membrane through slot die coating. Due to the proprietary nature of slot die coating machines, a detailed breakdown of their operational parameters/performance is not available publicly.[2] Consequently, we reasonably assumed the ionomer yield for the ionomer incorporated into the electrodes is the same as the ionomer yield in the membrane. Now we can calculate the cost of the PEI in the membrane ($C_{\text{PEI of membrane,PEMFC}}$) and the cost of PEI in the electrodes ($C_{\text{PEI in electrodes,PEMFC}}$) for a LDV PEMFC system with a total stack area of ($A_{Active\ Stack} \times (1 + R_{WA})$) from equations S89 and S90.

$$C_{PEI\ of\ membrane,PEMFC} = \frac{\varepsilon_{ePTFE}(A_{Active\ Stack} \times (1 + R_{WA}))}{Yield_{Ionomer}} \times (t_{Membrane\ PEMFC} \times Cost_{PEI,Volume-based}(EW = 850)) \quad (S89)$$

$$C_{PEI\ in\ electrodes,PEMFC} = \frac{\varepsilon_{Ionomer}(A_{Active\ Stack} \times (1 + R_{WA}))}{Yield_{Ionomer}} \times (t_{Anode\ PEMFC} + t_{Cathode\ PEMFC}) \times Cost_{PEI,Volume-based}(EW = 950)) \quad (S90)$$

In equation S89 and S90, ε_{ePTFE} and $\varepsilon_{Ionomer}$ are ionomer volume fractions in the membrane (0.95) and electrocatalyst layers (0.15). Similarly, we can calculate the cost of the HEI in the membrane ($C_{\text{HEI of membrane,HEMFC}}$) and the cost of HEI in the electrodes ($C_{\text{HEI in electrodes,HEMFC}}$) for a LDV HEMFC system with a total stack area of ($A_{Active\ Stack} \times (1 + R_{WA})$) from equations S91

and S92.

$$C_{HEI\ of\ membrane,HEMFC} = \frac{\varepsilon_{ePTFE}\left(A_{Active\ Stack} \times (1 + R_{WA})\right)}{Yield_{Ionomer}} \times \left(t_{Membrane\ HEMFC} \times Cost_{HEI,Volume-based}\right) \quad (S91)$$

$$C_{HEI\ in\ electrodes,HEMFC} = \frac{\varepsilon_{Ionomer}\left(A_{Active\ Stack} \times (1 + R_{WA})\right)}{Yield_{Ionomer}} \times \left(t_{Anode\ HEMFC} + t_{Cathode\ HEMFC}\right) \times Cost_{HEI,Volume-based} \quad (S92)$$

The HEMFC stack cost function

Following the above discussions, we presented the HEMFC stack cost function in equation S93. We presented the definition of $C_{Stack,PEMFC}$, $C_{BPP,PEMFC}$, $C_{BPP,HEMFC}$, $C_{PEI\ of\ membrane,PEMFC}$, $C_{PEI\ in\ electrodes,PEMFC}$, $C_{HEI\ of\ membrane,HEMFC}$, and $C_{HEI\ in\ electrodes,HEMFC}$ terms in equations S76, S79, S85, S89, S90, S91, and S92.

$$C_{Stack,HEMFC} = C_{Stack,PEMFC} + \left(C_{BPP,HEMFC} - C_{BPP,PEMFC}\right) + \left(C_{HEI\ of\ membrane,HE} \quad (S93)$$

FC stack component cost breakdown

We performed a component cost breakdown using the FC stack cost models detailed above and the cost information provided in the SA comprehensive report. We broke down the stack cost into component costs: anode/cathode electrocatalyst cost, ePTFE membrane substrate cost, total ionomer within electrodes and membrane cost, BPP cost, GDL coated with MPL cost, subgasket and its sealing cost, and balance of stack (BOS) cost.

Anode/cathode electrocatalyst cost analysis

Using the FC stack cost function provided in the SA comprehensive report (equation S76), we can calculate the anode/cathode electrocatalyst cost by equations S94 and S95 for either a PEMFC stack or a HEMFC stack. The definition of the parameters in equations S94 and S95 are the same

as those in equation S76.

$$C_{Anode\ electrocatalyst} = 1.97 \times 10^{-4} \times ((0.16485 \times A_{Active\ Stack} + 588.83) \times (L_{Anode} \times \quad (S94)$$

$$C_{Cathode\ electrocatalyst} = 1.97 \times 10^{-4} \times ((0.16485 \times A_{Active\ Stack} + 588.83) \times (L_{Cathode} \times \quad (S95)$$

ePTFE membrane substrate cost analysis

The SA comprehensive report specifies the area-based cost of the ePTFE membrane substrate and the ePTFE yield ($Yield_{ePTFE}$) in the membrane as 6.18 ($/m^2) as 0.95.[2] Consequently, we can calculate the ePTFE membrane substrate cost (C_{ePTFE}) of either a PEMFC stack or a HEMFC stack with a total stack area of ($A_{Active\ Stack} \times (1 + R_{WA})$) by equation S96.

$$C_{ePTFE} = \frac{A_{Active\ Stack} \times (1 + R_{WA})}{Yield_{ePTFE}} \times 6.18 \quad (S96)$$

Total ionomer within electrodes and membrane cost analysis

We note that the ionomer cost within electrodes and the ionomer cost in the membrane are minor contributors to the overall cost of either a PEMFC stack or a HEMFC stack. So, we decided to combine these into one cost function. For a PEMFC, we can calculate the total cost of the PEI in the stack ($C_{PEI,PEMFC}$) by equation S97.

$$C_{PEI,PEMFC} = C_{PEI\ of\ membrane,PEMFC} + C_{PEI\ in\ electrodes,PEMFC} \quad (S97)$$

For a HEMFC, we can calculate the total cost of the HEI in the stack ($C_{HEI,HEMFC}$) by equation S98.

$$C_{HEI,HEMFC} = C_{HEI\ of\ membrane,HEMFC} + C_{HEI\ in\ electrodes,HEMFC} \quad (S98)$$

BPP cost analysis

We presented the cost of BPP for a PEMFC stack and a HEMFC stack in equations S79 and S85.

GDL coated with MPL cost analysis

The SA comprehensive report specifies the area-based cost of the GDL coated with MPL as 5.64 \$/m^2.[2] Consequently, we can calculate the cost of GDL coated with MPL (C_{GDL}) of either a PEMFC stack or a HEMFC stack with a total active area of ($A_{Active\ Stack}$) by equation S99. We included factor 2 in equation S99 to account for the presence of two GDLs coated with MPL in the stack, one on the anode side and the other on the cathode side.

$$C_{GDL} = 2A_{Active\ Stack} \times 5.64 \quad (S99)$$

Subgasket and its sealing cost analysis

The SA comprehensive report specifies the cost of the subgasket and its sealing for the 2018 LDV PEMFC system as 85 \$.[2] We reasonably assumed that the subgasket and its sealing cost of the 2018 LDV PEMFC system normalized by its total stack area is the same as that of a PEMFC stack or a HEMFC stack with a total stack area of ($A_{Active\ Stack} \times (1 + R_{WA})$). This assumption will allow us to calculate the subgasket and its sealing cost of a PEMFC stack or a HEMFC stack with a total stack area of ($A_{Active\ Stack} \times (1 + R_{WA})$) through equation S100.

$$C_{Subgasket\ and\ its\ sealing} = \frac{A_{Active\ Stack} \times (1 + R_{WA})}{A_{Active\ Stack,2018\ PEMFC} \times (1 + R_{WA,2018\ PEMFC})} \times 85 \quad (S100)$$

BOS cost analysis

We calculated the BOS cost of a PEMFC or a HEMFC by subtracting the cost of anode/cathode electrocatalyst, ePTFE membrane substrate, total ionomer within electrodes and membrane, BPP, GDL coated with MPL, and subgasket and its sealing from the stack cost function.

EDCS performance model details

Definition of parameters for EDCS and BOP calculations

We defined a few parameters for simplicity and a better conceptual understanding of our EDCS and BOP calculations. First, using equation S101, we defined a parameter named BOP current (I_{BOP}; A).

$$I_{BOP} = n_{Cell} I_{Cell} \ (S101)$$

In equation S101, n_{Cell} is the number of single cells in the FC stack and I_{Cell} is the FC stack current, which is the same as the current of a single cell in the stack. Here, we emphasize the fact that, despite having the dimension of current, I_{BOP} does not represent any actual current in the FC system, as the FC stack current equals to I_{Cell}. Following the definition of I_{BOP}, we can calculate the molar flow rate of O_2 entering the stack ($n_{O_2}^{Stack-Inlet}$; mol/s), the molar flow rate of O_2 exiting the stack ($n_{O_2}^{Stack-Outlet}$; mol/s), and the molar flow rate of H_2 entering the stack ($n_{H_2}^{Stack-Inlet}$; mol/s) by equations S102 to S104.

$$n_{O_2}^{Stack-Inlet} = n_{Cell}\left(\frac{S_{Cathode}}{4F} I_{Cell}\right) = \frac{S_{Cathode} I_{BOP}}{4F};\ S_{Cathode} = 1.5 \ \ (S102)$$

$$n_{O_2}^{Stack-Outlet} = n_{Cell}\left(\frac{(S_{Cathode} - 1)}{4F} I_{Cell}\right) = \frac{(S_{Cathode} - 1) I_{BOP}}{4F};\ S_{Cathode} = 1.5 \ \ (S103)$$

$$n_{H_2-Inlet}^{Stack} = n_{Cell}\left(\frac{S_{Anode}}{2F} I_{Cell}\right) = \frac{S_{Anode} I_{BOP}}{2F};\ S_{Anode} = 1.5 \quad (S104)$$

As we mentioned in the paper, the EDCS unit is a small HEMFC unit placed upstream of the HEMFC stack on the cathode side, which scrubs atmospheric air containing 420 ppm CO_2 to 4 ppm CO_2 concentration. Being a HEMFC, the EDCS unit consumes the O_2 in the atmospheric air and H_2 in the H_2 purge stream, producing H_2O while operating. We reasonably assumed that the H_2 purge in the FC stack to be 1% of H_2 fed to the FC stack, or equivalently to be 1.5% of stack H_2 consumption ($0.01 \times \left(\frac{S_{Anode} I_{BOP}}{2F}\right) = 0.015 \times \left(\frac{I_{BOP}}{2F}\right)$). Based on our in-lab measurements, we assigned a value of 0.8 as a reasonable estimate for H_2 utilization in EDCS units. Consequently, we can calculate the molar flow rate of H_2 consumed in the EDCS unit ($n_{H_2-Consumed}^{EDCS}$; mol/s) using equation S105.

$$n_{H_2-Consumed}^{EDCS} = 0.8 \times 0.015 \times \left(\frac{I_{BOP}}{2F}\right) = 0.012 \times \left(\frac{I_{BOP}}{2F}\right) \quad (S105)$$

Subsequently, using equation S106, we defined a parameter named f_{O_2}, which is the ratio of the molar flow rate of O_2 consumed in the EDCS unit ($n_{O_2-Consumed}^{EDCS}$; mol/s) to the molar flow rate of O_2 entering the stack ($n_{O_2-Inlet}^{Stack}$; mol/s).

$$f_{O_2} = \frac{n_{O_2-Consumed}^{EDCS}}{n_{O_2-Inlet}^{Stack}} = \frac{\frac{n_{H_2-Consumed}^{EDCS}}{2}}{n_{O_2-Inlet}^{Stack}} = \frac{0.012 \times \left(\frac{I_{BOP}}{4F}\right)}{\left(\frac{1.5 \times I_{BOP}}{4F}\right)} = 0.008 \quad (S106)$$

First, following the definition of f_{O_2}, we can calculate the molar flow rate of O_2 ($n_{O_2-Inlet}^{EDCS}$; mol/s) in the air loop going through the compressor, air-precooler, and dry side of the membrane

humidifier before entering the EDCS by equations S107.

$$n_{O_2-Inlet}^{EDCS} = \frac{(1+f_{O_2})S_{Cathode}I_{BOP}}{4F};\ S_{Cathode} = 1.5 \quad (S107)$$

Next, we can reasonably assume the molar flow rate of N_2 ($n_{N_2}^{Air\ loop}$; mol/s) in the air loop to be constant, and we can calculate it using equation S108.

$$n_{N_2}^{Air\ loop} = \frac{1 - x_{O_2}^{Dry\ air}}{x_{O_2}^{Dry\ air}} n_{O_2-Inlet}^{EDCS} = constant\ and\ x_{O_2}^{Dry\ air} = 0.21 \quad (S108)$$

Finally, we can calculate the molar flow rate of gaseous H_2O ($n_{H_2O}^{Air\ loop}$; mol/s) at any point in the air loop from the molar flow rate of O_2 at that point ($n_{O_2}^{Air\ loop}$; mol/s), molar flow rate of N_2 at that point ($n_{N_2}^{Air\ loop}$; mol/s), and H_2O mole fraction ($x_{H_2O}^{Air\ loop}$) at that point using equation S109.

$$n_{H_2O}^{Air\ loop} = \left(\frac{x_{H_2O}^{Air\ loop}}{1 - x_{H_2O}^{Air\ loop}}\right)\left(n_{O_2}^{Air\ loop} + n_{N_2}^{Air\ loop}\right) \quad (S109)$$

We want to finish this section by mentioning three crucial points. First, the equations mentioned in this section provide the foundation to calculate the molar flow rates in all of the air loop components outside the FC stack, and a close inspection of these equations shows that the total molar flow rates in these components are linearly proportional to (I_{BOP}), a fact that we will use in the following sections. Second, we can calculate the partial pressure of O_2 entering the stack ($P_{O_2-Inlet}^{Stack}$) from the stack inlet pressure (P_{Inlet}^{Stack}), O_2 mole fraction in dry air ($x_{O_2}^{Dry\ air} = 0.21$), H_2O mole fraction at stack inlet ($x_{H_2O}^{Stack\ inlet}$) and f_{O_2} using equation S110.

$$P_{O_2-Inlet}^{Stack} = \frac{x_{O_2}^{Dry\ air}\left(1 - x_{H_2O}^{Stack\ inlet}\right)}{1 + f_{O_2} \times \left(1 - x_{O_2}^{Dry\ air}\right)} P_{Inlet}^{Stack} \quad (S110)$$

Third, using the ideal gas law, one can easily show that f_{O_2} is linearly proportional to the H_2 consumed to CO_2 removed ratio in the EDCS unit, as shown in equation S111.

$$\left(\frac{H_2\ consumed\ in\ EDCS}{CO_2\ removed\ by\ EDCS}\right) = \frac{\left(2 f_{O_2} x_{O_2}^{Dry\ air}\right)}{\left(x_{CO_2}^{Inlet\ EDCS} - x_{CO_2}^{Outlet\ EDCS}\right)};\ x_{CO_2}^{Inlet\ EDCS} = 420\ ppm\ and\ x_{CO_2}^{Outlet\ EDCS} = 4\ ppm \quad (S111)$$

Consequently, any percentage change in f_{O_2} will result in an identical percent change in the H_2 consumed to CO_2 removed ratio, a fact that we used in our single variable sensitivity analysis in the paper.

EDCS performance model calculations

As mentioned in the paper, EDCS is a small HEMFC unit placed upstream of a HEMFC stack on the cathode side, in which H_2 reacts with O_2 and produces H_2O and heat. If left unchecked, the heat released in the EDCS unit can result in significant temperature increases within the unit, quickly degrading the ionomer in the membrane and electrodes. Unlike the FC stack, the shorted membrane EDCS with a spiral-wound structure that we included in our HEMFC system has no cooling cells in its construction.[40] Consequently, we decided to add a reasonable heat management strategy for the EDCS. In this strategy, a pump injects the liquid H_2O gathered in the anode demister to the anode purge flow in the EDCS. A portion of the liquid H_2O injected into the H_2 flow in the EDCS will evaporate and enable the isothermal operation of the EDCS. This evaporated water will end up in the airflow of the EDCS due to its higher flow rate. Since we implemented a

reasonable heat management strategy for the EDCS, we assumed the operating temperature of EDCS (T_{EDCS}) to be the same as the operating temperature of the FC stack (95 °C).

First, following the definition of f_{O_2}, we can calculate the molar flow rate of gaseous H_2O ($n_{H_2O-Produced}^{EDCS}$; mol/s) produced in the EDCS by equation S112.

$$n_{H_2O-Produced}^{EDCS} = 0.012 \times \left(\frac{I_{BOP}}{2F}\right) \quad (S112)$$

Next, we can calculate the molar flow rate of H_2O ($n_{H_2O-Evaporated}^{EDCS}$; mol/s) that evaporates within EDCS and enables the isothermal operation of EDCS from the lower heating value of H_2 ($LHV_{H_2} = 241.111\ \frac{kJ}{mol}$)[41] and the latent heat of vaporization of H_2O ($\Delta H_{Vap,H_2O} = 40.89\ \frac{kJ}{mol}$)[41] by equations S113.

$$n_{H_2O-Evaporated}^{EDCS} = n_{H_2O-Produced}^{EDCS}\left(\frac{LHV_{H_2}}{\Delta H_{Vap,H_2O}}\right) \quad (S113)$$

Finally, we can calculate the molar flow rate of gaseous H_2O ($n_{H_2O}^{EDCS}$; mol/s) that ends up in the airflow of the EDCS by equation S114.

$$n_{H_2O}^{EDCS} = n_{H_2O-Produced}^{EDCS} + n_{H_2O-Evaporated}^{EDCS} = n_{H_2O-Produced}^{EDCS}\left(1 + \frac{LHV_{H_2}}{\Delta H_{Vap,H_2O}}\right) \quad (S114)$$

In our HEMFC system modeling, we assumed that inlet cathode RH, which is the same as the EDCS outlet RH, to be constant at 65%. Consequently, the gaseous H_2O that ends up in the airflow of the EDCS will reduce the humidification requirement and the cost of the membrane humidifier.

Previously, as presented in equation S115, we developed an EDCS performance model that correlates the EDCS active area (A_{EDCS}; m^2) to the mole fraction of CO_2 in the EDCS inlet air stream ($x_{CO_2}^{Inlet\ EDCS} = 420\ ppm$), the mole fraction of CO_2 in the EDCS outlet air stream ($x_{CO_2}^{Outlet\ EDCS} = 4\ ppm$), the volumetric flow rate of air at the conditions within the EDCS ($\dot{V}_{EDCS}$; m^3/s) and a total CO_2 capture mass transport resistance (R_{MT}; s/m).[42]

$$\ln\left(\frac{x_{CO_2}^{Inlet\ EDCS}}{x_{CO_2}^{Outlet\ EDCS}}\right) = \frac{A_{EDCS}}{R_{MT}\dot{V}_{EDCS}} \quad (S115)$$

We assumed the pressure drop within the EDCS (ΔP_{EDCS}) to be 0.072 atm (30 % of the pressure drop of the FC stack (0.24 atm)). We note that measuring the value of (ΔP_{EDCS}) and establishing the strategies to control/reduce it for EDCS units processing technologically relevant air flow rates corresponding to an 80 kW_{Net} FC stack should be a fundamental and urgent future research goal for the HEMFC community for two reasons. First, we note that the EDCS research and development efforts up until now have been focused on reducing R_{MT}.[40, 42] While this is a conceptually sound research strategy, the improvements in R_{MT} have been achieved by using air flow mediums with high inherent pressure drops that are not typically used in the FC industry, namely interdigitated flow fields and polypropylene/nickel mesh.[40, 42] Interdigitated flow fields are the flow fields of choice for redox flow batteries.[43] The flow field structure forces fluid flow into a portion of the electrode, improving mass transport at the cost of increased pressure drop.[43] As a point of comparison, United Technologies' benchmark computational fluid dynamic (CFD) results demonstrate that at equal area-specific flow rates and channel lengths, typical interdigitated flow fields have about four times higher pressure drops than parallel flow fields.[43] Polypropylene and

nickel mesh are porous mediums that will exert significant skin friction on the fluid flow through them. As a point of comparison, United Technologies' benchmark CFD results demonstrate that at equal area-specific flow rates and channel lengths, fluid flow through fibrous porous mediums with permeabilities of 10^{-10} m^2 and 10^{-9} m^2 will create pressure drops of about 50 to 5 times higher than the pressure drop of parallel flow fields.[43] The high inherent pressure drop of these air flow mediums clearly signifies the need to measure and control the pressure drop in EDCS units that are built based on them and process technologically relevant air flow rates. Second, our single variable sensitivity analysis demonstrates that EDCS pressure drop significantly impacts the overall FC system cost, comparable to the area-based cost of EDCS.

We note that the EDCS outlet pressure equals the stack inlet pressure (P_{Inlet}^{Stack}). As depicted in equation S116, we reasonably assumed the operating pressure of EDCS (P_{EDCS}) to be the average of the inlet and outlet pressure of EDCS.

$$P_{EDCS} = P_{Inlet}^{Stack} + \frac{\Delta P_{EDCS}}{2} \quad (S116)$$

As shown in equation S117, we reasonably assumed the total molar flow rate of air through the EDCS (n_{Total}^{EDCS}; mol/s) to be the average of the total molar flow rate of air at the inlet of the EDCS ($n_{Total-Inlet}^{EDCS}$; mol/s) and the outlet of EDCS ($n_{Total-Outlet}^{EDCS}$; mol/s) and used it to calculate the volumetric flow rate of air at the conditions within the EDCS ($\dot{V}_{EDCS}$; m^3/s) by the ideal gas law. We emphasize that both n_{Total}^{EDCS} and $\dot{V}_{EDCS}$ are linearly proportional to I_{BOP}.

$$n_{Total}^{EDCS} = \frac{(n_{Total-Inlet}^{EDCS} + n_{Total-Outlet}^{EDCS})}{2} \; and \; \dot{V}_{EDCS} = \frac{n_{Total}^{EDCS} R_g T_{EDCS}}{P_{EDCS}} \quad (S117)$$

We note that the total CO_2 capture mass transport resistance (R_{MT}) includes all mass transport

processes (i.e., molecular diffusion and Knudsen diffusion) and kinetic processes involving CO_2 at the cathode of EDCS.[42] Our measurements of R_{MT} in in-lab made EDCS units show that, at a P_{EDCS} of approximately 2.5 atm, R_{MT} is approximately 20 s/m.[40] We assumed that pressure-dependent and pressure-independent CO_2 capture mass transport resistances contribute equally to R_{MT} at $P_{EDCS} = 2.5\ atm$. Consequently, we calculated R_{MT} using equation S118.

$$R_{MT} = 10\left(\frac{s}{m}\right) + 4\left(\frac{s}{m.\ atm}\right)P_{EDCS} \quad (S118)$$

We note that for our 30 \$/kW$_{Net}$-case, we assumed that through research and innovation efforts ΔP_{EDCS} and R_{MT} could be reduced by 50 % ($\Delta P_{EDCS} = 0.036\ atm\ and\ R_{MT} = 5\left(\frac{s}{m}\right) + 2\left(\frac{s}{m.\ atm}\right)P_{EDCS}$).

EDCS cost model details

We can calculate the EDCS cost from the required EDCS active area (A_{EDCS}; m^2) and the area-based cost of the EDCS ($Cost_{EDCS\ -\ Area\ based}$; \$/m^2). Previously, we performed a detailed technoeconomic analysis for a shorted membrane EDCS with a spiral-wound structure that contained a total Pt electrocatalyst content of 0.02 mg/cm^2 and established that $Cost_{EDCS\ -\ Area\ based} = 40.88\ \frac{\$}{m^2}$.[40] We reasonably assumed that we could replace the Pt electrocatalyst with an anode of Ni/N-doped C (0.5 mg/cm^2) and a cathode of $MnCo_2O_4$/C (0.1 mg/cm^2; see caption of Figure S2 for the electrocatalyst material costs). Consequently, $Cost_{EDCS\ -\ Area\ based}$ would be reduced to 31.36 \$/m^2.

We added a reasonable heat management strategy for the EDCS, where a pump injects the liquid H_2O gathered in the anode demister to the anode purge flow in the EDCS. A portion of the

liquid H_2O injected into the H_2 flow in the EDCS will evaporate and enable the isothermal operation of the EDCS. This strategy requires the implementation of a coolant reservoir, a coolant pump, and coolant piping for the EDCS unit. As depicted in Table S3, we reasonably assumed the cost of these components to be 30% of the similar components in the low-temperature coolant loop of the 2018 LDV PEMFC system reported in the SA comprehensive report.[2]

Details of the performance model for the air management system

Pressure drop considerations

To calculate the power requirement of the electric motor of the CEM unit and the air management system cost, we need to determine the compressor's outlet pressure and the expander's inlet pressure. The desired stack inlet pressure plus any pressure drop within the BOP components upstream of the stack determines the outlet pressure of the compressor.[2] The BOP components upstream of the stack are the air pre-cooler, the dry side of the membrane humidifier, and EDCS (see Figure 1). The SA comprehensive report specifies the pressure drop through the air pre-cooler ($\Delta P_{Air\ pre-cooler}$) and the dry side of the membrane humidifier ($\Delta P_{Dry\ side\ humidifier}$) as 0.03 atm and 0.04 atm, and we adapted these values in our system model.[2] Consequently, we can correlate the compressor's outlet pressure ($P_{Comp,Out}$) to the stack inlet pressure (P_{Inlet}^{Stack}) through equation S119.

$$P_{Comp,Out} = P_{Inlet}^{Stack} + \Delta P_{Air\ pre-cooler} + \Delta P_{Dry\ side\ humidifier} + \Delta P_{EDCS} = P_{Inlet}^{Stack} + 0.07\ atm + \Delta P_{EDCS} \quad (S119)$$

Similarly, the desired stack inlet pressure minus the pressure drop of the stack and any pressure drop within the BOP components downstream of the stack determine the inlet pressure of the expander.[2] The BOP components downstream of the stack are the wet side of the membrane

humidifier and demister (see Figure 1). The SA comprehensive report specifies the pressure drop through the stack (ΔP_{Stack}), the wet side of the membrane humidifier ($\Delta P_{Wet\ side\ humidifier}$), and the demister ($\Delta P_{Demister}$) as 0.24 atm, 0.03 atm, and 0.04 atm, and we adapted these values in our system model.[2] Consequently, we can correlate the expander's inlet pressure ($P_{Exp,In}$) to the stack inlet pressure (P_{Inlet}^{Stack}) through equation S120.

$$P_{Exp,In} = P_{Inlet}^{Stack} - \Delta P_{Stack} - \Delta P_{Wet\ side\ humidifier} - \Delta P_{Demister} = P_{Inlet}^{Stack} - 0.31\ atm \quad (S120)$$

The specific heat capacity at constant volume (C_V), the specific heat capacity at constant pressure (C_P), and the ratio of the specific heat capacity at constant pressure to the specific heat capacity at constant volume (γ) calculations

To calculate the power requirement of the electric motor of the CEM unit, we need to determine the C_V, C_P, and γ for the air stream flowing through the compressor and the air stream flowing through the expander. We reasonably assumed that O_2, N_2, and H_2O obey the ideal gas law. Using statistical thermodynamics, one can prove that the C_V of a diatomic ideal gas (e.g., O_2 and N_2) and a non-linear triatomic ideal gas (e.g., H_2O) are equal to 2.5 R_g and 3 R_g (R_g: the universal gas constant=8.314 J/(mol.K)).[44] The C_P and C_V of an ideal gas are also correlated through equation S121.[41, 44]

$$C_P - C_V = R_g \quad (S121)$$

Table S4 summarizes the values of C_V, C_P, and γ for O_2, N_2, and H_2O that we used in our model. We reasonably assumed that air is a mixture of ideal gases and consequently calculated the C_V of air ($C_{V,Air}$; J/(mol.K)), C_P of air ($C_{P,Air}$; J/(mol.K)), and γ of air (γ_{Air}; J/(mol.K)) through equation S122.

$$C_{V,Air} = \sum_{k = O_2, N_2, H_2O} y_k C_{V,k};\ C_{P,Air} = \sum_{k = O_2, N_2, H_2O} y_k C_{P,k};\ \gamma_{Air} = \frac{C_{P,Air}}{C_{V,Air}} \quad (S122)$$

In equation S122, y_k, $C_{V,k}$, and $C_{P,k}$ are the mole fraction of component k in the gas mixture, C_V of component k in the gas mixture, and C_P of component k in the gas mixture.

CEM unit performance model calculations

We developed a detailed performance model for the CEM unit based on the information provided in the SA comprehensive report. The compressor of the CEM unit is a centrifugal compressor that consumes power to provide airflow at desired pressures.[2] We can calculate the compressor's power consumption through equations S123 and S124.

$$\dot{w}_{Comp,Ideal} = \left(n_{Air,Comp} R_g T_{Ambient}\right) \times \left(\frac{\gamma_{Air,Comp}}{\gamma_{Air,Comp} - 1}\right) \times \left(\left(\frac{P_{Comp,Out}}{P_{Ambient}}\right)^{\left(\frac{\gamma_{Air,Comp} - 1}{\gamma_{Air,Comp}}\right)} - 1\right) \quad (S123)$$

$$\dot{w}_{Comp} = \left(\frac{\dot{w}_{Comp,Ideal}}{\eta_{Comp}}\right) \quad (S124)$$

In equation S123, $n_{Air,Comp}$, $T_{Ambient}$, $\gamma_{Air,Comp}$, $P_{Comp,Out}$, and $P_{Ambient}$ are the molar flow rate of the air stream flowing through the compressor, ambient temperature, the ratio of the specific heat capacity at constant pressure to the specific heat capacity at constant volume for the air stream flowing through the compressor, the compressor's outlet pressure, and ambient pressure. $\dot{w}_{Comp,Ideal}$ mentioned in equation S123 is the power consumption of an ideal adiabatic reversible compressor.[41] In equation S124, $\dot{w}_{Comp}$ and η_{Comp} are the power consumption of the compressor and compressor efficiency. The SA comprehensive report specifies η_{Comp} as 0.71, which we used in our system model.[2] In our model, consistent with the SA comprehensive report, we set

$T_{Ambient}$ and $P_{Ambient}$ to be 40 °C and 1 atm.[2] We reasonably assumed the RH of ambient air to be 20 %. We note that $n_{Air,Comp}$ is linearly proportional to the BOP current (I_{BOP}) and thus, we can rearrange equation S124 to equation S125.

$$\dot{w}_{Comp} = V_{Comp}\left(P_{Inlet}^{Stack}, \Delta P_{EDCS}, f_{O_2}\right) I_{BOP} = V_{Comp} I_{BOP} \quad (S125)$$

In equation S125, V_{Comp} is an auxiliary parameter with the units of potential (Volts) that is a function of the stack inlet pressure (P_{Inlet}^{Stack}), the pressure drop within the EDCS (ΔP_{EDCS}), and the ratio of the molar flow rate of O_2 consumed in the EDCS unit to the molar flow rate of O_2 entering the stack (f_{O_2}).

The expander of the CEM unit is a radial-inflow expander that produces power from the air stream exiting the FC stack.[2] We can calculate the power generation of the expander through equations S126 and S127.

$$\dot{w}_{Exp,Ideal} = -\left(n_{Air,Exp} R_g T_{Stack}\right) \times \left(\frac{\gamma_{Air,Exp}}{\gamma_{Air,Exp} - 1}\right) \times \left(\left(\frac{P_{Ambient}}{P_{Exp,In}}\right)^{\left(\frac{\gamma_{Air,Exp} - 1}{\gamma_{Air,Exp}}\right)} - 1\right) \quad (S126)$$

$$\dot{w}_{Exp} = \eta_{Exp} \dot{w}_{Exp,Ideal} \quad (S127)$$

In equation S126, $n_{Air,Exp}$, T_{Stack}, $\gamma_{Air,Exp}$, and $P_{Exp,In}$ are the molar flow rate of the air stream flowing through the expander, the operating temperature of the FC stack (95 °C), the ratio of the specific heat capacity at constant pressure to the specific heat capacity at constant volume for the air stream flowing through the expander, and the expander's inlet pressure. $\dot{w}_{Exp,Ideal}$ mentioned in equation S126 is the power generation of an ideal adiabatic reversible expander.[41] In equation S127, $\dot{w}_{Exp}$ and η_{Exp} are the power generation of the expander and expander efficiency. The SA

comprehensive report specifies η_{Exp} as 0.73, which we used in our system model.[2] We note that $n_{Air,Exp}$ is linearly proportional to I_{BOP} and thus, we can rearrange equation S127 to equation S128.

$$\dot{w}_{Exp} = V_{Exp}\left(P_{Inlet}^{Stack}, f_{O_2}, RH_{Stack,Oulet}\right) I_{BOP} = V_{Exp} I_{BOP} \quad (S128)$$

In equation S128, V_{Exp} is an auxiliary parameter with the units of potential (Volts) that is a function of P_{Inlet}^{Stack}, f_{O_2}, and the stack's outlet RH ($RH_{Stack,Oulet}$).

The electric motor of the CEM unit receives power from the FC stack and drives the compressor with the help of the power generated by the expander.[2] We can calculate the power consumption of the electric motor through equation S129.

$$\dot{w}_{Motor} = \frac{\left(\dot{w}_{Comp} - \dot{w}_{Exp}\right)}{\eta_{Motor}} \quad (S129)$$

In equation S129, $\dot{w}_{Motor}$ and η_{Motor} are the power consumption of the electric motor and the electric motor's efficiency. The SA comprehensive report specifies η_{Motor} as 0.8, which we used in our system model.[2] By combining equations S125, S128, and S129, we can rearrange equation S129 to equation S130.

$$\dot{w}_{Motor} = V_{Motor}\left(P_{Inlet}^{Stack}, \Delta P_{EDCS}, f_{O_2}, RH_{Stack,Oulet}\right) I_{BOP} = V_{Motor} I_{BOP} \quad (S130)$$

In equation S130, V_{CEM} is an auxiliary parameter with the units of potential (Volts) that is a function of P_{Inlet}^{Stack}, ΔP_{EDCS}, f_{O_2}, and $RH_{Stack,Oulet}$.

We note that the PtCo/HSC used in GM's polarization curves (Figure 2, S3, and S4) is similar, to emphasize not identical, to the state-of-the-art PtCo/HSC that is used in the 2018 LDV PEMFC system reported in the SA comprehensive report.[3] As such, we run our pseudo-2-D FC model for

GM's PtCo/HSC cathode (Pt loadings=0.1 mg_{Pt}/cm^2) coupled with Pt/HSC anode (Pt loadings=0.025 mg_{Pt}/cm^2) for a PEMFC with operating conditions which were the same as the 2018 LDV PEMFC system reported in the SA comprehensive report ($P_{Inlet}^{Stack} = 2.5\ atm$, $T_{Stack} = 95\ ^{\circ}C$, H_2 stoichiometry=1.5, O_2 stoichiometry=1.5, inlet anode and cathode of 65% RH, and a cell voltage of 0.657 V) and found $RH_{Stack,Oulet}$ to be 100 %. Assuming the $RH_{Stack,Oulet}$ to be 100 % and the I_{BOP} to be the same as that of the 2018 LDV PEMFC system reported in the SA comprehensive report (134.50 kA),[2] equation S130 provides a value of 7.15 kW for $\dot{w}_{Motor}$, which compares reasonably with the corresponding value of 7.35 kW provided in the SA comprehensive report.[2] Out of an abundance of caution and to ensure that our CEM performance model provides the exact value for $\dot{w}_{Motor}$ as that of the 2018 LDV PEMFC system reported in the SA comprehensive report ($\dot{w}_{Motor,\,2018\,SA} = 7.35\ kW$), we calculated the power requirements of the compressor, expander, and electric motor using equations S131 to S133.

$$\dot{w}_{Comp} = V_{Comp,Adjusted} I_{BOP}; V_{Comp,Adjusted} = \left(\frac{\dot{w}_{Motor,\,2018\,SA}}{7.15\ kW}\right) V_{Comp} \quad (S131)$$

$$\dot{w}_{Exp} = V_{Exp,Adjusted} I_{BOP}; V_{Exp,Adjusted} = \left(\frac{\dot{w}_{Motor,\,2018\,SA}}{7.15\ kW}\right) V_{Exp} \quad (S132)$$

$$\dot{w}_{Motor} = V_{Motor,Adjusted} I_{BOP}; V_{Motor,Adjusted} = \left(\frac{\dot{w}_{Motor,\,2018\,SA}}{7.15\ kW}\right) V_{Motor} \quad (S133)$$

Details of the cost model for the air management system

The SA comprehensive report provides an air management system cost model that correlates the air management system's cost ($C_{Air,\,SA}$; $) to the compressor's outlet pressure ($P_{Comp,Out}$; atm) and the total parasitic power requirement of the FC system ($P_{Parasitic}$; kW) (equations S134).[2]

$$C_{Air,\,SA} = 284.96480 + \left(-57.0495 \times P_{Comp,Out}{}^{2}\right) + \left(267.9631 \times P_{Comp,Ou} + \left(3.9115 \times P_{Comp,Out} \times P_{Parasitic}\right)\right. \quad (S134)$$

The cost model presented in equation S134 does not incorporate the scenario where the FC system does not need an expander (i.e., when the air stream enters the expander at atmospheric pressure). We included this scenario in the cost model by applying a suitable correction term based on the information provided in the SA comprehensive report.

Table S5 provides the cost breakdown for the air management system for the 2018 LDV PEMFC system reported in the SA comprehensive report ($P_{Comp,Out} = 2.57\ atm$ and $P_{Parasitic} = 8.37\ kW$) for two cases, one with an expander and one without an expander.[2] According to the SA comprehensive report, 30% of the motor controller cost for the 2018 LDV PEMFC system corresponds to its logic functions, with the remaining 70% corresponding to its power management.[2] The cost of the logic circuitry portion of the motor controller is constant and independent of $P_{Parasitic}$, but the cost of the power management portion of the motor controller scales linearly with $P_{Parasitic}$.[2] Consequently, we can calculate the cost of the motor controller ($C_{Controller,Air}$; \$) using equation S135.

$$C_{Controller,Air} = \left(36.60754 \times P_{Parasitic} + 131.31647\right);\ if\ P_{Parasitic} = 8.37\ kW \Rightarrow C \\ 437.72\ \$ \quad (S135)$$

In addition, the cost of the air management components other than the CEM unit (including the motor controller) remains constant ($C_{Other,\,Air} = 237.84\ \$$; Table S5).[2] So, we can calculate the cost of the CEM ($C_{CEM,Air}$; \$) using equation S136.

$$C_{CEM,Air} = C_{Air,SA} - C_{Controller,Air} - C_{Other,Air} = \left(-84.18816 + \left(-57.0495 \times \right. \right. \quad (S136)$$

By close inspection of Table S5, we can see that the ratio of compressor-motor (CM) cost to compressor-expander-motor (CEM) cost is 0.67076 for the 2018 LDV PEMFC system, and we reasonably assumed that this ratio remains the same for different values of $P_{Comp,Out}$ and $P_{Parasitic}$. Consequently, we can calculate the cost of CM ($C_{CM,Air}$; \$) using equation S137.

$$C_{CM,Air} = 0.67076 \times C_{CEM,Air} = 0.67076 \times \left(-84.18816 + \left(-57.0495 \times P_{Comp,\ Out}{}^{2} \right) \right. \quad (S137)$$

Following the above discussion, we calculated the air management system cost (C_{Air}; \$) using equations S138-1 and S138-2. Basically, we used the same cost function as that of the SA comprehensive report when the pressure of the airstream entering the expander was higher than atmospheric pressure. When the pressure of the airstream entering the expander was equal to the atmospheric pressure, we used equation S137 in the cost functions instead of equation S136.

$$If \left(P_{Inlet}^{Stack} > 1.31\ atm \right): C_{Air} = C_{Other,\ Air} + C_{Controller,\ Air} + C_{CEM,\ Air} = C_{Air,\ SA} \quad (S138-1)$$

$$If \left(P_{Inlet}^{Stack} = 1.31\ atm \right): C_{Air} = C_{Other,\ Air} + C_{Controller,\ Air} + C_{CM,\ Air} \quad (S138-2)$$

We note that the SA comprehensive report outlines a cost reduction in the CEM unit (including the motor controller) of the 2018 LDV PEMFC system of 300 \$, which is expected to be achieved in the future through research and innovation.[2] This cost reduction results in a 37.454% cost reduction in the CEM unit (including the motor controller) cost of the 2018 LDV PEMFC system, and we reasonably assumed that this 37.454% cost reduction in the CEM unit remains the same

for different values of $P_{Comp,Out}$ and $P_{Parasitic}$. Consequently, for our 30 \$/kW$_{Net}$ LDV systems, we calculated the air management system cost (C_{Air}; \$) using equations S139-1 and S139-2.

$$If\ \left(P_{Inlet}^{Stack} > 1.31\ atm\right): C_{Air} = C_{Other,\ Air} + 0.62546 \times (C_{Controller,\ Air} + C_{CEM,\ Air})\ \ (S139-1)$$

$$If\ \left(P_{Inlet}^{Stack} = 1.31\ atm\right): C_{Air} = C_{Other,\ Air} + 0.62546 \times (C_{Controller,\ Air} + C_{CM,\ Air})\ \ (S139-2)$$

Details of the performance model for the cross-flow membrane humidifier in the humidification management system

Cross-flow membrane humidifier structural details

Figure S7 shows a schematic diagram of the cross-flow membrane humidifier in which streams of dry air from the air pre-cooler outlet and humid, O_2-depleted air from the FC cathode outlet exchange water through a four-layer composite membrane. The composite membrane layers are made by slot die coating a (5 μm) layer of Nafion ionomer onto a (10 μm) ePTFE layer on a Mylar backer (the Mylar backer is removed after slot die coating). A second ePTFE layer is then rolled on top, and the three layers pass through a curing oven. Finally, to make a four-layer membrane, all three layers are hot-laminated to a (180 μm) polyethylene terephthalate (PET) porous layer.[2] We reasonably assumed the porosity of ePTFE and PET layers to be 0.95 and that we can calculate the tortuosity of the layers using the Bruggeman correlation (equation S4).

Cross-flow membrane humidifier model calculations

As mentioned in the paper, the air pre-cooler sits between the centrifugal compressor and the membrane humidifier and cools the hot compressed air exiting the compressor to the stack's operating temperature (95 °C). We reasonably assumed that the humidifier operates at 95 °C. Using the cross-flow heat exchanger modeling framework available in the literature, we developed a performance model for the cross-flow membrane humidifier that allowed us to calculate the

required humidifier membrane area.

In heat exchanger design, the rate of heat transfer (Q; W) to or from a stream experiencing a temperature change from T_1 to T_2 is calculated using equation S140.[45]

$$Q = \Delta\dot{H} = \dot{m}\Delta h = \dot{m}\int_{T_1}^{T_2} C_P dT \cong \dot{m} C_{P,Avg}\Delta T;\ C_{P,Avg} = \frac{(C_P(T_1) + C_P(T_2))}{2} \quad (S140)$$

In equation S140, ($\dot{H}$; W) is the enthalpy flow rate of the stream, ($\dot{m}$; kg/s) is the mass flow rate of the stream, (h; J/kg) is the specific enthalpy of the stream, (C_P: J/(kg.K)) is the specific heat capacity at constant pressure, ($\Delta T = T_2 - T_1$) is the temperature difference, and $C_{P,Avg}$ is the average of C_P's calculated at T_1 and T_2. The heat transfer flux at any point within the heat exchanger (q_{Local}; W/m^2) is calculated using equation S141.[45]

$$q_{Local} = U\Delta T_{Local} \quad (S141)$$

In equation S141, (U; W/(m^2.K) is the overall heat transfer coefficient and (ΔT_{Local}) is the local temperature difference between the hot and cold streams.

One can describe the performance of a cross-flow heat exchanger using equations S142-1 and S142-2.[46]

$$\xi_{HE} = 1 - exp\left(\frac{NTU_{HE}^{0.22}}{C_{r,HE}}\left(exp\left(\left(-C_{r,HE}NTU_{HE}^{0.78}\right) - 1\right)\right)\right) \quad (S142-1)$$

$$\xi_{HE} = \frac{Q_{HE}}{Q_{HE,Max}};\ NTU_{HE} = \frac{UA_{HE}}{\min\left(\left(\dot{m}C_{p,Avg}\right)_H, \left(\dot{m}C_{p,Avg}\right)_C\right)};\ C_{r,HE} = \frac{\min\left(\left(\dot{m}C_{p,Avg}\right)_H, \left(\dot{m}C_{p,Avg}\right)_C\right)}{\max\left(\left(\dot{m}C_{p,Avg}\right)_H, \left(\dot{m}C_{p,Avg}\right)_C\right)} \quad (S142-2)$$

In equation S142-1, ξ_{HE}, NTU_{HE}, and $C_{r,HE}$ are dimensionless parameters called the effectiveness of the heat exchanger, the number of transfer units, and the heat capacity rate ratio.

Equation S142-2 provides the definition of ξ_{HE}, NTU_{HE} , and $C_{r,HE}$: 1) ξ_{HE} is defined as the actual rate of heat transfer (Q_{HE}; W) in the cross-flow heat exchanger divided by the thermodynamically maximum rate of heat transfer ($Q_{HE,Max}$; W) possible between the hot and cold streams flowing in a counterflow heat exchanger of infinite heat transfer area. $Q_{HE,Max}$ can be calculated by checking which of the two scenarios depicted in Figure S8 is the thermodynamically feasible one (see Figure S8's caption for more details), and 2) In the definition of NTU_{HE} and $C_{r,HE}$, A_{HE}, $\left(\dot{m}C_{p,Avg}\right)_H$, and $\left(\dot{m}C_{p,Avg}\right)_C$ are the heat transfer area of the cross-flow heat exchanger, the mass flow rate multiplied by the average specific heat capacity at constant pressure for the hot stream, and the mass flow rate multiplied by the average specific heat capacity at constant pressure for the cold stream.

We note that heat transfer in a cross-flow heat exchanger is conceptually quite similar to mass transfer in a cross-flow membrane humidifier, so we sought to use this similarity to properly define humidifier effectiveness (ξ_{Hum}), the number of transfer units of the humidifier (NTU_{Hum}), and the heat capacity rate ratio of the humidifier ($C_{r,Hum}$) such that we could use equation S142-1 to determine the required humidifier membrane area (A_{Hum}). First, we defined an average H_2O mole fraction for the wet and dry gas channels of the humidifier ($x_{H_2O,Wet\ Avg}$ and $x_{H_2O,\ Dry\ Avg}$) and an average pressure for the wet and dry gas channels of the humidifier ($P_{Wet\ Avg}$ and $P_{Dry\ Avg}$) using equations S143 and S144.

$$x_{H_2O,Wet\ Avg} = \left(\frac{x_{H_2O,\ Wet\ in} + x_{H_2O,\ Wet\ out}}{2}\right) \ \&\ x_{H_2O,\ Dry\ Avg} = \left(\frac{x_{H_2O,\ Dry\ in} + x_{H_2O,\ Dry\ out}}{2}\right) \quad (S143)$$

$$P_{Wet\ Avg} = \left(\frac{P_{\ Wet\ in} + P_{Wet\ out}}{2}\right) \ \&\ P_{Dry\ Avg} = \left(\frac{P_{Dry\ in} + P_{Dry\ out}}{2}\right) \quad (S144)$$

In equation S143, $x_{H_2O,\,Wet\,in}$, $x_{H_2O,\,Wet\,out}$, $x_{H_2O,\,Dry\,in}$, and $x_{H_2O,\,Dry\,out}$ are the inlet and outlet H_2O mole fractions for the wet gas channel and the inlet and outlet H_2O mole fractions for the dry gas channel. In equation S144, $P_{Wet\,in}$, $P_{Wet\,out}$, $P_{Dry\,in}$, and $P_{Dry\,out}$ are the wet gas channel's inlet and outlet pressure and the dry gas channel's inlet and outlet pressure. Second, we reasonably assumed that the gas phase diffusion of H_2O through the wet PET, wet ePTFE, and dry ePTFE layers happens due to molecular diffusion and that the Knudsen diffusion through these layers is negligible (see Figure S7 for the structural details of layers). Using equation S8, we calculated an effective H_2O diffusion coefficient at the inlet and outlet of the wet gas channel ($D_{H_2O}^{Eff,Wet\,in}$ and $D_{H_2O}^{Eff,Wet\,out}$) and the inlet and outlet of the dry gas channel ($D_{H_2O}^{Eff,Dry\,in}$ and $D_{H_2O}^{Eff,Dry\,out}$). Subsequently, we defined an average effective H_2O diffusion coefficient for the humidifier's wet and dry gas channels ($D_{H_2O}^{Eff,Wet\,Avg}$ and $D_{H_2O}^{Eff,Dry\,Avg}$) using equation S145.

$$D_{H_2O}^{Eff,Wet\,Avg} = \frac{D_{H_2O}^{Eff,Wet\,in} + D_{H_2O}^{Eff,Wet\,out}}{2} \;\&\; D_{H_2O}^{Eff,Dry\,Avg} = \frac{D_{H_2O}^{Eff,Dry\,in} + D_{H_2O}^{Eff,Dry\,out}}{2} \quad (S145)$$

Third, we note that one side of the Nafion layer is adjacent to the wet gas channel of the humidifier, and the other is adjacent to the dry gas channel of the humidifier (Figure S7). Using equation S17, we calculated H_2O permeability in Nafion at the inlet and outlet of the wet gas channel ($D_{\hat{a},H_2O}^{Mem,Wet\,in}$ and $D_{\hat{a},H_2O}^{Mem,Wet\,out}$), which allowed us to calculate a reasonable estimate of the H_2O permeability ($D_{\hat{a},H_2O}^{Mem,Avg\,Wet}$) for the side of the Nafion layer adjacent to the humidifier's wet gas channel (equation S146).

$$D_{\hat{a},H_2O}^{Mem,Avg\,Wet} = \frac{D_{\hat{a},H_2O}^{Mem,Wet\,in} + D_{\hat{a},H_2O}^{Mem,Wet\,out}}{2} \quad (S146)$$

Similarly, using equation S17, we calculated H_2O permeability in Nafion at the inlet and outlet of the dry gas channel ($D^{Mem,\,Dry\,in}_{\hat{a},H_2O}$ and $D^{Mem,Dry\,out}_{\hat{a},H_2O}$), which allowed us to calculate a reasonable estimate of the H_2O permeability ($D^{Mem,\,Avg\,Dry}_{\hat{a},H_2O}$) for the side of the Nafion layer adjacent to the humidifier's dry gas channel (equation S147).

$$D^{Mem,\,Avg\,Dry}_{\hat{a},H_2O} = \frac{D^{Mem,Dry\,in}_{\hat{a},H_2O} + D^{Mem,Dry\,out}_{\hat{a},H_2O}}{2} \quad (S147)$$

Subsequently, we calculated a reasonable estimate of the H_2O permeability ($D^{Mem,\,Avg}_{\hat{a},H_2O}$) of the Nafion layer using equation S148.

$$D^{Mem,\,Avg}_{\hat{a},H_2O} = \frac{D^{Mem,\,Avg\,Wet}_{\hat{a},H_2O} + D^{Mem,\,Avg\,Dry}_{\hat{a},H_2O}}{2} \quad (S148)$$

Forth, we can calculate the molar flow rate of H_2O ($n^{Air}_{H_2O}$; mol/s) in an air stream from the molar flow rate of O_2 ($n^{Air}_{O_2}$; mol/s), the molar flow rate of N_2 ($n^{Air}_{N_2}$; mol/s), and H_2O mole fraction ($x^{Air}_{H_2O}$) of that stream using S149.

$$n^{Air}_{H_2O} = \left(\frac{x^{Air}_{H_2O}}{1 - x^{Air}_{H_2O}}\right) n_{O_2\,\&\,N_2}^{Air};\; n_{O_2\,\&\,N_2}^{Air} = (n^{Air}_{O_2} + n^{Air}_{N_2}) \quad (S149)$$

By assigning a constant average pressure (P_{Avg}) to the air stream, and using the relation between H_2O activity ($\hat{a}_{H_2O}$) and H_2O mole fraction ($x_{H_2O} = \frac{P^{Sat}_{H_2O}\hat{a}_{H_2O}}{P_{Avg}}$; $P^{Sat}_{H_2O}$: H_2O saturation pressure), we can rearrange equation S149 to S150.

$$n_{H_2O}^{Air} = n_{O_2\,\&\,N_2}^{Air}\left(\frac{P_{H_2O}^{Sat}\hat{a}_{H_2O}}{P_{Avg} - P_{H_2O}^{Sat}\hat{a}_{H_2O}}\right) = n_{O_2\,\&\,N_2}^{Air}\int_0^{\hat{a}_{H_2O}}\frac{P_{H_2O}^{Sat}P_{Avg}}{\left(P_{Avg} - P_{H_2O}^{Sat}\hat{a}_{H_2O}\right)^2}d\hat{a}_{H_2O} \quad (S150)$$

Consequently, we can calculate the change in the H_2O molar flow rate of an air stream experiencing H_2O activity/H_2O mole fraction change from $(\hat{a}_{H_2O,1}/x_{H_2O,1})$ to $(\hat{a}_{H_2O,2}/x_{H_2O,2})$ using equations S151-1 to S151-3.

$$\Delta n_{H_2O}^{Air} = n_{O_2\,\&\,N_2}^{Air}\int_{\hat{a}_{H_2O,1}}^{\hat{a}_{H_2O,2}}\frac{P_{H_2O}^{Sat}P_{Avg}}{\left(P_{Avg} - P_{H_2O}^{Sat}\hat{a}_{H_2O}\right)^2}d\hat{a}_{H_2O} \cong n_{O_2\,\&\,N_2}^{Air}\left(\frac{P_{H_2O}^{Sat}P_{Avg}}{\left(P_{Avg} - P_{H_2O}^{Sat}\hat{a}_{H_2O}\right)^2}\right)_{Avg}\Delta\hat{a}_{H_2O} \quad (S151-1)$$

$$\left(\frac{P_{H_2O}^{Sat}P_{Avg}}{\left(P_{Avg} - P_{H_2O}^{Sat}\hat{a}_{H_2O}\right)^2}\right)_{Avg} = \frac{P_{H_2O}^{Sat}}{P_{Avg}}\left(\frac{1}{\left(1 - x_{H_2O}\right)^2}\right)_{Avg} \quad (S151-2)$$

$$\left(\frac{1}{\left(1 - x_{H_2O}\right)^2}\right)_{Avg} = \frac{\frac{1}{\left(1 - x_{H_2O,1}\right)^2} + \frac{1}{\left(1 - x_{H_2O,2}\right)^2}}{2} \quad (S151-3)$$

By comparing equations S140 and S151-1, we can see that the role of C_P in calculating ΔH is similar to the role of $\frac{P_{H_2O}^{Sat}P_{Avg}}{\left(P_{Avg} - P_{H_2O}^{Sat}\hat{a}_{H_2O}\right)^2}$ in calculating $\Delta n_{H_2O}^{Air}$. Consequently, the same way that one uses $C_{P,Avg}$ to define $C_{r,HE}$, we can use $\left(\frac{P_{H_2O}^{Sat}}{P_{Avg}}\left(\frac{1}{\left(1 - x_{H_2O}\right)^2}\right)_{Avg}\right)$ to define $C_{r,Hum}$ (equation S152).

$$C_{r,Hum}=\frac{\min\left(\left(n_{O_2\ \&\ N_2}^{Air}\frac{P_{H_2O}^{Sat}}{P_{Avg}}\left(\frac{1}{(1-x_{H_2O})^2}\right)_{Avg}\right)_{Wet},\left(n_{O_2\ \&\ N_2}^{Air}\frac{P_{H_2O}^{Sat}}{P_{Avg}}\left(\frac{1}{(1-x_{H_2O})^2}\right)_{Avg}\right)_{Dry}\right)}{\max\left(\left(n_{O_2\ \&\ N_2}^{Air}\frac{P_{H_2O}^{Sat}}{P_{Avg}}\left(\frac{1}{(1-x_{H_2O})^2}\right)_{Avg}\right)_{Wet},\left(n_{O_2\ \&\ N_2}^{Air}\frac{P_{H_2O}^{Sat}}{P_{Avg}}\left(\frac{1}{(1-x_{H_2O})^2}\right)_{Avg}\right)_{Dry}\right)} \quad (S152)$$

In equation S152, the index Avg, Wet, and Dry refer to the average between the inlet and outlet of an air stream in the humidifier, air stream flowing in the humidifier's wet/dry gas channels. Fifth, we can calculate the H_2O transfer flux at any point within the humidifier (N_{H_2O}; mol/(m^2.s)) using equations S153-1 and S153-2.

$$N_{H_2O}=\frac{\Delta\hat{a}_{H_2OLocal}}{R_{Total}};\ R_{Total}=R_{Wet\ PET}+R_{Wet\ ePTFE}+R_{Mem}+R_{Dry\ ePTFE} \quad (S153-1)$$

$$R_{Wet\ PET}=\left(\frac{t_{Wet\ PET}}{D_{H_2O}^{Eff,\,Wet\ Avg}C_{H_2O}^{Sat}}\right);\ R_{Wet\ ePTFE}=\left(\frac{t_{Wet\ ePTFE}}{D_{H_2O}^{Eff,\,Wet\ Avg}C_{H_2O}^{Sat}}\right);\ R_{Mem}=\left(\frac{}{D}\right.$$
$$=\left(\frac{t_{Drt\ ePTFE}}{D_{H_2O}^{Eff,Dry\ Avg}C_{H_2O}^{Sat}}\right) \quad (S153-2)$$

In equation S153-1, $\Delta\hat{a}_{H_2OLocal}$, R_{Total}, $R_{Wet\ PET}$, $R_{Wet\ ePTFE}$, R_{Mem}, and $R_{Dry\ ePTFE}$ are the local H_2O activity difference between the wet and dry streams, total H_2O mass transfer resistance, and H_2O mass transfer resistance in the wet PET layer/wet ePTFE layer/Nafion layer/dry ePTFE layer. In equation S153-2, $t_{Wet\ PET}$, $t_{Wet\ ePTFE}$, t_{Mem}, $t_{Drt\ ePTFE}$, and $C_{H_2O}^{Sat}$ are the thickness of the wet PET layer/wet ePTFE layer/Nafion layer/dry ePTFE layer and H_2O saturation concentration ($C_{H_2O}^{Sat}=\frac{P_{H_2O}^{Sat}}{R_gT_{Stack}}$). By comparing equations S141 and S153-1, we can see that the role of U in

calculating q_{Local} is similar to the role of $(\frac{1}{R_{Total}})$ in calculating N_{H_2O}. Consequently, the same way that one uses U to define NTU_{HE}, we can use $(\frac{1}{R_{Total}})$ to define NTU_{Hum} (equation S154).

$$NTU_{Hum} = \frac{A_{Hum}}{R_{Total} \min\left(\left(n_{O_2\,\&\,N_2}^{Air} \frac{P_{H_2O}^{Sat}}{P_{Avg}} \left(\frac{1}{(1-x_{H_2O})^2}\right)_{Avg}\right)_{Wet}, \left(n_{O_2\,\&\,N_2}^{Air} \frac{P_{H_2O}^{Sat}}{P_{Avg}} \left(\frac{1}{(1-x_{H_2O})^2}\right)_{Avg}\right)_{Dry}\right)} \quad (S154)$$

Sixth, we can define ξ_{Hum} using a similar equation that is used to define ξ_{HE} (equation S155).

$$\xi_{Hum} = \frac{Q_{Hum}}{Q_{Hum,Max}} \quad (S155)$$

In equation S155, (Q_{Hum}; mol/s) is the actual rate of H_2O transfer in the cross-flow humidifier divided by the thermodynamically maximum rate of H_2O transfer ($Q_{Hum,Max}$; mol/s) possible between the wet and dry air streams flowing in a counterflow humidifier of infinite membrane area. $Q_{Hum,Max}$ can be calculated by checking which of the two scenarios depicted in Figure S9 is the thermodynamically feasible one (see Figure S9's caption for more details). Seventh, assuming the $RH_{Stack,Oulet}$ to be 100 % ($\hat{a}_{H_2O,\,Stack,\,Oulet} = 1$) for the 2018 LDV PEMFC system reported in the SA comprehensive report, our cross-flow membrane humidifier performance model provides a value of 0.6776 m^2 for A_{Hum}, which compares reasonably with the corresponding value of 0.675 m^2 provided in the SA comprehensive report.[2] Out of an abundance of caution and to ensure that our cross-flow membrane humidifier performance model provides the exact value for A_{Hum} as that of the 2018 LDV PEMFC system reported in the SA comprehensive report ($A_{Hum,\,2018\,SA} = 0.675\ m^2$), we calculated the area of the cross-flow membrane humidifier (A_{Hum})

using equation S156.

$$A_{Hum} = \left(\frac{A_{Hum,\,2018\,SA}}{0.6776\ m^2}\right) A_{Hum,\,S142-1} \quad (S156)$$

In equation S156, $A_{Hum,\,S142-1}$ is the cross-flow membrane humidifier area that results from equation S142-1. Finally, we note that for our 30 \$/kW$_{Net}$-case, we assumed that through research and innovation efforts $t_{Wet\,PET}$, $t_{Wet\,ePTFE}$, and $t_{Drt\,ePTFE}$ can be reduced to 85 μm, 7 μm, and 7 μm, and that the H_2O permeability in the 5 μm thin membrane can be increased by 200 % (i.e., it would become three times that of the H_2O permeability of the Nafion layer).

Details of the cost model for the humidification management system

The SA comprehensive report provides a humidification management system cost model that correlates the humidification management system's cost (C_{Humid}; \$) to the cross-flow membrane humidifier membrane area (A_{Hum}; m^2), heat duty of the air pre-cooler ($Q_{Pre-cooler}$; kW), and the difference between the temperature of the compressor exit air and the coolant temperature entering into the air pre-cooler ($\Delta T_{Pre-cooler}$; °C) (equation S157).[2]

$$C_{Humid} = \left(-1.48979 \times {A_{Hum}}^2 + 64.37770 \times A_{Hum} + 14.25859\right) + \left(642.0 \quad (S157)$$

We explained in detail in the previous section how to calculate A_{Hum} (equation S156). We note that the compressor operates through an adiabatic process,[41] hence through energy balance, we can correlate the power consumption of the compressor ($\dot{W}_{Comp}$) to the molar flow rate of the air stream flowing through the compressor ($n_{Air,Comp}$), specific heat capacity at constant pressure

for the air stream flowing through the compressor ($C_{P,\,Air,\,Comp}$), the compressor's outlet temperature ($T_{Comp,Out}$), and the ambient temperature ($T_{Ambient} = 40\ ℃$) (equation S158).

$$\dot{w}_{Comp} = n_{Air,Comp} C_{P,\,Air,\,Comp} \times \left(T_{Comp,Out} - T_{Ambient}\right) \quad (S158)$$

We can calculate $Q_{Pre-cooler}$ from an energy balance of the pre-cooler unit as detailed in equation S159 (T_{Hum} is humidifier's operating temperature (95 °C)).

$$Q_{Pre-cooler} = n_{Air,Comp} C_{P,\,Air,\,Comp} \times \left(T_{Comp,Out} - T_{Hum}\right) = \dot{w}_{Comp} + n_{Air,Comp} C_{P,\,Ai} \quad (S159)$$

We can combine equation S159 with equation S131 and derive the following equation for $Q_{Pre-cooler}$.

$$Q_{Pre-cooler} = V_{Pre-cooler}\left(P_{Inlet}^{Stack}, \Delta P_{EDCS}, f_{O_2}\right) I_{BOP} = V_{Pre-cooler} I_{BOP} \quad (S160)$$

In equation S125, $V_{Pre-cooler}$ is an auxiliary parameter with the units of potential (Volts) that is a function of the stack inlet pressure (P_{Inlet}^{Stack}), the pressure drop within the EDCS (ΔP_{EDCS}), and the ratio of the molar flow rate of O_2 consumed in the EDCS unit to the molar flow rate of O_2 entering the stack (f_{O_2}). The SA comprehensive report provides a value of 118 °C for the $\Delta T_{Pre-cooler}$ of the 2018 LDV PEMFC system.[41] From equation S158, we calculated the $T_{Comp,Out}$ for the 2018 LDV PEMFC system to be 180.06 °C, which means that the coolant temperature entering into the air pre-cooler for the 2018 LDV PEMFC system is 62.06 °C. We adopted this value for the calculation of $\Delta T_{Pre-cooler}$ of our system (i.e., $\Delta T_{Pre-cooler} = T_{Comp,Out} - 62.06\ ℃$).

Details of the cost model for the thermal management system

The SA comprehensive report provides a thermal management system cost model that correlates the thermal management system's cost ($C_{Thermal}$; $) to the radiator duty ($Q_{HTCL}$; kW) of the high-temperature coolant loop (HTCL), the difference between the operating temperature of the FC stack ($T_{Stack} = 95$ ℃) and ambient temperature ($T_{Ambient} = 40$ ℃) (ΔT_{HTCL} ;°C or K), the radiator duty (Q_{LTCL}; kW) of the low-temperature coolant loop (LTCL), the difference between the coolant outlet temperature from the air pre-cooler and $T_{Ambient}$ (ΔT_{LTCL} ;°C or K), and the FC stack inlet pressure (P_{Inlet}^{Stack}; atm) (equation S161).[2]

$$C_{Thermal} = \left(94.0853 \times \left(\frac{Q}{\Delta T}\right)_{HTCL} + 169.9283\right) + 0.9144 \times \left(\frac{Q}{\Delta T}\right)_{LTCL}^{2} + 101.$$
$$2.2211 \times P_{Inlet}^{Stack2} + 20.8371 \times P_{Inlet}^{Stack} - 2.4537 \times P_{Inlet}^{Stack} \times \left(\frac{Q}{\Delta T}\right)_{LTCL}$$
$$- 10.4304 \quad (S161)$$

According to the SA comprehensive report, Q_{HTCL} and $\left(\frac{Q}{\Delta T}\right)_{HTCL}$ can be calculated using equation S162.[2]

$$Q_{HTCL} = \frac{P_{Gross} \times (1.25 - V_{Cell})}{V_{Cell}}; \left(\frac{Q}{\Delta T}\right)_{HTCL} = \frac{P_{Gross} \times (1.25 - V_{Cell})}{V_{Cell} \times (T_{Stack} - T_{Ambient})} \quad (S162)$$

In equation S162, P_{Gross} is the gross power of the FC stack and V_{Cell} is the operating voltage of a single cell in the FC stack. We can calculate P_{Gross} using equation S163.

$$P_{Gross} = n_{Cell} I_{Cell} V_{Cell} = I_{BOP} V_{Cell} \quad (S163)$$

In equation S163, n_{Cell}, I_{Cell} , and I_{BOP} are the number of single cells in the FC stack, the FC

stack current, and the BOP current defined in equation S101. By inspecting equations S162 and S163, we can see that Q_{HTCL} and $(\frac{Q}{\Delta T})_{HTCL}$ are linearly proportional to I_{BOP} (equation S164).

$$Q_{HTCL} = I_{BOP} \times (1.25 - V_{Cell}); (\frac{Q}{\Delta T})_{HTCL} = \frac{I_{BOP} \times (1.25 - V_{Cell})}{(T_{Stack} - T_{Ambient})} \quad (S164)$$

The LTCL has a complicated structure, and it cools the motor of the CEM unit, the electronic components of the CEM unit, and the compressed air intake in the air pre-cooler before it goes into the membrane humidifier.[2] We decided to adopt a reasonable high-level approach to calculate $(\frac{Q}{\Delta T})_{LTCL}$, in which: 1) We used the values of $\left(\frac{Q}{\Delta T}\right)_{LTCL}$ provided in the SA comprehensive report for the 2018 LDV PEMFC system (0.36 kW/K) as a basis,[2] 2) We made a conceptually reasonable high-level assumption that Q_{LTCL} is proportional to the summation of the heat released in the motor of the CEM unit due to its inefficiency ($(1 - \eta_{Motor})\dot{w}_{Motor}$) and the heat duty of the pre-cooler ($Q_{Pre-cooler}$), and 3) We assumed that ΔT_{LTCL} of our system is the same as that of the 2018 LDV PEMFC system described in the SA comprehensive report. Subsequently, we calculated $\left(\frac{Q}{\Delta T}\right)_{LTCL}$ using equation S165.

$$(\frac{Q}{\Delta T})_{LTCL} = \frac{((1 - \eta_{Motor})\dot{w}_{Motor} + Q_{Pre-cooler})}{((1 - \eta_{Motor})\dot{w}_{Motor} + Q_{Pre-cooler})_{LTCL,2018\,SA}} \times \left(\frac{Q}{\Delta T}\right)_{LTCL,2018\,SA} \quad (S165)$$

In equation S165, $((1 - \eta_{Motor})\dot{w}_{Motor} + Q_{Pre-cooler})$ and $((1 - \eta_{Motor})\dot{w}_{Motor} + Q_{Pre-cooler})_{LTCL,2018\,SA}$ are the values of $((1 - \eta_{Motor})\dot{w}_{Motor} + Q_{Pre-cooler})$ calculated by our model for any FC system and the 2018 LDV PEMFC system described in the SA comprehensive report.

Details of calculating the parasitic power requirements of thermal management system components

The thermal management system includes a HTCL pump, a HTCL radiator fan, and a LTCL pump whose operation requires receiving power from the FC stack.[2] We reasonably assumed that any change in the radiator duty of HTCL or LTCL is compensated with a proportionate change in the flow rate of coolant in HTCL or LTCL. The change in the flow rate of coolant in HTCL or LTCL would conceptually require a proportional change in the power consumption of the HTCL pump, the HTCL radiator fan, and the LTCL pump. We calculated the power requirement of the HTCL pump ($P_{Pump,\ HTCL}$; kW) using equation S166.

$$\frac{P_{Pump,\ HTCL}}{P_{Pump,\ HTCL,\ 2018\,SA}} = \left(\frac{Q_{HTCL}}{Q_{HTCL,\,2018\,SA}}\right) = \frac{(1.25 - V_{Cell})}{(1.25 - V_{Cell,2018\,SA})} \times \left(\frac{I_{BOP}}{I_{BOP,\ 2018\,SA}}\right) \Rightarrow P_{Pump,\ HTCL} = V_{Pump,\ HTCL}(V_{Cell}) I_{BOP} \quad (S166)$$

In equation S166, $P_{Pump,\ HTCL,\ 2018\,SA}$, $Q_{HTCL,\,2018\,SA}$, $V_{Cell,2018\,SA}$, and $V_{Pump,\ HTCL}$ are the power requirement of the HTCL pump for the 2018 LDV PEMFC system (0.52 kW), the radiator duty of the HTCL for the 2018 LDV PEMFC system, the operating voltage of a single cell in the FC stack of the 2018 LDV PEMFC system (0.657 V) and a known auxiliary parameter with the units of potential (Volts) that is a function of V_{Cell}.[2] Using a similar line of argument, we calculated the power requirement of the HTCL radiator fan ($P_{Fan,\ HTCL}$; kW) and the LTCL pump ($P_{Pump,\ LTCL}$; kW) using equations S167 and S168.

$$\frac{P_{Fan,\ HTCL}}{P_{Fan,\ HTCL,\ 2018\,SA}} = \left(\frac{Q_{HTCL}}{Q_{HTCL,\,2018\,SA}}\right) = \frac{(1.25 - V_{Cell})}{(1.25 - V_{Cell,2018\,SA})} \times \left(\frac{I_{BOP}}{I_{BOP,\ 2018\,SA}}\right) \Rightarrow P_{Fan,\ HT}$$
$$(V_{Cell})I_{BOP} \quad (S167)$$

$$\frac{P_{Pump,\ LTCL}}{P_{Pump,\ LTCL,\ 2018\,SA}} = \left(\frac{Q_{LTCL}}{Q_{LTCL,\,2018\,SA}}\right) = \left(\frac{((1-\eta_{Motor})\dot{w}_{Motor} + Q_{Pre-cooler})}{((1-\eta_{Motor})\dot{w}_{Motor} + Q_{Pre-cooler})_{LTCL,2018\,SA}}\right.$$
$$= V_{Pump,\ LTCL}\left(P_{Inlet}^{Stack}, \Delta P_{EDCS}, f_{O_2}, RH_{Stack,Oulet}\right) I_{BOP} \quad (S168)$$

In equation S167, $P_{Fan,\ HTCL,\ 2018\,SA}$ and $V_{Fan,\ HTCL}$ are the power requirement of the HTCL fan for the 2018 LDV PEMFC system (0.35 kW)[2] and a known auxiliary parameter with the units of potential (Volts) that is a function of V_{Cell}. In equation S168, $P_{Pump,\ LTCL,\ 2018\,SA}$ and $V_{Pump,\ LTCL}$ are the power requirement of the LTCL pump for the 2018 LDV PEMFC system (0.05 kW)[2] and a known auxiliary parameter with the units of potential (Volts) that is a function of P_{Inlet}^{Stack}, ΔP_{EDCS}, f_{O_2}, and $RH_{Stack,Oulet}$.

Details of implementing the operational constraints relevant to FC systems for LDV applications

We note that the operation of a FC system for a LDV is subject to three critical constraints. In this section, we explain what these constraints are and how we implemented them in our FC system model.

Implementation of the first and second constraint

First, the BOP of the FC system includes some key components whose operation requires

receiving power from the FC stack. These components include the electric motor of the CEM unit, the HTCL pump, the HTCL radiator fan, the LTCL pump, and components such as the FC system controller and sensors.[2] In addition to providing the parasitic power requirements of these components, the FC stack has to deliver 80 kW of power to the electric traction motor of the LDV that drives the vehicle wheels.[2] Second, for compatibility with the electric traction motor of the LDV, the FC stack must deliver a system voltage of 250 V.[2]

To implement these two constraints, first, we need to calculate the total parasitic power requirement of the FC system ($P_{Parasitic}$; kW). We have already derived the expressions required to calculate the parasitic power requirements of the electric motor of the CEM unit, the HTCL pump, the HTCL radiator fan, and the LTCL pump. We presented these expressions in equations S133, S166, S167, and S168. We reasonably assumed that the parasitic power requirement (P_{Other}; kW) of components such as the FC system controller and sensors is constant and equal to the value reported in the SA comprehensive report (0.1 kW).[2] We can combine equations S133, S166, S167, and S168 to calculate $P_{Parasitic}$ (equation S169-1 and S169-2).

$$P_{Parasitic} = \left(V_{Motor}\left(P_{Inlet}^{Stack}, \Delta P_{EDCS}, f_{O_2}, RH_{Stack,Oulet}\right) + V_{Pump,\ HTCL}(V_{Cell}) + \right. \\ \times I_{BOP} + P_{Other} \\ = V_{Parasitic}\left(P_{Inlet}^{Stack}, \Delta P_{EDCS}, f_{O_2}, RH_{Stack,Oulet}, V_{Cell}\right) I_{BOP} + P_{Other} \quad (S1$$

$$V_{Parasitic}\left(P_{Inlet}^{Stack}, \Delta P_{EDCS}, f_{O_2}, RH_{Stack,Oulet}, V_{Cell}\right) \\ = V_{Motor}\left(P_{Inlet}^{Stack}, \Delta P_{EDCS}, f_{O_2}, RH_{Stack,Oulet}\right) + V_{Pump,\ HTCL}(V_{Cell}) + V_{Fan,\ HTCL} \\ (V_{Cell}) + V_{Pump,\ LTCL}\left(P_{Inlet}^{Stack}, \Delta P_{EDCS}, f_{O_2}, RH_{Stack,Oulet}\right) \quad (S169-2)$$

All variables in equation S169-1 are explained in the definition of variables of equations S133,

S166, S167, and S168. Equation S169-2 presents the definition of $V_{Parasitic}$, which is a known auxiliary parameter with the units of potential (Volts) that is a function of P_{Inlet}^{Stack}, ΔP_{EDCS}, f_{O_2}, $RH_{Stack,Oulet}$, and V_{Cell}.

The requirement that the FC stack must deliver a system voltage of 250 V means that we can correlate the number of single cells in the FC stack (n_{Cell}) to the operating voltage of a single cell in the FC stack (V_{Cell}) through equation S170.

$$n_{Cell} = \left(\frac{250}{V_{Cell}}\right) \ (S170)$$

We can calculate the gross power of the FC stack (P_{Gross}; kW) using equation S171.

$$P_{Gross} = n_{Cell} I_{Cell} V_{Cell} = \left(\frac{250}{V_{Cell}}\right) I_{Cell} V_{Cell} = 250 I_{Cell} \ (S171)$$

We note that we replaced n_{Cell} in equation S171 with the expression that we derived for it in equation S170, which allowed us to derive an expression that correlates P_{Gross} to only the FC stack current (I_{Cell}). By definition, P_{Gross} consists of two components: 1) The power requirement of the electric traction motor of the LDV that drives the vehicle wheels ($P_{Net} = 80\ kW$); 2) The total parasitic power requirement of the FC system ($P_{Parasitic}$; kW).[2] Consequently, we can write equations S172-1 and S172-2.

$$P_{Gross} = P_{Net} + P_{Parasitic} = P_{Net} + P_{Other} + V_{Parasitic} I_{BOP} = P_{Net\ \&\ Other} + \ (S172-1)$$

$$P_{Net\ \&\ Other} = P_{Net} + P_{Other} = 80.1\ kW \ \ (S172-2)$$

Equation S172-2 presents the definition of $P_{Net\ \&\ Other}$, which is a known constant. By combining equations S171 and S172-1, we can derive an expression for I_{Cell} (equation S173).

$$I_{Cell} = \frac{P_{Net\ \&\ Other}}{250 \times (1 - \frac{V_{Parasitic}}{V_{Cell}})} \quad (S173)$$

We can subsequently calculate the active area of a single cell in the FC stack ($A_{Active\ Cell}$) and the total active area of the stack ($A_{Active\ Stack}$) using equation S174.

$$A_{Active\ Cell} = \frac{I_{Cell}}{i_{Cell}};\ A_{Active\ Stack} = n_{Cell} A_{Active\ Cell} = \left(\frac{250}{V_{Cell}}\right) \times A_{Active\ Cell} \quad (S174)$$

In equation S174, (i_{Cell}; A/m^2) is the FC geometric current density provided by our comprehensive FC model, which, as we explained before, is independent of $A_{Active\ Cell}$.

Implementation of the third constraint

The third constraint states that the size of the radiator rejecting waste heat to ambient should be reasonable for incorporation into a light-duty automobile. According to the SA comprehensive report, placing a heat rejection criterion of ($(\frac{Q}{\Delta T})_{HTCL} \leq 1.45\ \frac{kW}{°C}$) ensures that the size of the radiator is reasonable.[2] Using equation S162, we can write the criterion as follows:

$$(\frac{Q}{\Delta T})_{HTCL} = \frac{P_{Gross} \times (1.25 - V_{Cell})}{V_{Cell} \times (T_{Stack} - T_{Ambient})} \leq 1.45\ \frac{kW}{°C} \quad (S175)$$

We can combine equations S171 and S173 to derive an expression that correlates P_{Gross} to only $V_{Parasitic}$ and V_{Cell} (equation S176).

$$P_{Gross} = 250 \times I_{Cell} = 250 \times \frac{P_{Net\ \&\ Other}}{250 \times (1 - \frac{V_{Parasitic}}{V_{Cell}})} = \frac{P_{Net\ \&\ Other}}{(1 - \frac{V_{Parasitic}}{V_{Cell}})} \quad (S176)$$

By substituting equation S176 in equation S175, we get the following inequality, which is

$$\frac{1.25 + (\frac{1.45 \times \Delta T_{HTCL}}{P_{Net\ \&\ Other}}) \times V_{Parasitic}\left(P_{Stack,\ Inlet}, \Delta P_{EDCS}, f_{O_2}, RH_{Stack,\ Oulet}, V_{Cell}\right)}{\left(\frac{1.45 \times \Delta T_{HTCL}}{P_{Net\ \&\ Other}}\right) + 1}$$
$$= V_{Lower\ bound}\left(P_{Stack,\ Inlet}, \Delta P_{EDCS}, f_{O_2}, RH_{Stack,\ Oulet}, V_{Cell}\right) \leq V_{Cell} \quad (S177)$$

In equation S177, (ΔT_{HTCL} ;°C) is the difference between the operating temperature of the FC stack ($T_{Stack} = 95$ ℃) and ambient temperature ($T_{Ambient} = 40$ ℃) and $V_{Lower\ bound}$ is a known auxiliary parameter with the units of potential (Volts) that is a function of P_{Inlet}^{Stack}, ΔP_{EDCS}, f_{O_2}, $RH_{Stack,Oulet}$, and V_{Cell}. Enforcing the inequality presented in equation S177 is mathematically equivalent to enforcing the inequality in equation S175.

We enforced the inequality in equation S177 using the well-known penalty function method.[47] This method adds a penalty function to the objective function. The penalty function significantly increases the objective function when the constraint is violated and subsequently eliminates the chance of being selected as the optimum for the set of free variables of optimization that violated the constraint.[47] The penalty function consists of a big positive number called the penalty parameter, which gets multiplied by the measure of constraint violation. The measure of constraint violation is the amount of constraint violation when the constraint is violated and is zero when the constraint is not violated.[47] Following the above discussion, we applied a cost penalty function to the total FC system cost for the LDV presented in equation 1 in the paper. Therefore, we

implemented equation 1 in the paper as equation S178 at the time of optimizing the total FC system cost.

$$C_{System} = C_{Stack} + C_{EDCS} + C_{Air} + C_{Humid} + C_{Thermal} + C_{Fuel} + C_{BOP,Addition}$$

In equation S178, (C_{System}; \$), (C_{Stack}; \$), (C_{EDCS}; \$), (C_{Air}; \$), (C_{Humid}; \$), ($C_{Thermal}$; \$), (C_{Fuel}; \$), and ($C_{BOP,Additional}$; \$) are the total FC system cost for the LDV, the FC stack cost, the EDCS unit cost, the air management system cost, the humidification management system cost, the thermal management system cost, the fuel management system cost, and the cost of additional BOP components. ($C_{Penalty}$; \$) is the cost penalty function defined in equation S179.

$$C_{Penalty} = 80 \times 10^6 \times \begin{cases} 0; & if\ (V_{Lower\ bound} \leq V_{Cell}) \\ (V_{Lower\ bound} - V_{Cell}); & if (V_{Lower\ bound} > V_{Cell}) \end{cases} \quad (S179)$$

As it is clear from equation S179, if the inequality in equation S177 is valid, the cost penalty would be zero. Any violation of the inequality in equation S177 will result in a significant increase in $C_{Penalty}$ and consequently C_{System}. For example, if $V_{Lower\ bound}$ is higher than V_{Cell} by only 0.001 mV, the cost penalty function will have the value of 80000 \$ (1000 \$/kW$_{Net}$), ensuring that the optimized FC system does not violate the inequality presented in equation S177.

Details of implementing the 1-D FC sandwich model that operated based on the average inlet and exit pressure and composition of the anode and cathode gas channels in our cost optimization approach in a computationally efficient manner

As mentioned in the paper, we optimized the total FC system cost using a 1-D FC sandwich model that operated based on the average inlet and exit pressure and composition of the anode and cathode gas channels. As mentioned before, the 1-D FC sandwich model is quite computationally

expensive, and for a complex multi-variable optimization problem like the one considered in this paper, finding the global optimum requires a large number of objective function evaluations based on the execution of the 1-D FC sandwich model which makes acquiring results in a reasonable time impractical. Therefore, we implemented the below-described sensible approach, which maintains the underlying physics of the 1-D FC sandwich model in our global optimization while enabling much faster execution times for our global optimization. We note that to run our global optimization, we only need to know the geometric current density (i_{1D-MEA}) provided by our 1-D FC model for the range of the FC stack operating parameters in the optimization. Consequently, i_{1D-MEA} is only a function of four independent variables that represent the operating parameters of the FC stack, namely: the stack inlet pressure (P_{Inlet}^{Stack}), the thickness of the anode and cathode electrocatalyst layers (t_{ACL} and t_{CCL}), and the operating voltage of a single cell in the FC stack (V_{Cell}). Therefore, we formed a 4-D matrix of the values of four independent variables in their assigned range (we discussed the assigned ranges to the FC stack operating parameters in the optimization process in detail in the paper): P_{Inlet}^{Stack} values (25 equidistant points on a logarithmic scale varying between the lower bound and higher bound of its specified range), t_{ACL} and t_{CCL} values (25 equidistant points on a logarithmic scale varying between the lower bound and higher bound of their specified range), and V_{Cell} values (20 equidistant points varying between the lower bound and higher bound of its specified range). The only exception to these value assignments was for Fe-N-C containing system where: 1) For the case where we assigned a lower bound of 1 μm and a higher bound of 132.5 μm to t_{CCL}, we assigned 60 equidistant points on a logarithmic scale varying between the lower bound and higher bound of the specified range, and 2) For the case where we assigned a lower bound of 1 μm and a

higher bound of 70 μm to t_{CCL}, we assigned 30 equidistant points on a logarithmic scale varying between the lower bound and higher bound of the specified range. Subsequently, we ran the 1-D FC sandwich model over the 4-D matrix of the values of four independent variables and stored the i_{1D-MEA} results in a matrix. Finally, at the time of global optimization objective function evaluation, we used the matrix of results and the matrix of independent variables' values and performed a cubic spline interpolation to calculate i_{1D-MEA}.

Figures

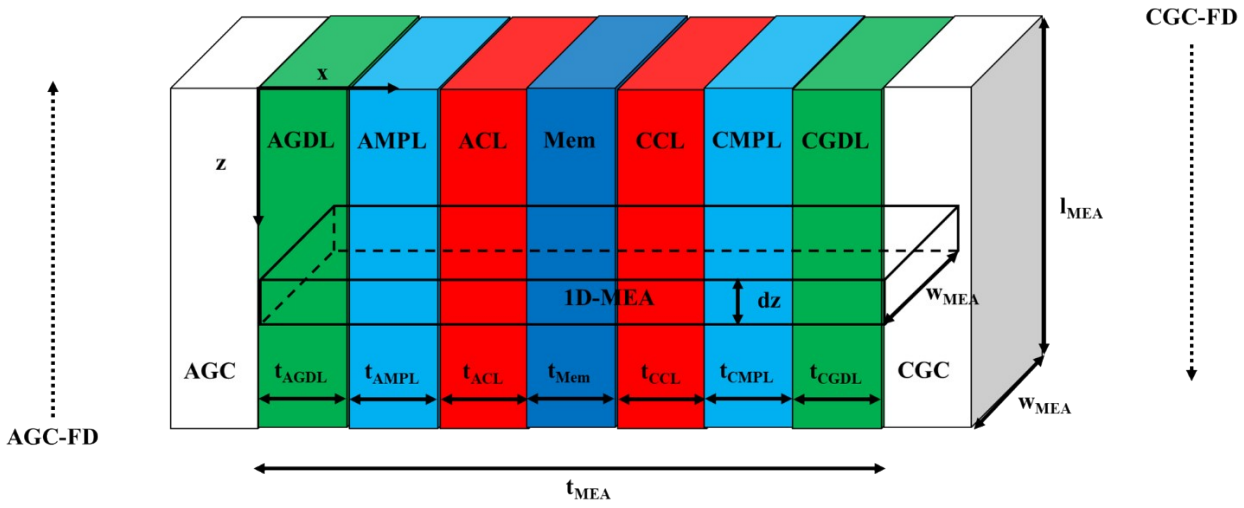

Figure S1: Schematic diagram of our pseudo-2-D FC model, which is a 1-D FC sandwich model coupled with a 1-D down-the-channel model. The 1-D FC sandwich model only considers the direction normal to the MEA along the MEA thickness. The 1-D down-the-channel model consists of mass balance down the channel for the reactants and water coupled with an assumption of linear total pressure drop along the flow channels. The dashed lines show the flow and pressure drop direction in the anode and cathode flow channels. AGC-FD: flow direction in the anode gas channel; AGC: anode gas channel; AMPL: anode microporous layer; ACL: anode electrocatalyst layer; Mem: membrane; CCL: cathode electrocatalyst layer; CMPL: cathode microporous layer; CGDL: cathode gas diffusion layer; CGC: cathode gas channel; CGC-FD: flow direction in the cathode gas channel; t_x: the thickness of layer "x"; l_{MEA}: the length of MEA; w_{MEA}: the width of MEA; dz: the thickness of a discretization unit of a single cell which acts like a FC operating under "differential" conditions which we modeled using a 1-D FC sandwich model;

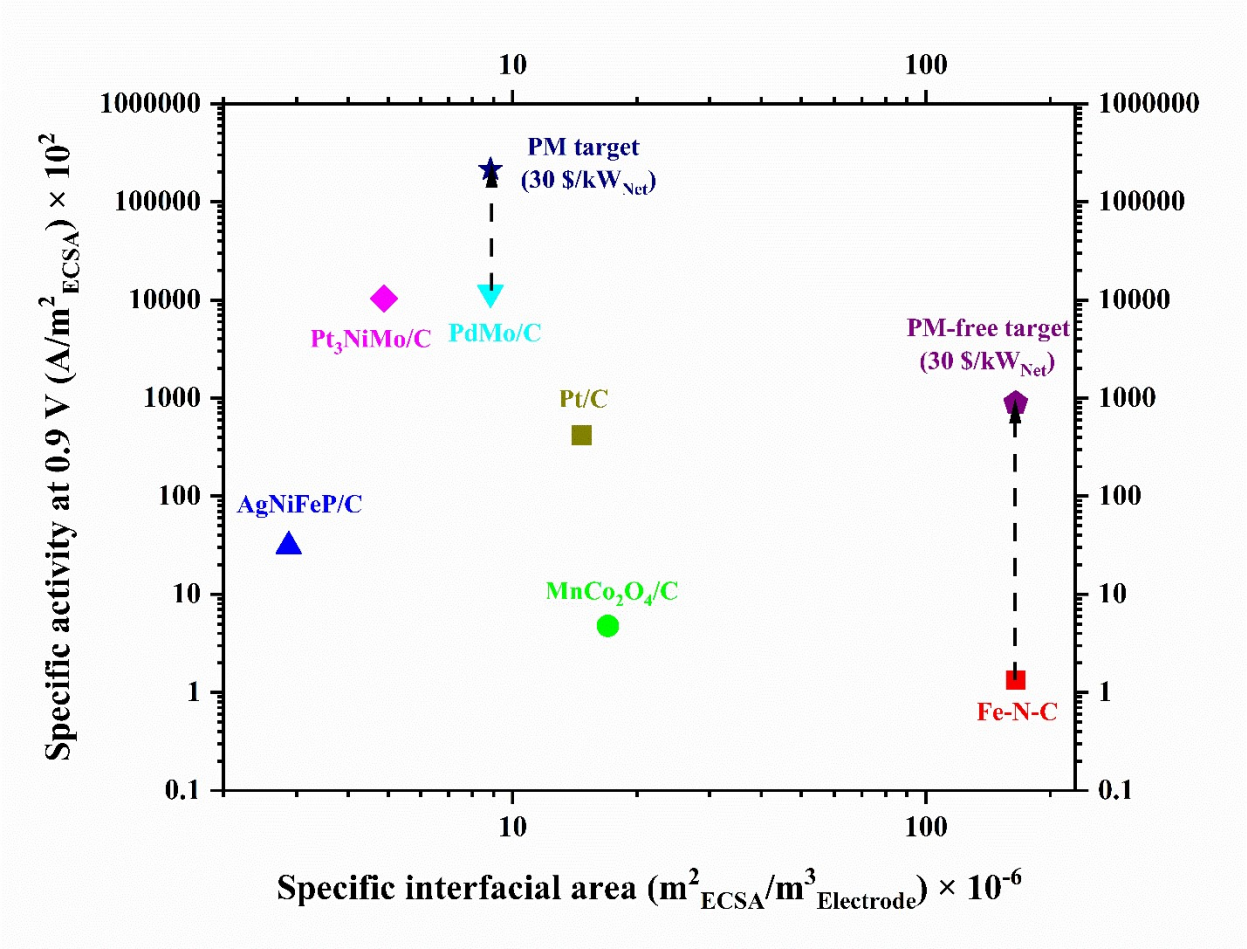

Figure S2-1: The ORR electrocatalyst activity at 0.9 V vs. RHE measured by rotating disk electrode (RDE) in alkaline electrolyte (except for Pt_3NiMo/C, whose activity was measured by RDE in acidic electrolyte) vs. the specific interfacial area of the ORR electrocatalyst. ORR electrocatalyst additional information (the values in parentheses are the electrocatalyst loading in the carbon-supported electrocatalyst, ECSA of the electrocatalyst, and electrocatalyst material cost). AgNiFeP/C (20 wt. %; 43.61 m^2/g; 0.304 \$/g)[48]; Pt_3NiMo/C (21.63 wt. %; 67.5 m^2/g; 43.324 \$/g)[49]; PdMo/C (20 wt. %; 138.7 m^2/g; 57.534 \$/g)[50]; Pt/C (46 wt. %; 62 m^2/g; 1500 \$/tr.oz)[34]; $MnCo_2O_4/C$ (80 wt. %; 32.73 m^2/g; 0.0294 \$/g)[21]; Fe-N-C (NA; 550 m^2/g; 0.0929 \$/g)[16]; All the reported specific activities in Figure S2-1 are at 25 °C and 1 atm partial pressure. The arrows in the figure demonstrate how much improvement in the intrinsic activities of the ORR electrocatalyst is required to achieve the cost target of 30 $/kW$_{Net}$ for (PdMo/C-Ru_7Ni_3/C) and ((Fe-N-C)-Ni/N-doped C) HEMFC systems.

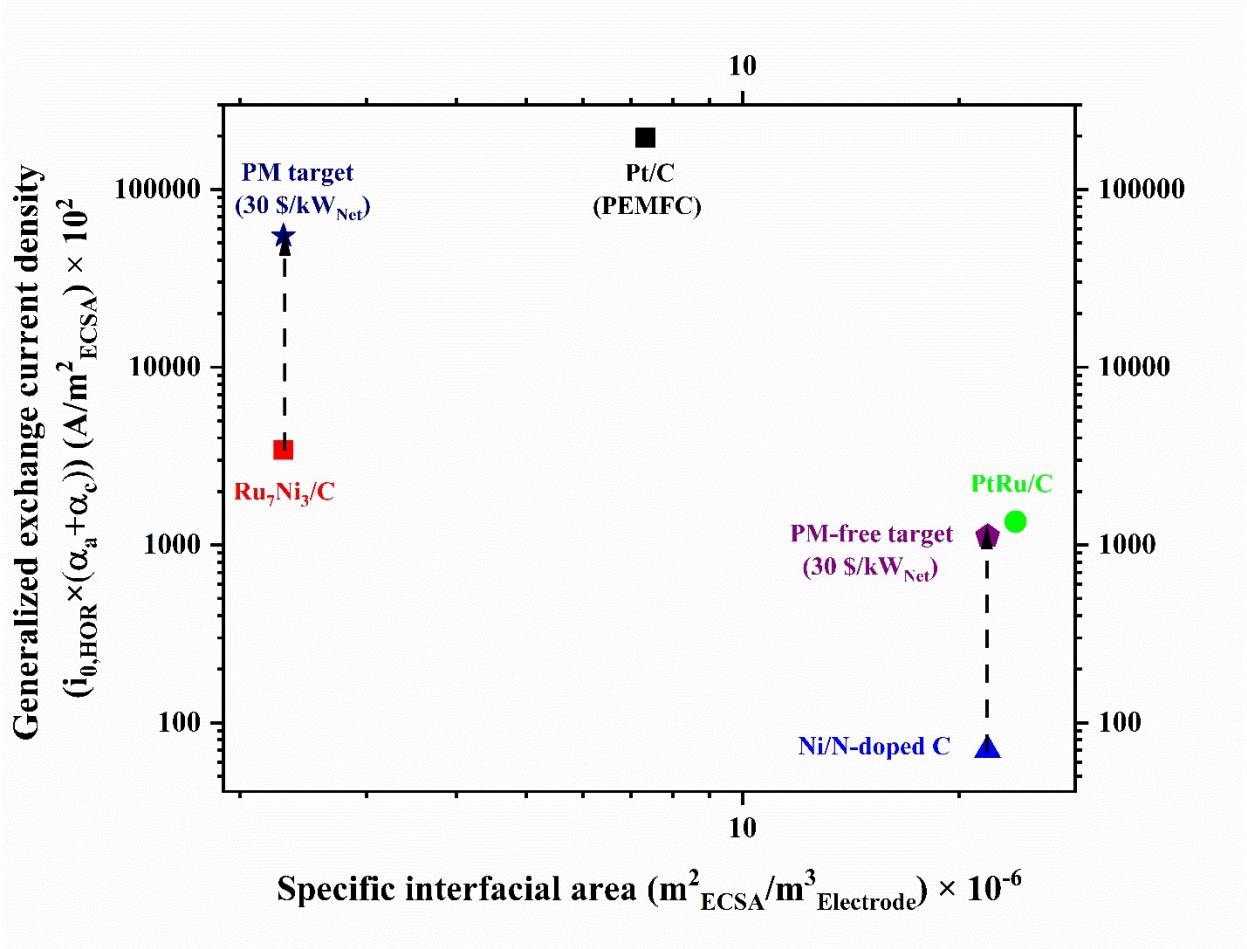

Figure S2-2: The HOR electrocatalyst activity measured by RDE in alkaline electrolyte (except for Pt/C, whose activity was measured by hydrogen pump in acidic electrolyte) vs. the specific interfacial area of the HOR electrocatalyst. HOR electrocatalyst additional information (the values in parentheses are the electrocatalyst loading in the carbon-supported electrocatalyst, ECSA of the electrocatalyst, α_a^{HOR}, α_C^{HOR}, and electrocatalyst material cost). Ru_7Ni_3/C (20 wt. %; 40 m^2/g; 1.5; 0.5; 11.289 $/g)[51]; Pt/C (20 wt %; 100 m^2/g; 0.5; 0.5; 1500 $/tr.oz)[32, 52]; Ni/N-doped C (83 wt. %; 31.35 m^2/g; 0.5; 0.5; 0.0189 $/g)[53]; PtRu/C (60 wt. %; 62.51 m^2/g; 1.5; 0.5; 36.578 $/g)[54]; We assumed that 60 wt. % PtRu/C has the same ECSA as that of 40 wt. % PtRu/C.[54] We normalized the HOR specific activity of 20 wt. % Pt/C measured by the hydrogen pump to 25 °C and 1 atm of partial pressure using activation energy of 16 kJ/mol. Consequently, all the reported specific activities in Figure S2-2 are at 25 °C and 1 atm partial pressure. The arrows in the figure demonstrate how much improvement in the intrinsic activities of the HOR electrocatalysts are required to achieve the cost target of 30 $/$kW_{Net}$ for (PdMo/C-Ru_7Ni_3/C) and ((Fe-N-C)-Ni/N-doped C) HEMFC systems.

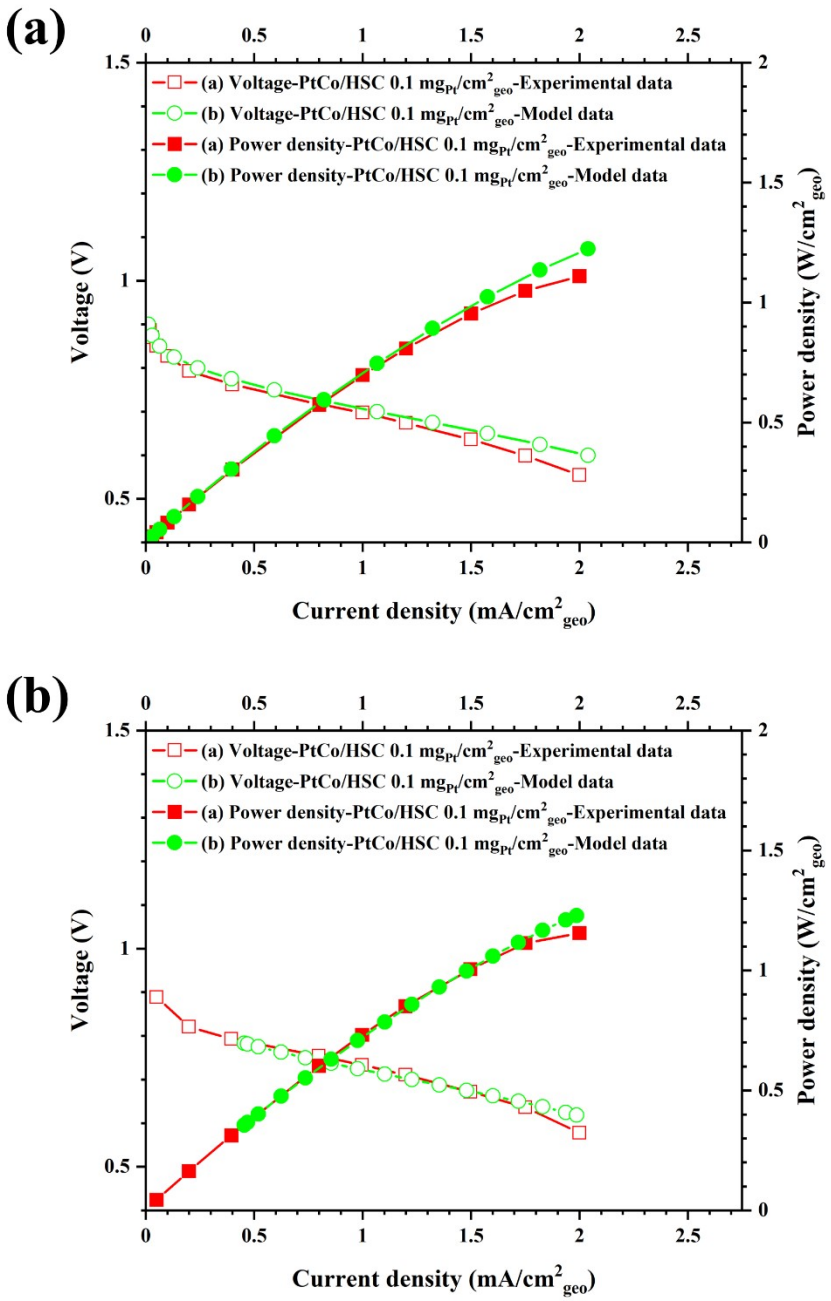

Figure S3: Comparison between model results and experimental data (a) 1-D FC sandwich model results vs. experimental data for a GM's PEMFC operating in differential mode (differential mode corresponds to high gas flows rates giving >10 H_2 and O_2 stoichiometry; 5 cm^2 active area single cell). Operating conditions of the PEMFC in the order of anode/cathode: H_2/air, 80 °C, 100/100% RH, 150/150 kPa$_{Abs}$. (b) Pseudo-2-D FC model results vs. experimental data for a GM's PEMFC operating in counter-flow mode (50 cm^2 active area single cell). Operating conditions of the PEMFC in the order of anode/cathode: H_2/air, 94 °C, 65/65% RH, 250/250 kPa$_{Abs,outlet}$, stoichiometries of 1.5/2.

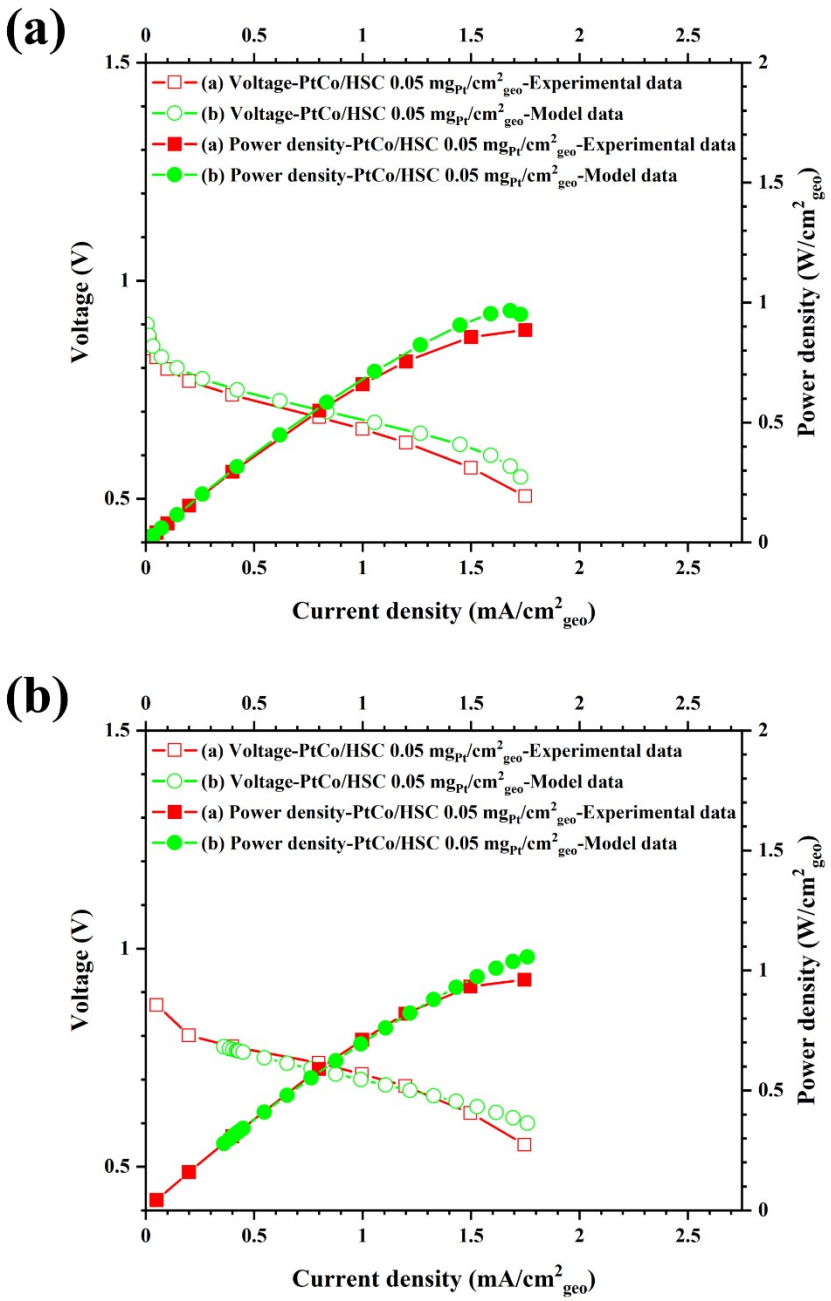

Figure S4: Comparison between model results and experimental data (a) 1-D FC sandwich model results vs. experimental data for a GM's PEMFC operating in differential mode (differential mode corresponds to high gas flows rates giving >10 H_2 and O_2 stoichiometry; 5 cm^2 active area single cell). Operating conditions of the PEMFC in the order of anode/cathode: H_2/air, 80 °C, 100/100% RH, 150/150 kPa_{Abs}. (b) Pseudo-2-D FC model results vs. experimental data for a GM's PEMFC operating in counter-flow mode (50 cm^2 active area single cell). Operating conditions of the PEMFC in the order of anode/cathode: H_2/air, 94 °C, 65/65% RH, 250/250 $kPa_{Abs,outlet}$, stoichiometries of 1.5/2.

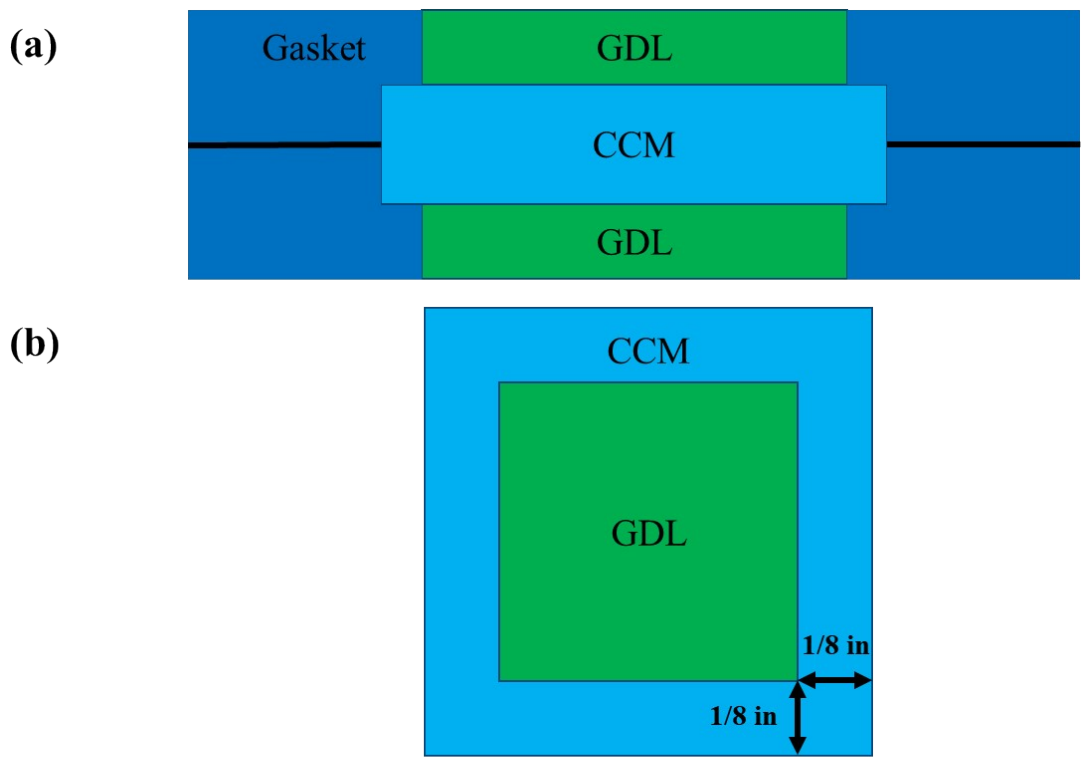

A ~1/8 inch (~0.003175 m) overlap of the gasket over the CCM exists on each side (the figure is not drawn to scale)

Figure S5: (a) MEA cross-section view (b) MEA top view. GDL: gas diffusion layer coated with MPL; CCM: electrocatalyst-coated membrane.

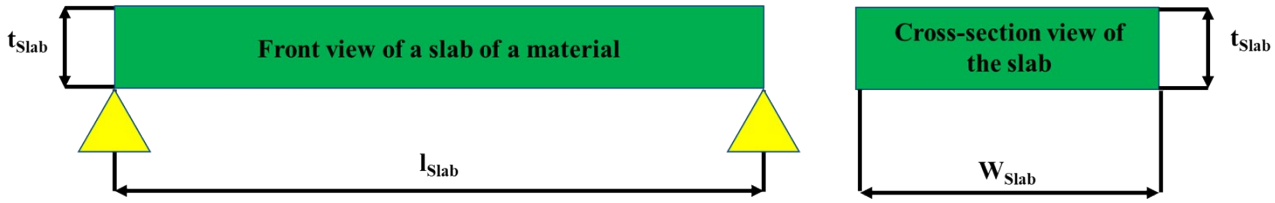

$$l_{Slab} = length\ of\ slab;\ t_{Slab} = thickness\ of\ slab;\ w_{Slab} = width\ of\ slab$$

$$E_{Young} = Young's\ moduls;\ I_{Inertia} = \frac{w_{Slab}{t_{Slab}}^3}{12}(moment\ of\ inertia);$$
$$D_{Flexural} = E_{Young}I_{Inertia}(flexural\ rigidity)$$

Figure S6: Definition of flexural rigidity of a slab of material.

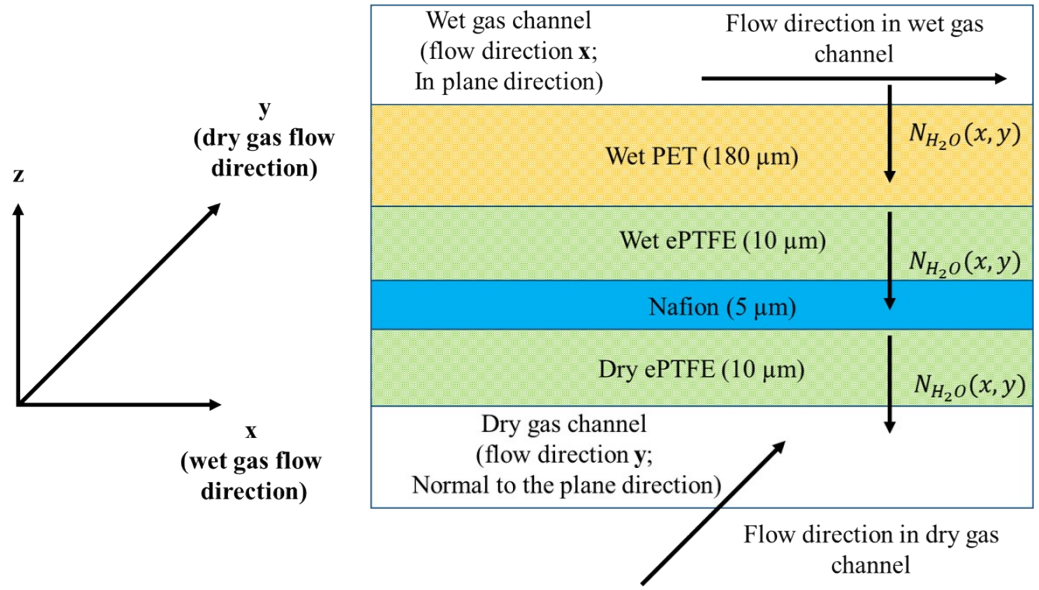

Figure S7: Schematic diagram of the cross-flow membrane humidifier.

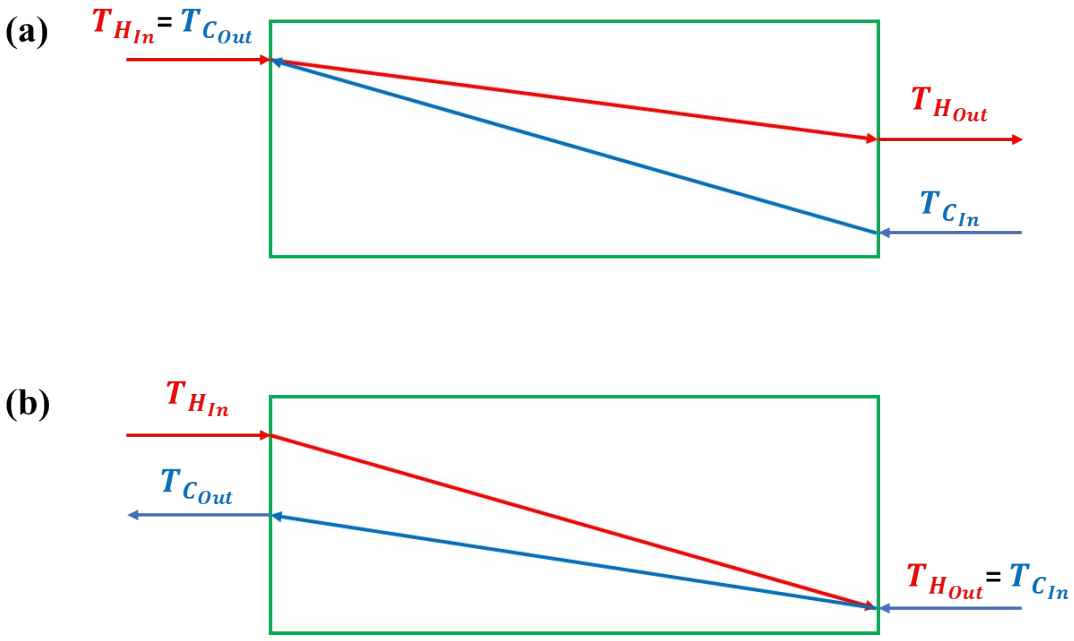

Figure S8: In a counterflow heat exchanger of infinite heat transfer area, one of the two scenarios depicted in Figure S8 is the thermodynamically feasible one. In scenario (a), the cold stream outlet temperature reaches the hot stream inlet temperature while the hot stream outlet temperature remains above the cold stream inlet temperature. In scenario (b), the hot stream outlet temperature reaches the cold stream inlet temperature while the cold stream outlet temperature remains below the hot stream inlet temperature.

(a)

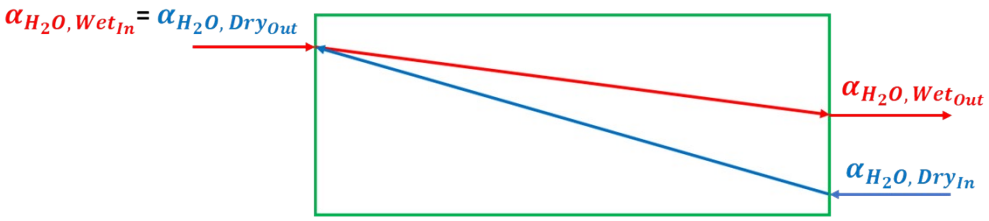

(b)

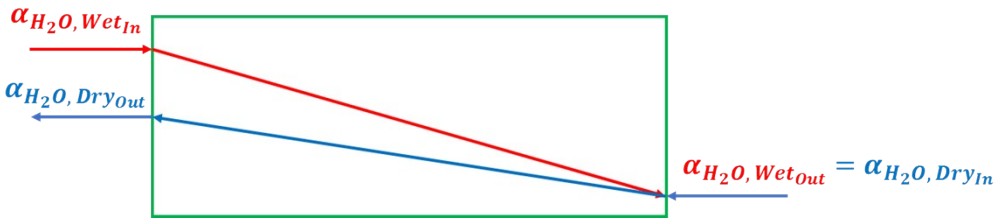

Figure S9: In a counterflow humidifier of infinite mass transfer area, one of the two scenarios depicted in Figure S9 is the thermodynamically feasible one. In scenario (a), the dry air stream outlet H_2O activity reaches the wet air stream inlet H_2O activity while the wet air stream outlet H_2O activity remains above the dry air stream inlet H_2O activity. In scenario (b), the wet air stream outlet H_2O activity reaches the dry air stream inlet H_2O activity while the dry air stream outlet H_2O activity remains below the wet stream inlet H_2O activity.

Tables

Table S1: Dimensions of the modeling domains and the values of transport parameters used for each domain. Eqn "x": equation x in the electronic supporting information.

Parameter	Value
The thickness of GDL, MPL, GDM, and membrane	GM-case: 200; 30; 230; 25 µm Base-case: 105; 45; 150; 10 µm 30 \$/kW$_{Net}$-case: 90; 20; 110; 10 µm
The thickness of electrocatalyst layers	Eqn S1&S2
The porosity of GDL, MPL, and electrocatalyst layers	0.78[55]; 0.585[14]; 0.7
Ionomer volume fraction in the membrane and electrocatalyst layers	GM-case: 1; 0.15 Base-case: 0.95; 0.15 30 \$/kW$_{Net}$-case: 0.95; 0.15
Electrocatalyst volume fraction in electrocatalyst layers	0.15
Thermal conductivity of GDL, MPL, electrocatalyst layers, and membrane	1.45[56]; 0.2; 0.18[57] W/(m.K); Eqn S5&S6
Thermal contact resistance between flow field and GDL	3.4×10^{-4} (K.m^2)/W [57]
Effective diffusivity	Eqn S7 to S11
Total area-specific electronic resistance	20 mΩ.cm^2
The electronic conductivity of the carbon-supported electrocatalysts	120 S/cm
The ionic conductivity, H_2O permeability, the number of H_2O molecules per charged group at equilibrium, and permeation coefficient of ionomers	Eqn S14 to S23

Table S2: Cost breakdown of BPPs of the 2018 LDV PEMFC system as reported in the SA comprehensive report[2]

BPP materials cost ($/Stack)	BPP manufacturing cost ($/Stack)	BPP tooling cost ($/Stack)	BPP coating cost ($/Stack)	BPP total cost ($/Stack)
204	64	52	68	388

Table S3: Details of cost calculation of the coolant reservoir, coolant pump, and coolant piping for the EDCS unit

Component	Cost of the component in the low-temperature coolant loop of the 2018 LDV PEMFC system ($)[2]	Cost of the component in the EDCS unit ($)
Coolant reservoir	6	1.8
Coolant pump	16	4.8
Coolant piping	5	1.5
Total cost		8.1

Table S4: The values of C_V, C_P, and γ for O_2, N_2, and H_2O that we used in our model. R_g: the universal gas constant=8.314 J/(mol.K).

Gas	C_V (J/(mol.K))	C_P (J/(mol.K))	γ
O_2	2.5 R_g	3.5 R_g	$\frac{7}{5}$
N_2	2.5 R_g	3.5 R_g	$\frac{7}{5}$
H_2O	3 R_g	4 R_g	$\frac{4}{3}$

Table S5: The cost breakdown for the air management system for the 2018 LDV PEMFC system reported in the SA comprehensive report ($P_{Comp,Out} = 2.57\ atm$ and $P_{Parasitic} = 8.37\ kW$) for two cases, one with an expander and one without an expander.[2]

The air management system cost (with an expander)		The air management system cost (without an expander)	
Compressor-expander-motor cost ($)	363.25	Compressor-motor cost ($)	243.65
Motor controller cost ($)	437.72	Motor controller cost ($)	437.72
The cost of other components, which remains constant ($)	237.84	The cost of other components, which remains constant ($)	237.84
Total cost ($)	1038.81	Total cost ($)	919.21
Cost savings because of the elimination of expander ($)=119.60 The ratio of compressor-motor cost to compressor-expander-motor cost= 0.67076			

Table S6: The FC stack operating parameters, geometric current density associated with a single cell in the FC stack (i_{Cell}), and the cathode outlet RH ($RH_{Cathode,Out}$) for (PdMo/C-PtRu/C) and (PdMo/C-Ni/N-doped C) HEMFC systems.

FC system	PdMo/C-PtRu/C	PdMo/C-Ni/N-doped C
$L_{Cathode}$ (mg/cm^2)	0.0413	0.0319
t_{CCL} (μm)	5.744	4.433
L_{Anode} (mg/cm^2)	0.0383	3.4680
t_{ACL} (μm)	1.000	49.648
V_{Cell} (V)	0.651	0.650
P_{Inlet}^{Stack} (atm)	1.729	1.763
$RH_{Cathode,Out}$	0.760	0.811
i_{Cell} (A/cm^2)	1.858	1.335

References

1. B. Han, C. E. Carlton, A. Kongkanand, R. S. Kukreja, B. R. Theobald, L. Gan, R. O'Malley, P. Strasser, F. T. Wagner and Y. Shao-Horn, *Energy & Environmental Science*, 2015, **8**, 258-266.
2. B. D. James, J. M. Huya-Kouadio, C. Houchins and D. A. DeSantis, *Mass Production Cost Estimation of Direct H_2 PEM Fuel Cell Systems for Transportation Applications: 2018 Update*, 2018.
3. A. Kongkanand and M. F. Mathias, *The journal of physical chemistry letters*, 2016, **7**, 1127-1137.
4. H. Sadeghifar, N. Djilali and M. Bahrami, *Journal of Power Sources*, 2014, **248**, 632-641.
5. M. Andisheh-Tadbir, E. Kjeang and M. Bahrami, *Journal of Power Sources*, 2015, **296**, 344-351.
6. O. S. Burheim, H. Su, S. Pasupathi, J. G. Pharoah and B. G. Pollet, *International Journal of Hydrogen Energy*, 2013, **38**, 8437-8447.
7. C. Chan, N. Zamel, X. Li and J. Shen, *Electrochimica Acta*, 2012, **65**, 13-21.
8. V. D. Bruggeman, *Annalen der physik*, 1935, **416**, 636-664.
9. M. R. Gerhardt, L. M. Pant and A. Z. Weber, *Journal of The Electrochemical Society*, 2019, **166**, F3180.
10. W. M. Haynes, D. R. Lide and T. J. Bruno, *CRC handbook of chemistry and physics*, CRC press, 2016.
11. N. Nonoyama, S. Okazaki, A. Z. Weber, Y. Ikogi and T. Yoshida, *Journal of The Electrochemical Society*, 2011, **158**, B416.

12. R. B. Bird, W. E. Stewart and E. N. Lightfoot, *Transport phenomena revised 2nd edition*, New York: John Wiley & Sons, Inc, 2006.

13. Z. Liu, B. Brady, R. Carter, B. Litteer, M. Budinski, J. Hyun and D. Muller, *Journal of The Electrochemical Society*, 2008, **155**, B979.

14. J. Lee, R. Banerjee, M. George, D. Muirhead, P. Shrestha, H. Liu, N. Ge, S. Chevalier and A. Bazylak, *Journal of the electrochemical society*, 2017, **164**, F1149.

15. A. Z. Weber and J. Newman, *Journal of the Electrochemical Society*, 2004, **151**, A311.

16. H. Adabi, A. Shakouri, N. Ul Hassan, J. R. Varcoe, B. Zulevi, A. Serov, J. R. Regalbuto and W. E. Mustain, *Nature energy*, 2021, **6**, 834-843.

17. G. Huang, M. Mandal, X. Peng, A. C. Yang-Neyerlin, B. S. Pivovar, W. E. Mustain and P. A. Kohl, *Journal of The Electrochemical Society*, 2019, **166**, F637.

18. N. Ul Hassan, M. Mandal, G. Huang, H. A. Firouzjaie, P. A. Kohl and W. E. Mustain, *Advanced Energy Materials*, 2020, **10**, 2001986.

19. X. Peng, D. Kulkarni, Y. Huang, T. J. Omasta, B. Ng, Y. Zheng, L. Wang, J. M. LaManna, D. S. Hussey and J. R. Varcoe, *Nature communications*, 2020, **11**, 1-10.

20. J. Wang, Y. Zhao, B. P. Setzler, S. Rojas-Carbonell, C. Ben Yehuda, A. Amel, M. Page, L. Wang, K. Hu and L. Shi, *Nature Energy*, 2019, **4**, 392-398.

21. Y. Yang, H. Peng, Y. Xiong, Q. Li, J. Lu, L. Xiao, F. J. DiSalvo, L. Zhuang and H. c. D. Abruña, *ACS Energy Letters*, 2019, **4**, 1251-1257.

22. R. Abbasi, B. P. Setzler, S. Lin, J. Wang, Y. Zhao, H. Xu, B. Pivovar, B. Tian, X. Chen and G. Wu, *Advanced Materials*, 2019, **31**, 1805876.

23. M. Mandal, G. Huang, N. U. Hassan, X. Peng, T. Gu, A. H. Brooks-Starks, B. Bahar, W. E. Mustain and P. A. Kohl, *Journal of The Electrochemical Society*, 2019, **167**, 054501.

24. S. T. Thompson, B. D. James, J. M. Huya-Kouadio, C. Houchins, D. A. DeSantis, R. Ahluwalia, A. R. Wilson, G. Kleen and D. Papageorgopoulos, *Journal of Power Sources*, 2018, **399**, 304-313.

25. S. T. Thompson, D. Peterson, D. Ho and D. Papageorgopoulos, *Journal of The Electrochemical Society*, 2020, **167**, 084514.

26. T. Wang, L. Shi, J. Wang, Y. Zhao, B. P. Setzler, S. Rojas-Carbonell and Y. Yan, *Journal of The Electrochemical Society*, 2019, **166**, F3305.

27. M. Yandrasits, M. Lindell, M. Schaberg and M. Kurkowski, *The Electrochemical Society Interface*, 2017, **26**, 49.

28. T. E. Springer, T. Zawodzinski and S. Gottesfeld, *Journal of the electrochemical society*, 1991, **138**, 2334.

29. E. L. Redmond, K. U. Hansen and D. W. Berg, *ECS Transactions*, 2019, **92**, 445.

30. K. Neyerlin, W. Gu, J. Jorne and H. A. Gasteiger, *Journal of the Electrochemical Society*, 2006, **153**, A1955.

31. A. J. Bard, L. R. Faulkner and H. S. White, *Electrochemical methods: fundamentals and applications*, John Wiley & Sons, 2022.

32. K. Neyerlin, W. Gu, J. Jorne and H. A. Gasteiger, *Journal of The Electrochemical Society*, 2007, **154**, B631.

33. J. Durst, C. Simon, F. Hasché and H. A. Gasteiger, *Journal of The Electrochemical Society*, 2014, **162**, F190.

34. W. Sheng, H. A. Gasteiger and Y. Shao-Horn, *Journal of The Electrochemical Society*, 2010, **157**, B1529.

35. T. A. Zawodzinski, J. Davey, J. Valerio and S. Gottesfeld, *Electrochimica Acta*, 1995, **40**, 297-302.

36. V. Yarlagadda, M. K. Carpenter, T. E. Moylan, R. S. Kukreja, R. Koestner, W. Gu, L. Thompson and A. Kongkanand, *ACS Energy Letters*, 2018, **3**, 618-621.

37. A. Rabbani and M. Rokni, *Applied energy*, 2013, **111**, 1061-1070.

38. R. Ahluwalia and X. Wang, *Journal of Power Sources*, 2007, **171**, 63-71.

39. A. C. Ugural, *Mechanics of materials*, John Wiley & Sons, 2007.

40. L. Shi, Y. Zhao, S. Matz, S. Gottesfeld, B. P. Setzler and Y. Yan, *Nature Energy*, 2022, **7**, 238-247.

41. M. M. Abbott, J. Smith and H. Van Ness, *Chemical engineering thermodynamics*, Boston: McGraw-Hill, 2001.

42. S. Matz, B. P. Setzler, C. M. Weiss, L. Shi, S. Gottesfeld and Y. Yan, *Journal of The Electrochemical Society*, 2021, **168**, 014501.

43. M. MacDonald and R. M. Darling, *AIChE Journal*, 2018, **64**, 3746-3755.

44. D. A. McQuarrie, *Statistical thermodynamics*, HarperCollins Publishers, 1973.

45. F. Kreith and W. Z. Black, *Basic heat transfer*, Harper & Row, 1980.

46. ESDU, *Effectiveness-NTU Relations for the Design and Performance Evaluation of Two-stream Heat Exchangers, Engineering Science Data Unit 86018 with amendment*, ESDU International plc London, 1991.

47. A. Ravindran, G. V. Reklaitis and K. M. Ragsdell, *Engineering optimization: methods and applications*, John Wiley & Sons, 2006.

48. Z. Xu, X. Zhang, X. Wang, J. Fang, Y. Zhang, X. Liu, W. Zhu, Y. Yan and Z. Zhuang, *ACS nano*, 2021, **15**, 7131-7138.

49. X. Huang, Z. Zhao, L. Cao, Y. Chen, E. Zhu, Z. Lin, M. Li, A. Yan, A. Zettl and Y. M. Wang, *Science*, 2015, **348**, 1230-1234.

50. M. Luo, Z. Zhao, Y. Zhang, Y. Sun, Y. Xing, F. Lv, Y. Yang, X. Zhang, S. Hwang and Y. Qin, *Nature*, 2019, **574**, 81-85.

51. Y. Xue, L. Shi, X. Liu, J. Fang, X. Wang, B. P. Setzler, W. Zhu, Y. Yan and Z. Zhuang, *Nature communications*, 2020, **11**, 1-8.

52. 20% Platinum on Carbon XC-72 specifications, https://www.fuelcellstore.com/20-platinum-carbon?search=20%20%%20Platinum, 2023).

53. W. Ni, T. Wang, F. Héroguel, A. Krammer, S. Lee, L. Yao, A. Schüler, J. S. Luterbacher, Y. Yan and X. Hu, *Nature Materials*, 2022, 1-7.

54. J. Nash, J. Zheng, Y. Wang, B. Xu and Y. Yan, *Journal of The Electrochemical Society*, 2018, **165**, J3378.

55. Technical details of Toray Carbon Paper TGP-H-060, https://www.fuelcellearth.com/fuel-cell-products/toray-paper-060/, (accessed 2023).

56. N. Zamel, E. Litovsky, X. Li and J. Kleiman, *international journal of hydrogen energy*, 2011, **36**, 12618-12625.

57. M. Khandelwal and M. Mench, *Journal of Power Sources*, 2006, **161**, 1106-1115.